THE UNIVERSITY OF CHICAGO

HYDRODYNAMIC COUPLING AND OPTICAL PATTERNING OF MANY-PARTICLE COLLOIDAL SYSTEMS

A DISSERTATION SUBMITTED TO
THE FACULTY OF THE DIVISION OF THE PHYSICAL SCIENCES
IN CANDIDACY FOR THE DEGREE OF
DOCTOR OF PHILOSOPHY

DEPARTMENT OF PHYSICS

BY

ERIC ROBERT DUFRESNE

CHICAGO, ILLINOIS

AUGUST 2000

In Memory of J. Michael Nitschke

ACKNOWLEDGEMENTS

If my short career in physics has been at all successful, it is only because I have been lucky enough to be inspired and challenged by a large group of enthusiastic and intelligent scientists and students.

First, I would like to thank my advisor, David Grier. David's enthusiasm and creativity have made working in his laboratory fun and exciting. His patience and generosity have allowed me to explore my own ideas and find my own path. His keen analytical skills, deep physical insight, knack for experiments, and lucid writing have challenged and guided me.

Thanks to the first generation of Grierlings for welcoming me to Chicago and introducing me to the work of our group. I especially would like to thank John Crocker for helping me to download his brain during the two short months that we worked together in David's lab.

I would like to thank the second generation of Grierlings for making our lab a fun, stimulating and supportive place to work during the bulk of my time in Chicago: Chorng Sow, Pamela Korda, Joseph Plewa, Jennifer Curtis, Steven Sundbeck, Yilong Han, Brian Koss, Sven Behrens, Cynthia Hunt, Matthew Vincenz, David Altman, and Benjamin Zwiebel.

Thanks to Todd Squires and Michael Brenner for shedding crucial light on the interpretation of my hydrodynamic data.

I would like to thank Gabe Spalding and all his students at Illinois Wesleyan University for a long and fruitful collaboration. Special thanks to Matthew Dearing, Steven Sheets, and Nathan Mueggenburg.

Outside of my thesis research, many people in the RI and KPTC have contributed to my success and sanity. Thank You! Van Bistrow, Kate Cleary, Jim McConville, Mark Chantell and Stuart Gazes. Thank You! Ward Lopes, Jordan Koss, Journal Clubbers, Bag Lunchers, Stas Potocki, Rosemary Garrison, and Brenda Thomas. Thank You! Alan Thomas and Ken Bradley. Thanks to Kristin Sundbeck for helping me edit this document.

Thanks to John Dawson of the University of New Hampshire, for introducing me to the ideas and culture of physics. Thanks to the teachers at Yale who had the largest influence on my career: William R. Bennett Jr., Ramamurti Shankar, Victor Henrich. Thanks to my undergraduate summer research advisors, J. Michael Nitschke and Robert Horton.

Since long before I could pronounce the word 'physics,' my parents and brothers, Robert, Ann, Mark, Guy and Gary Dufresne, have continually supported and encouraged me in all endeavors. The opportunities they have given me and the lessons in life they have taught me are the foundation of my success and happiness.

My warmest and most abundant thanks are reserved for my strongest ally, my wisest critic, my joy, my peace and my wife, Alexandra.

TABLE OF CONTENTS

LIST OF FIGURES

ABSTRACT

Hydrodynamic interactions couple the Brownian motion of all colloidal particles, yet the fundamental equations of hydrodynamics defy exact solution for all but the simplest colloidal systems. We measure Brownian motion in a variety of few-body colloidal systems using *blinking optical tweezers* and interpret our data in light of the predictions of an approximate theory, *Stokeslet analysis*. Stokeslet analysis describes the weak hydrodynamic coupling of arbitrary numbers of colloidal spheres in free and confined geometries. This theory assumes that the separations between the spheres are much greater than their radii and models their hydrodynamic interactions as those between point-like particles. We find that Stokeslet analysis' predictions are consistent with our measurements, and that it accounts for many-body interactions ignored by the linear superposition of hydrodynamic drag forces.

While Stokeslet analysis can be scaled to analyze larger many-body systems, conventional optical tweezer techniques cannot manipulate more than a few particles. Therefore, we have invented a simple, robust and inexpensive technique to create multiple optical traps from a single laser beam using computer generated holograms. These *holographic optical tweezer arrays* can trap thousands of particles in arbitrary configurations. In addition to enabling direct measurements of many-body interactions, holographic optical tweezer arrays can be applied to study structural phase transitions in colloidal systems, to assemble microscopically textured materials, and to sort and manipulate biological materials.

CHAPTER 1

THE PHYSICS OF COLLOIDAL SUSPENSIONS

1.1 Colloidal Suspensions

A colloid is a suspension of microscopic particles in a liquid. Colloidal particles vary in size from $1\,nm$ to $10\,\mu m$. They can be made of inorganic materials such as gold, clay or silica, or organic materials such as fatty acids, proteins, plastics or even entire cells. Colloidal particles are typically suspended in water. Interactions between particles and with external fields are typically weaker than or comparable to the thermal energy scale. Therefore, in thermal equilibrium, colloidal particles tend to be evenly distributed throughout the suspending fluid.

Colloidal suspensions are vital to human life. Blood, Fig. 1.1, is predominantly made up of $5\,\mu m$ diameter lozenge-shaped cells suspended in an aqueous electrolyte. Milk, Fig. 1.2, is made up of globules of fat and protein suspended in water. Over the centuries, people have learned to exploit the properties of colloidal suspensions for industrial needs. Paint and glue are colloidal suspensions. The industrial production of many familiar substances rely on the enormous surface area to volume ratios of colloidal particles to efficiently catalyze chemical reactions.

In recent years, there has been a resurgent interest in the physical properties of colloidal suspensions, driven by new insights into their microscopic behavior and the desire to create new materials and devices. Colloidal particles interact through a wide range of forces that are delicately balanced in a typical colloidal suspension.

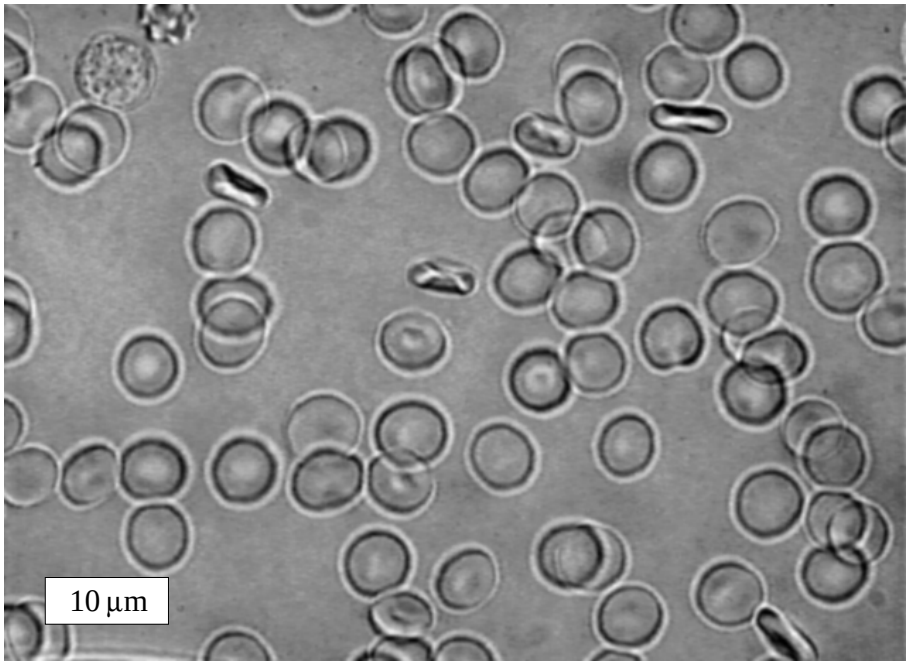

Figure 1.1: *Human blood.*

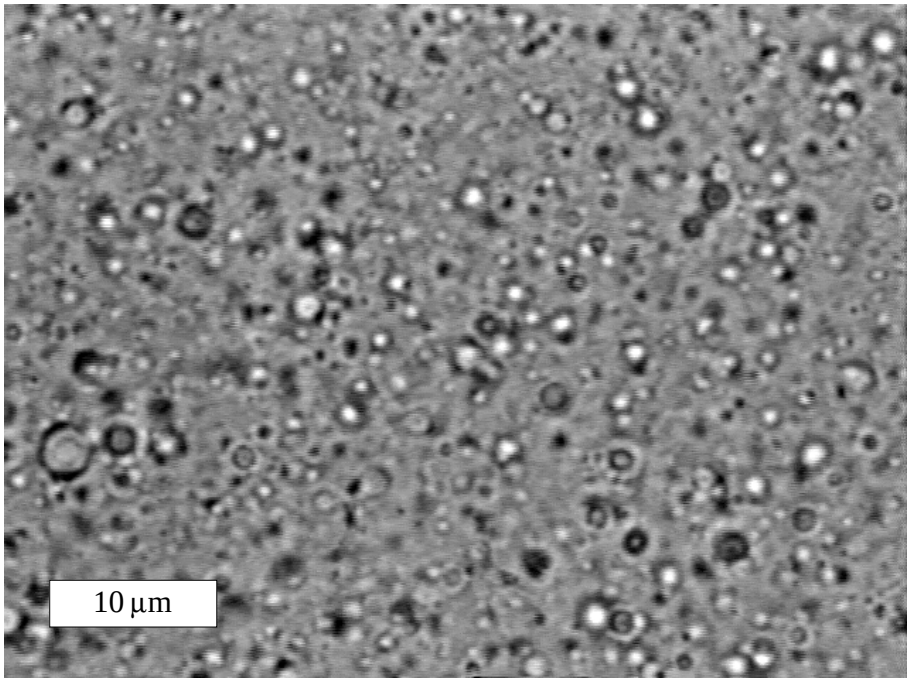

Figure 1.2: *Homogenized cow's milk.*

The relative strength and range of these interactions determine a suspension's stability and structure. For example, if attractive dispersion forces between colloidal particles are not balanced by repulsive electrostatic or steric interactions, the particles will coagulate and fall out of the suspension. The early history of modern colloid science focused on understanding and controlling this balance of forces to stabilize colloidal suspensions.

More recently, the focus of colloid science has shifted from stability to structure. Depending on the exact nature of the balance of forces in a colloidal suspension, colloidal particles can be arranged in a variety of structural phases including both common gaseous, liquid, and crystalline phases as well as more exotic phases with no atomic counterparts. For example, if repulsive forces exceed the thermal energy scale in dense suspensions of identical particles, the particles can form ordered structures called colloidal crystals, Fig. 1.3. Soon after light microscopy first revealed their organized structure [1], colloidal crystals came to be studied as a model system for understanding the equilibrium structure and non-equilibrium melting and freezing of conventional atomic crystals.

The study of colloidal crystals has received a further boost in recent years because of their fabulous optical properties [2–5]. Since the lattice constants of colloidal crystals are comparable to the wavelength of light, colloidal crystals scatter visible light of different wavelengths in different directions, just as atomic crystals Bragg scatter x-rays of different energies into different angles. Consequently, colloidal crystals, made up of millions of transparent spheres, can shimmer brightly with a wide spectrum of colors. This is the same effect that gives an opal its characteristic colored glow, for an opal is a dessicated crystal of colloidal silica spheres [6]. Yet colloidal crystals can interact with light in more subtle and powerful ways.

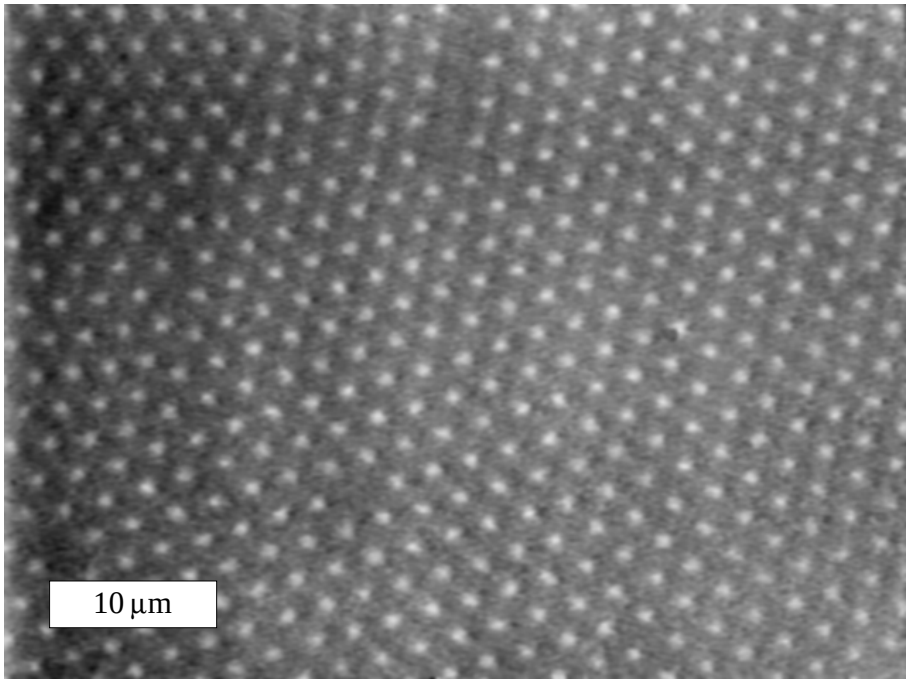

Figure 1.3: *Colloidal crystal.* $352\,nm$ diameter charged polystyrene spheres.

Colloidal crystals made up of special types of particles are predicted to have a *full photonic band gap* [7–9]. In analogy to the electronic band gaps in semiconductors, a photon whose energy lies within a photonic band gap cannot propagate through the crystal. Photons within the band gap are strongly affected by defects in perfect photonic crystals, which can form resonant cavities, waveguides and switches. Someday, these pieces may be wired together to create logical elements, with the ultimate goal of creating fast and efficient photonic computers.

Recently, colloidal systems have been studied as models for explaining the physical processes underlying biological systems. Large bio-molecules, and complex cellular components experience the same forces as simple colloidal particles [10–13]. As we advance our understanding of the fundamental interactions and dynamics of colloidal systems, we will gain new insight into the mechanics of the fundamental building blocks of biological systems.

The forces that drive the motions of colloidal particles lie at the heart of all colloidal phenomena. These forces arise from interactions with the suspending fluid and interactions between the particles. The interactions between particles are mediated by the fluid and can be surprisingly complex in even the simplest of systems. This thesis describes measurements of hydrodynamic interactions in colloidal systems whose well defined and tightly controlled geometries enable us to directly test a versatile new theory of the hydrodynamic coupling between colloidal particles.

1.2 Brownian Motion

Colloidal particles never rest. They jiggle and jerk along the fractal trajectories first observed by Brown in 1827 [14]. At the turn of the 20th century, Einstein [15], Langevin [16], and Perrin [17, 18] placed the observed motion of Brownian particles in the context of macroscopic diffusion, equilibrium thermodynamics, and the molecular nature of matter. Simply stated, they found that the solvent shares its thermal energy with colloidal particles through constant intermolecular collisions. The incessant Brownian motion of colloidal particles drives the suspension towards a macroscopically uniform dispersed state, with any inhomogeneities eventually diffusing away. Diffusion therefore describes the evolution of a colloidal suspension's macroscopic structure.

1.2.1 Fick's Laws

We now know that diffusion is driven by the Brownian motion of individual colloidal particles. However, Fick developed the first quantitative theory of diffusion in 1855, without any knowledge of the underlying Brownian motion [19]. Fick's result

follows from two simple principles. First, colloidal particles tend to diffuse down concentration gradients. According to Fick's first law of diffusion, the diffusive flux of colloidal particles is proportional to the gradient of their concentration

$$\vec{J}^D(\vec{r}) = -D\,\vec{\nabla} n(\vec{r}), \tag{1.1}$$

where D is the diffusion coefficient of the colloidal particles and $n(\vec{r})$ is the concentration of colloid at $\vec{r}$. Second, the total number of colloidal particles is conserved. Therefore, the concentration of spheres must satisfy

$$\frac{\partial n}{\partial t} = -\vec{\nabla} \cdot \vec{J}(\vec{r}). \tag{1.2}$$

If the particles' dynamics are solely diffusive then $\vec{J} = \vec{J}^D$ and we can combine these two equations to arrive at Fick's second law,

$$\frac{\partial n}{\partial t} = D\,\nabla^2 n. \tag{1.3}$$

Therefore, if a collection of N colloidal spheres starts off at $\vec{r}_o$ at $t = 0$, then the concentration evolves according to

$$n(\vec{r}, t) = \frac{N}{(4\pi D t)^{d/2}} \exp\Big[\frac{-|\vec{r} - \vec{r}_o|^2}{4Dt}\Big], \tag{1.4}$$

in d dimensions. The cloud of particles expands such that its mean-squared width increases linearly with time,

$$\langle r(t)^2 \rangle = 2dD\,t. \tag{1.5}$$

1.2.2 Stokes-Einstein Relation

In 1905, Einstein related the diffusion coefficient of a colloidal suspension to its temperature, the size of its constituent particles, and the viscosity of its solvent. He considered a colloidal suspension in an applied potential, $\Phi(\vec{r})$. In equilibrium, the net particle flux must vanish, $\vec{J}(\vec{r}) = 0$. Therefore, the diffusive flux $\vec{J}^D(\vec{r})$ must be balanced by an interaction-driven flux, $\vec{J}^I(\vec{r})$, resulting from gradients in $\Phi(\vec{r})$.

To calculate the flux due to interactions with the external field, Einstein assumed that the particles' motions are overdamped. Overdamped particles move only when driven. Specifically, the velocity of an overdamped particle, $\vec{v}(\vec{r})$, is proportional to the applied force, $\vec{f}(\vec{r})$,

$$\vec{v}(\vec{r}) = b\ \vec{f}(\vec{r}), \tag{1.6}$$

where b is the particle's hydrodynamic mobility. The force on a particle at $\vec{r}$ is given by the gradient of the externally applied potential,

$$\vec{f}(\vec{r}) = -\vec{\nabla}\Phi(\vec{r}). \tag{1.7}$$

In equilibrium, the potential is related to the concentration of particles through the Boltzmann distribution,

$$n(\vec{r}) = n_o \exp\left[-\frac{\Phi(\vec{r})}{k_B T}\right]. \tag{1.8}$$

Thus, $\vec{f}(\vec{r}) = k_B T\ \vec{\nabla}\log[n(\vec{r})]$. Since, $\vec{J}(\vec{r}) = n(\vec{r})\ v(\vec{r})$, we can combine the above

to give

$$\vec{J}^I(\vec{r}) = k_B T\, b\, \vec{\nabla} n(\vec{r}). \tag{1.9}$$

Applying the condition for equilibrium, $\vec{J}^D + \vec{J}^I = 0$, to Eqs. 1.1 and 1.9, we find that

$$D = k_B T\, b. \tag{1.10}$$

Therefore, if the colloidal particle is a sphere of radius, a, and is immersed in a fluid of viscosity, η, then we can apply Stokes' law for the hydrodynamic mobility, $b = (6\pi\eta a)^{-1}$, to obtain the Stokes-Einstein relation,

$$D = \frac{k_B T}{6\pi\eta a}. \tag{1.11}$$

Equations 1.5 and 1.11 provide a means to determine Boltzmann's constant, and thus Avogadro's number, by measuring the Brownian motion of colloidal particles of known radius in a fluid of known viscosity and temperature. This experiment won Perrin the Nobel prize in 1926.

1.2.3 Langevin Theory

Langevin developed an alternative formalism for describing the Brownian motion of a single particle based on Newton's second law and a simple model of a Brownian

particle's collisions with solvent molecules. The Langevin equation,

$$m\dot{v}(t) = -\gamma v(t) + \nu(t), \tag{1.12}$$

says that the total force on a Brownian particle is the sum its hydrodynamic drag and a random force due to collisions with solvent molecules. The hydrodynamic drag coefficient, γ, is the inverse of the mobility. For a sphere, $\gamma = 1/b = 6\pi\eta a$. The random force, $\nu(t)$, vanishes on average, $\langle \nu(t) \rangle = 0$, and is assumed to be uncorrelated over all accessible length and time scales,

$$\langle \nu(t)\nu(0) \rangle = \Gamma\delta(t), \tag{1.13}$$

where Γ characterizes the strength of the random force. The Langevin equation, Eq. 1.12, can be solved for the particle's velocity,

$$v(t) = v(t_o)e^{-(t-t_o)/\tau} + \frac{1}{m}\int_{t_o}^{t} e^{-(t-t')/\tau}\nu(t')dt', \tag{1.14}$$

where the viscous relaxation time, $\tau = m/\gamma$, ranges from 10^{-13} to 10^{-6} sec for typical aqueous colloids. This formal solution for $v(t)$ can be combined with the statistical properties of the random thermal force, $\nu(t)$, to calculate the auto-correlation of the particle's velocity,

$$\langle v(t)v(0) \rangle = \frac{\Gamma}{2m\gamma}e^{-\frac{t}{\tau}}, \tag{1.15}$$

where $t > 0$. Therefore, sampling the particle's motions at intervals greater than τ yields completely uncorrelated velocities, and the particles effectively have

no inertial mass. At short times, the equipartition theorem must hold, so that $\frac{1}{2}m\langle v(0)v(0)\rangle = \frac{1}{2}k_BT$. Combining this with Eq. 1.15 yields Einstein's relation between the microscopic random driving force and the macroscopic drag,

$$\Gamma = 2\,\gamma\,k_BT. \tag{1.16}$$

This result was the original expression of the fluctuation-dissipation theorem. Finally, the expression for the particle's velocity, $v(t)$, can be integrated and averaged to give the Brownian particle's mean-squared displacement,

$$\langle [x(t) - x(t_o)]^2 \rangle = 2D(t - t_o), \tag{1.17}$$

where $D = k_BT/6\pi\eta a$. Fick's law yielded the same result, Eq. 1.5, but now it is apparent that Brownian motion is driven by microscopic collisions with individual solvent molecules and moderated by hydrodynamic coupling to the solvent's macroscopic flow-field.

The Langevin equation also can describe the motion of a Brownian particle in a harmonic well [20],

$$m\ddot{x}(t) = -\gamma\dot{x}(t) - kx + \nu(t), \tag{1.18}$$

where k is the well's curvature. In the overdamped limit, $m\ddot{x} \to 0$, so

$$\gamma\dot{x} = -kx + \nu(t), \tag{1.19}$$

which is formally equivalent to Eq. 1.12. Thus, the particle's trajectory is given by

$$x(t) = x(t_o)e^{-\frac{k}{\gamma}(t-t_o)} + \frac{1}{\gamma}\int_{t_o}^{t} e^{-\frac{k}{\gamma}(t-t')}\nu(\tau)dt', \tag{1.20}$$

and the autocorrelation of the particle's position evolves according to

$$\langle x(t)x(0)\rangle = \frac{k_B T}{k}e^{-\frac{k}{\gamma}t}, \tag{1.21}$$

where $t > 0$. A trajectory's correlations decay exponentially with a timescale, $\tau' = \gamma/k$, set by viscous drag and the shape of the confining potential. This result will be useful in the Appendix, where we study the motions of colloidal particles trapped in optical tweezers.

1.3 Colloidal Interactions

While the interactions with the solvent drive the Brownian motion of colloidal particles, interactions between colloidal particles affect the stability and phase behavior of colloidal suspensions. Dispersion, electrostatic, entropic and hydrodynamic forces play important roles in the properties of colloidal suspensions.

Derjaguin, Landau, Verwey and Overbeek developed the standard theory of electrostatic and dispersion interactions in colloidal suspensions [21] to explain the stability of charge-stabilized colloidal suspensions. Colloidal particles suspended in a fluid of lower dielectric constant are attracted to each other by strong van der Waals or dispersion forces, created by thermally driven fluctuations of their dipole moments. For two spheres of radius a, whose surfaces are separated by a distance

h, these fluctuation-induced attractions have the form

$$\frac{V(r)}{k_B T} = -\frac{A}{6}\left(\frac{2}{x^2-4} + \frac{2}{x^2} + \ln\left[\frac{x^2-4}{x^2}\right]\right), \tag{1.22}$$

where $x \equiv h/a$, and A is the Hamacker constant which depends on the material properties of the spheres and the intervening solvent [10]. For latex particles suspended in water, the Hamacker constant is comparable to $k_B T$. Dispersion attractions are negligible when the spheres are separated by more than about $100\,nm$, but they become enormous when the spheres are in contact. Two spheres that approach each other within the range of dispersion attractions stick to one another irreversibly. In order to create a stable colloidal suspension, repulsive interactions must overcome these strong attractive interactions between colloidal particles. Colloidal suspensions are typically stabilized by introducing steric or electrostatic interactions between the particles.

The electrostatic repulsion between like-charged colloidal particles is screened by the solvent's ions, and is naturally described in terms of the Poisson-Boltzmann theory of the distribution of mobile ions [21]. A linearized mean field description yields

$$\frac{U(r)}{k_B T} = Z^{*2}\left(\frac{e^{\kappa a}}{1+\kappa a}\right)^2 \frac{\lambda_B}{r}\, e^{-\kappa r}, \tag{1.23}$$

for the screened Coulomb repulsion between a pair of identical spheres, where Z^* is the spheres' effective charge, κ^{-1} is the inverse screening length, a is the spheres' radius, λ_B is the Bjerrum length, and r is the center-to-center distance separating the spheres. The Bjerrum length is the separation where two electrons repel one

another with $1\,k_BT$,

$$\lambda_B = \frac{e^2}{4\pi\epsilon_o\epsilon\, k_BT}. \tag{1.24}$$

The screening length, κ^{-1}, depends on the concentration, n_i, and valence, z_i, of each ionic species,

$$\kappa^2 = \frac{e^2}{\epsilon_o\epsilon k_BT}\sum_i n_i\, z_i^2. \tag{1.25}$$

This picture is only valid when the coupling between the spheres and the mobile ions is much weaker than k_BT. Outside of this regime, non-linear coupling and ion-ion correlations can overscreen [22] or possibly even reverse the sign of electrostatic interactions [13, 23–25].

Entropically-driven forces can also play important roles in polydisperse suspensions and mixtures of colloid and polymers. Entropic or depletion forces have been the focus of much recent work [26–31].

Finally, hydrodynamic interactions can couple the motions of all colloidal particles. As particles move through a fluid, they create long-ranged hydrodynamic flows, which apply forces to other particles in the fluid. The nature of hydrodynamic coupling in colloidal suspensions is considered in detail in Chapter 3. In addition to presenting the form of interactions in simple two-body systems, we consider many-body hydrodynamic interactions in dilute suspensions of confined colloid. We measure Brownian motion in a variety of few-body colloidal systems using *blinking optical tweezers*, and interpret our data in light of the predictions of Stokeslet analysis. While Stokeslet analysis can be extended to describe weak

hydrodynamic coupling between arbitrary numbers of particles, conventional optical tweezer techniques cannot manipulate more than a few particles. In Chapter 4, we present a simple, robust and inexpensive technique to create multiple optical traps from a single laser beam using computer generated holograms. These *holographic optical tweezer arrays* can trap thousands of particles in arbitrary configurations. In addition to enabling direct measurements of many-body interactions, holographic optical tweezer arrays can be applied to study structural phase transitions in colloidal systems, to assemble microscopically textured materials and to sort and manipulate biological materials.

CHAPTER 2

MICROSCOPIC OBSERVATION AND MANIPULATION OF COLLOIDAL SUSPENSIONS

This chapter describes the experimental techniques employed in this thesis for studying the dynamics of colloidal suspensions. *Digital video microscopy* records the trajectories of individual colloidal particles. These trajectories can be analyzed to understand both the dynamics of individual particles and the collective behavior of many particles. *Optical tweezers* can manipulate individual colloidal particles, and have enabled precise measurements of the interactions and dynamics of small numbers of particles. Techniques developed in the course of this research will soon enhance the utility of optical tweezers to address collective phenomena in colloidal suspensions and enable the micro-assembly of new materials [32].

2.1 Digital Video Microscopy

Digital video microscopy (DVM) combines conventional optical microscopy, digital imaging and computerized image processing to observe, record and calculate the trajectories of colloidal particles. First, the particles are imaged with bright field microscopy, Fig. 2.1. An inverted optical microscope (Olympus IMT-2) equipped with an oil-immersion objective lens (Olympus S-Plan Apochromat, $NA = 1.4$, $f = 1.62\,mm$, $100\times$) projects images of the suspension onto a CCD camera (NEC

TI-324A), which encodes the images in a standard video signal. The images are displayed on a television monitor and recorded by a VCR (JVC BR-S822DXU).

Once images have been recorded on video tape, they are digitized, stored, and processed by a personal computer. A frame grabber (MuTech MV1000/1350) digitizes the video images and the computer records them to disk in real-time. One standard video image, or frame, is generated every $1/30\,sec$. Each frame is the superposition of two interlaced partial images, or fields, which are exposed once every $1/60\,sec$, Fig. 2.2. Image processing algorithms [33], implemented in IDL (Interactive Data Language, Research Systems Inc.), filter the images, identify particles, and track their movements. Particle locations can be sampled 60 times per second with a resolution, δx, of about $20nm$. The resulting particle trajectories can be analyzed to extract information regarding the colloidal suspension's physical properties.

Digital video microscopy is a powerful technique, yet subject to several limitations. For example, wave optics and Brownian motion place lower limits on the size of colloidal particles that can be tracked with DVM. Only particles whose size is comparable to or larger than the wavelength of light can form resolvable images, that is, $a \gtrsim \lambda/2$. Brownian motion also blurs the image of a colloidal particle when it diffuses a distance greater than the spatial resolution of our imaging system, δx, during the exposure time, τ_{exp}, of the CCD. Therefore we require $\langle \Delta x^2(\tau_{exp}) \rangle < \delta x^2$, or

$$a > \frac{k_B T\, \tau_{exp}}{3\pi\eta\, \delta x^2}. \tag{2.1}$$

On the other hand, if the particles are too big, the Brownian motions, which disperse

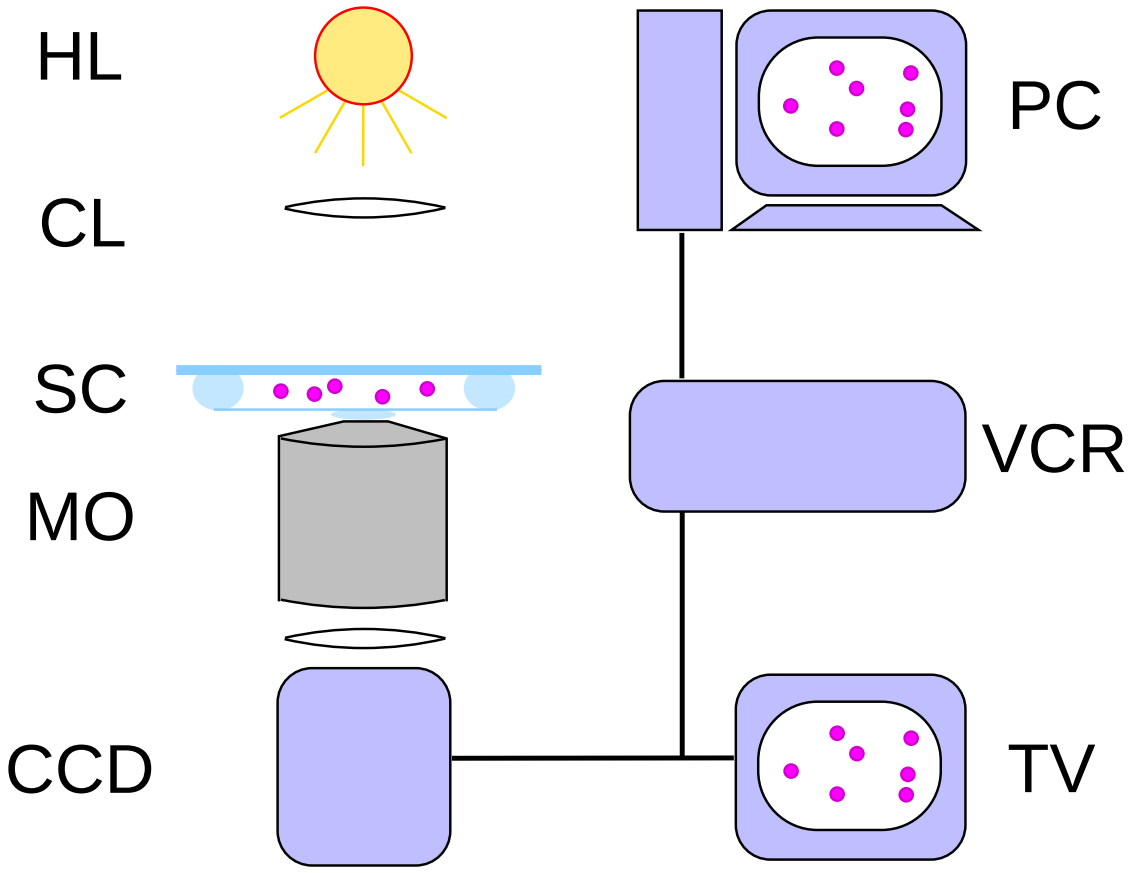

Figure 2.1: *Digital video microscopy.* Light from a halogen lamp, **HL**, is focused by a condenser lens, **CL**, onto the colloidal sample cell, **SC**. A microscope objective, **MO**, and additional transfer optics project an image of the colloid onto the surface of a CCD camera, **CCD**. The CCD's video signal is displayed on a television monitor, **TV**, and recorded by a VCR, **VCR**. A personal computer, **PC**, stores and processes the images.

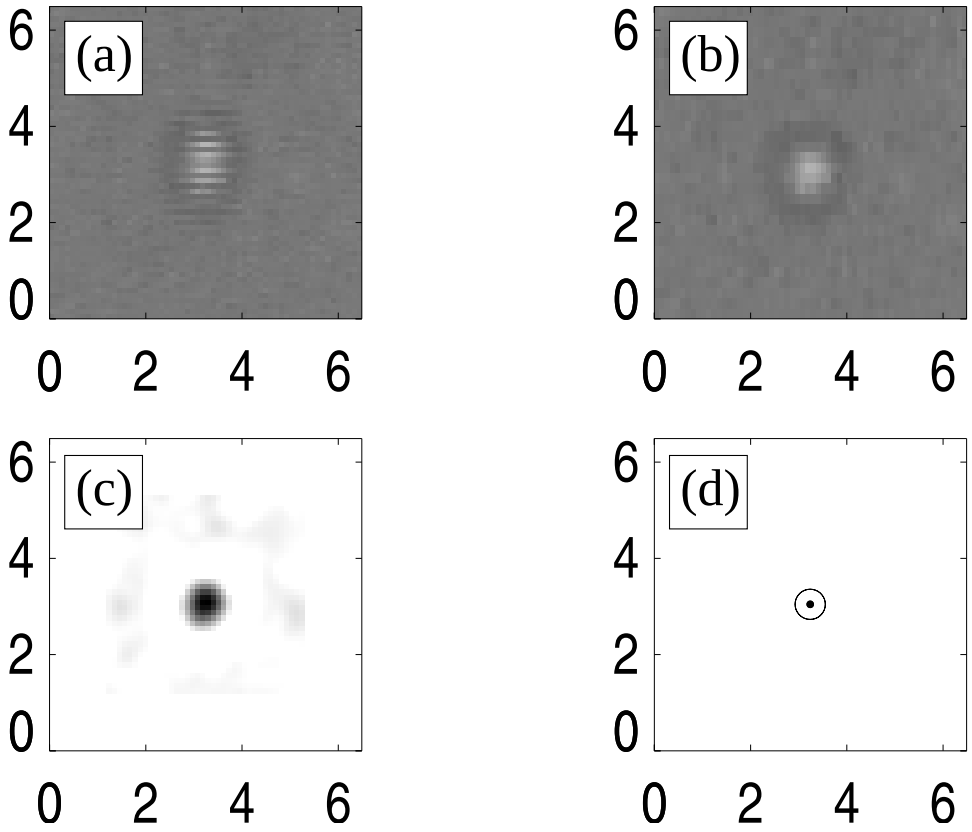

Figure 2.2: *Image processing. (a)*: The original interlaced image. *(b)*: A single field, rescaled to the original image size. *(c)*: The band-pass filtered image. *(d)*: The particle location, the brightness centroid of the band-pass filtered image. Axes are calibrated in *microns*.

them throughout the suspension, will be overwhelmed by inertial effects. If the particles are dispersed in water at room temperature, these considerations lead to an optimal range of particle diameters from about 0.5 to 3 μm. Further limitations of DVM and some alternative particle tracking techniques are presented in the Appendix.

2.2 The Optical Tweezer

In 1986, Arthur Ashkin and coworkers showed that a tightly focused laser beam can trap microscopic dielectric particles at the bottom of a three-dimensional potential well, several k_BT deep and less than a cubic-wavelength in volume [34]. Their invention, the *optical tweezer*, is revolutionizing the way scientists study the microscopic structure and dynamics of aqueous systems. Scientists have used the optical tweezer to measure tiny forces in physical [23, 31, 35–39] and biological [40–45] systems, and to sort and assemble microscopic particles [32, 46–48].

2.2.1 Rayleigh Theory of Optical Tweezers

Even though existing theories cannot describe the tweezer effect over a wide range of particle sizes and compositions, they can provide practical insight into the physics of optical tweezers. Simple descriptions of the optical trapping effect can be formulated for dielectric spheres in the ray optics [49] and Rayleigh limits [50].

We present the results of Harada's Rayleigh theory of optical tweezers [50]. Harada derives the optical forces on a dielectric sphere whose radius, a, is much smaller than the wavelength of trapping light, $a \ll \lambda$. The sphere is modeled as a

point dipole of strength, $\vec{p} = \alpha\vec{E}$, where $\vec{E}$ is the electric field of the laser light,

$$\alpha = 4\pi\epsilon_0 \left(\frac{\epsilon - \epsilon_0}{\epsilon + 2\epsilon_0}\right) a^3 \tag{2.2}$$

is the sphere's polarizability, ϵ is the sphere's dielectric constant at optical frequencies, and ϵ_0 is the dielectric constant of the medium surrounding the sphere. This is the quasi-static limit, where we assume that the electronic configuration of the particle can follow the oscillations of the electric field in phase. This assumption is valid whenever the frequency of the laser is tuned below the sphere's electronic resonances. In this limit, laser light exerts two forces on dielectric particles: the scattering force, $\vec{F}_s$, and the gradient force, $\vec{F}_\nabla$.

The scattering force drives the particle along the direction of propagation of the illuminating radiation. A sub-wavelength dielectric sphere scatters light with a dipole radiation pattern. While the illuminating radiation has a well-defined momentum density, described by the Poynting vector, $\vec{S}$, the scattered light has no net momentum. Therefore, conservation of momentum requires that the sphere feels a force, $\vec{F}_s$, along the original direction of propagation of the laser light:

$$\vec{F}_s = \frac{8}{3}\pi(ka)^4 a^2 \frac{\sqrt{\epsilon_0}}{c}\left(\frac{\epsilon - \epsilon_0}{\epsilon + 2\epsilon_0}\right)^2 \vec{S}. \tag{2.3}$$

The gradient force drives the particle along the gradient of the laser's intensity. An electric dipole, $\vec{p}$, experiences a force, $\vec{F}_\nabla = (\vec{p}\cdot\vec{\nabla})\vec{E}$, in a spatially varying electric field, $\vec{E}$. Since the sphere's dipole moment is proportional to the electric field, $\vec{F}_\nabla = \alpha(\vec{E}\cdot\vec{\nabla})\vec{E}$. Assuming $\vec{\nabla}\times\vec{E} = 0$ and applying some vector identities, we find that $\vec{F}_\nabla \propto \vec{\nabla}(\vec{E}\cdot\vec{E})$. For an electromagnetic plane wave, $\vec{F}_\nabla \propto \vec{\nabla}|\vec{S}|$.

Taking geometrical factors into account, Harada shows that

$$\vec{F}_{\nabla} = 2\pi a^3 \frac{\sqrt{\epsilon_0}}{c}\left(\frac{\epsilon - \epsilon_0}{\epsilon + 2\epsilon_0}\right)\vec{\nabla}\,|\vec{S}|. \tag{2.4}$$

The gradient force is proportional to the dielectric constant mismatch between the particle and the medium in which it is suspended. If the particle's dielectric constant is greater than the suspending medium's, it will be driven toward bright regions.

If the laser is focused to a tight spot, as in Fig. 2.3, then the gradient force will draw the particle toward the focus, while the scattering force will drive the particle along the direction of the laser's propagation. These forces will balance, and the particle will be trapped at a point just beyond the focus of the beam.

Many applications require precise knowledge of the forces felt by a particle in an optical tweezer. In principle, a trap's potential energy profile can be calculated from the optical properties of the trap and the particle. In practice, trapping forces are extremely sensitive to the geometry and composition of the trapped particle and the optical properties of the trap.. Several techniques for measuring the force profile of an optical tweezer are presented in the Appendix.

2.2.2 Practical Considerations

A simple optical tweezer can be built from a laser and a high numerical-aperture microscope objective lens, ($NA \gtrsim 1.2$). Dielectric particles with a wide range of sizes and compositions can be trapped with about a milliwatt of laser light. Ashkin demonstrated the tweezer effect over a wide range of sphere sizes, from $25\,nm$ to tens of micrometers [51]. One must be careful to avoid any electronic or geometrical resonances [52] of the particle, which can introduce a phase lag between the incident

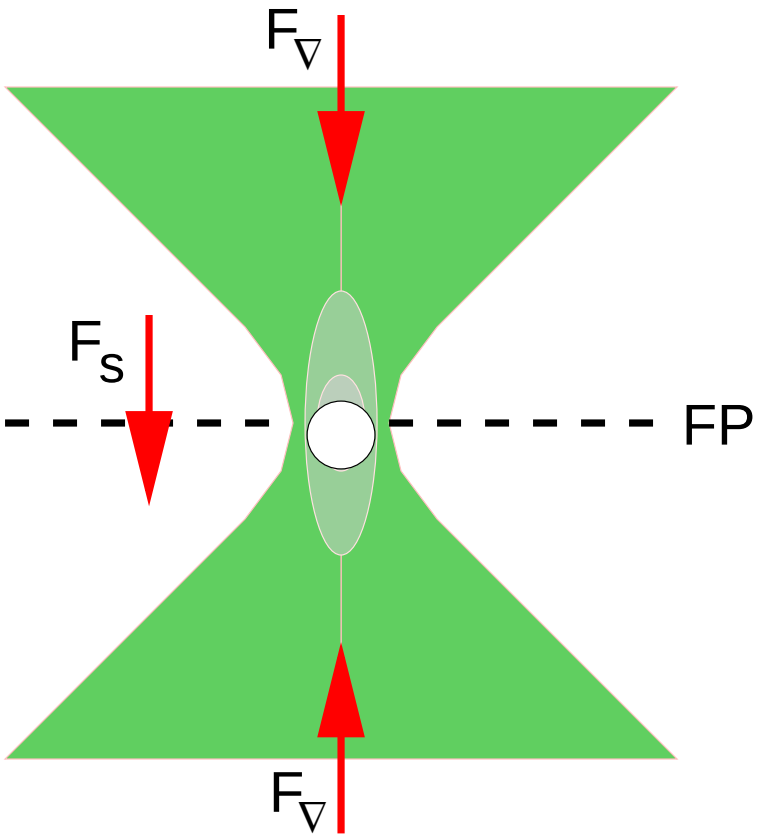

Figure 2.3: *The optical tweezer.* The gradient force, $\vec{F}_{\nabla}$, drives particles towards the focal point of a converging laser beam. The scattering force, $\vec{F}_s$, drives particles along the direction of the laser's propagation. The particle is trapped just beyond the laser's focal plane, **FP**.

electric field and the particle's induced dipole moment, reducing the strength of the gradient force or even reversing its direction. In general, particles that absorb any of the laser's light will be quickly destroyed in the focal point of a conventional optical tweezer, where the laser light is incredibly intense, about $1\,mW/\mu m^2 = 10^9\,W/m^2$. Svoboda has shown, nonetheless, that conventional optical tweezers can trap $35\,nm$ gold Rayleigh particles [53].

While conventional optical tweezers can typically trap only non-absorbing dielectric particles whose dielectric constant is greater than that of the surrounding medium, variats of the optical tweezer can trap a wider range of particles. Sasaki has trapped $3\,\mu m$ iron particles inside an optical cage made by rapidly scanning a simple tweezer in a circle [54]. Rubinsztein-Dunlop has shown that micron-sized absorbing particles can be trapped in dark optical traps created from optical vortex modes [55]. The same group has recently demonstrated that micron-sized birefringent particles trapped with circularly polarized light experience large torques which rotate the particles at rates over $350\,Hz$ [56].

While a simple optical tweezer requires only a laser and an objective lens, a few more optical elements are typically added to the optical train for imaging and steering. One can simultaneously trap and image colloidal particles by adding a dichroic mirror, which reflects the laser light and transmits the rest of the optical spectrum to a CCD camera, as shown in Fig. 2.4. One can steer the tweezer through the objective's field of view by adding a simple two-lens telescope and a beam-steering device, such as a gimbal mounted mirror, Fig. 2.4. The telescope should image the output plane of the beam steering device onto the back aperture of the microscope objective lens.

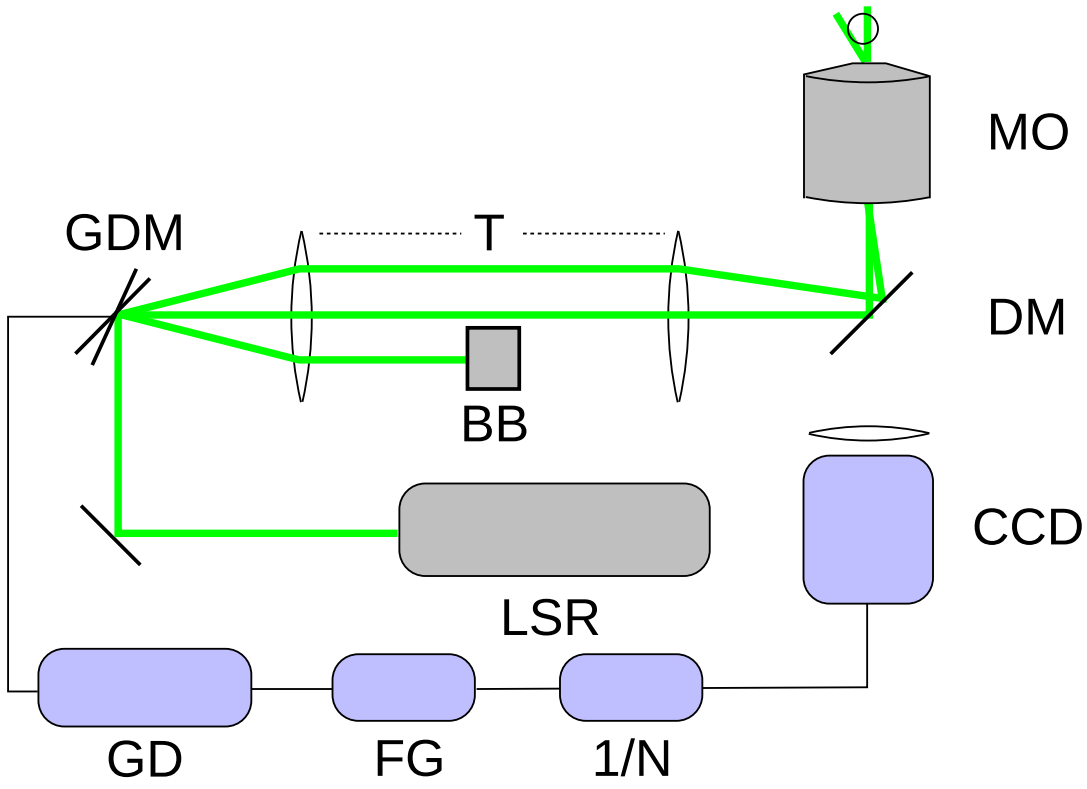

Figure 2.4: *Blinking optical tweezer apparatus.* A Coherent Verdi diode-pumped solid-state laser, **LSR**, emits 10 to 5000 mW of green light, $\lambda = 532\,nm$. A galvanometer-driven mirror, **GDM** deflects the beam. A 3 : 2 Keplerian telescope, **T**, made of two plano-convex lenses, $f = 300,\ 200\,mm$, projects an image of the surface of the GDM onto the back aperture of the microscope objective lens, **MO**. The objective lens focuses the laser into an optical tweezer. A dichroic mirror, **DM**, reflecting $\lambda = 532\,nm$, allows for simultaneous trapping and imaging by a CCD camera, **CCD**. The tweezer is extinguished by steering the laser beam onto a beam block, **BB**. The steering mirror, GDM, is controlled by a galvanometer driver, **GD**, Cambridge Technology, 603X Dual-Axis Mirror Positioning System. The galvanometer driver positions the mirror in proportion to a voltage signal provided by a function generator, **FG**. The function generator can be triggered by a sync pulse, emitted by the CCD camera and processed by a divide by N counter, **1/N** .

There are several schemes for creating multiple optical tweezers. Most simply, N tweezers can be made by separately focusing N laser beams with one microscope objective lens. If these N beams are created from a single laser with multiple beam splitters [35, 57], this technique becomes prohibitively cumbersome and expensive when N is much larger than two. Alternatively, the interference pattern of N beams can trap many more than N particles [58–60]. Indeed, the interference patterns of several laser beams can create hundreds of bright spots whose lateral intensity gradients attract particles. However, the axial intensity gradients near these bright spots are too weak to overcome radiation pressure and particles can only be trapped against a wall. The overall layout of traps is limited to highly symmetric arrangements, and the optical train is extremely difficult to align.

Time-sharing has become the standard method for generating several traps from a single laser. A rapidly moving optical tweezer can create a time-averaged intensity pattern capable of trapping many spheres. If the tweezer oscillates rapidly between a number of positions where it pauses briefly, the time-averaged intensity pattern is dominated by several bright spots each of which functions as a conventional optical tweezer. It is essential that the tweezer's velocity between traps, v, is much greater than the maximum velocity that the particle can follow. A sphere's maximum velocity in a tweezer is determined by the balance of optical and hydrodynamic forces. Therefore, the tweezer's velocity between traps must satisfy $v \gg F_{max}/(6\pi\eta a)$, where F_{max} is the maximum force exerted by the tweezer. The tweezer's velocity also limits the total number of traps, since the period of the tweezer's trajectory must be less than the time it takes the sphere to diffuse from a trap. If the tweezer is steered by galvanometer-driven mirrors, then time sharing techniques cannot make more than ten traps. Using accousto-optic deflectors to steer the trapping beam

[61], one can create up to one hundred independent traps. We use time sharing techniques to create two blinking optical tweezers for measuring interactions between colloidal particles, Fig. 2.4.

Alternatively, if the tweezer moves without resting along its path, the time-averaged intensity profile will be smooth, and can trap particles all along the tweezer's trajectory. Crocker [31] has trapped a few particles on a scanned line, and Sasaki [46, 47] has trapped dozens of particles in more complicated patterns. Continuous patterns have weak intensity gradients and typically form very weak traps. To mitigate these weaker trapping forces, particles must be trapped near walls [31] or in highly viscous fluids [46, 47].

In Chapter 4, we present methods for trapping thousands of particles in arbitrary configurations using holographic techniques.

2.3 Blinking Optical Tweezers

DVM and optical tweezers can be combined into sensitive and efficient probes of the dynamics of colloidal systems, offering substantial improvements over passive observations. For example, pairwise interaction potentials can be extracted from passive observations of the equilibrium structure of dilute suspensions [62–64]. Liquid structure theory [65] provides the framework to analyze this data by relating the interaction potential to the two-point correlation function of the particle density. In principle, this technique can return precise results for weakly interacting particles. In practice, these experiments require enormous amounts of data and can only be executed in confined geometries where the particles are restricted to move within the nearly two dimensional focal volume of a microscope objective. Alternatively,

Crocker and Grier have used *blinking optical tweezers* to measure pairwise interactions [23, 35, 36]. Their non-equilibrium technique requires much less data, can measure interactions at small separations where interactions are very strong, and does not require geometrical confinement.

Generally, blinking optical tweezers can precisely measure the dynamics of a colloidal system near a particular configuration [33]. First, optical tweezers trap and arrange the particles, Fig. 2.5. Then the tweezers are extinguished and the particle trajectories are recorded while the particles freely diffuse and interact. As time passes, the particles tend to diffuse away from their initial configuration. Before they travel too far, the tweezers turn back on and return the particles to their initial positions. Repeating this process many times makes it possible to characterize the statistical fluctuations of the system from near initial configuration. Crocker analyzed this information to extract the electrostatic and hydrodynamic interactions between pairs of colloidal spheres [23, 36]. In Chapter 3, we use blinking optical tweezers to study the hydrodynamic interactions of colloidal particles in confined geometries.

We have built a second-generation blinking optical tweezers system to rapidly measure the interactions between particles under computer control with minimal geometrical projection errors. The tweezers are turned on and off by steering the beam from the microscope objective lens to a beam block with a galvanometer-driven mirror, Fig. 2.4. A timing circuit synchronizes the blinking of the tweezer with the exposure of the video frames, Fig. 2.6. Multiple optical tweezers are created using the time-sharing technique. Small displacements of the galvanometer-driven mirror translate the optical tweezer in the focal plane of the objective lens. The galvanometer-driven mirror positions the tweezer in proportion to a control volt-

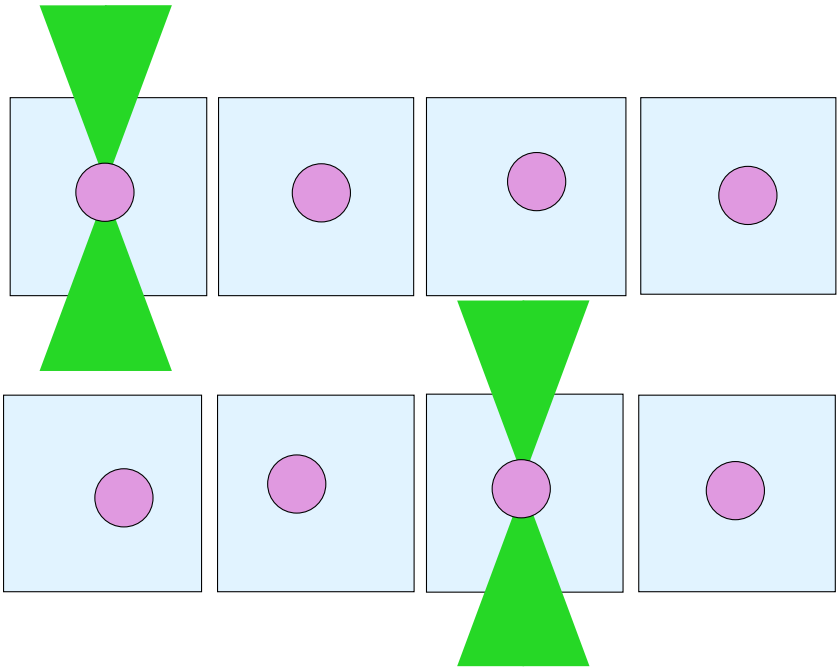

Figure 2.5: *Blinking optical tweezer measurement.* An optical tweezer traps a particle. The tweezer releases the particle and the dynamics of the free particle are recorded. Before the particle can diffuse too far, the trap returns the particle to is initial position, and the process is repeated. Each box represents successive video fields.

age applied by a function generator. A personal computer calculates the trajectory needed to produce a particular arrangement of traps and transfers this information to the function generator. In our experiments, tweezers trap particles for somewhat less than $1/60\,sec$, during the exposure time of one video field. The tweezers are then extinguished for five fields, $5/60\,sec$. Our digital video capture system, Fig. 2.1, records all of these images, with and without the tweezer. Image processing algorithms implemented in IDL, identify and reject all the images where the tweezer is on, while locating and tracking freely diffusing particles when the tweezer is off. Between tweezer bursts, the particle trajectories are sampled 5 times, at $1/60\,sec$ intervals. These trajectories are analyzed to reveal the underlying physics.

2.3.1 Brownian Motion of a Single Colloidal Particle

As a simple example of blinking optical tweezer techniques, we measure the diffusion coefficient of a single Brownian sphere. In this experiment, one micron diameter silica spheres, ($a = (0.495 \pm 0.025)\mu m$, Duke Scientific, Cat. No. 8100) are suspended in water at $T = (29.00 \pm 0.01)°\mathrm{C}$, while a blinking optical tweezer repeatedly traps and releases a single sphere. DVM images and tracks the sphere for 400 *sec*, yielding about 4000 trajectories, each with five time steps. These trajectories are analyzed to calculate $P(\Delta x, \tau)$, the probability that the particle will move a distance Δx along one dimension in a time τ. Our ensemble of five-point trajectories provides samples of Δx for 4 time intervals, $\tau = 1/60$, $2/60$, $3/60$, and $4/60\,sec$. Since these time intervals are all much longer than the system's viscous relaxation time, which is about $0.1\,\mu sec$, each displacement is independent. Therefore, each five-point trajectory provides 4, 3, 2, and 1 independent samples of particle dis-

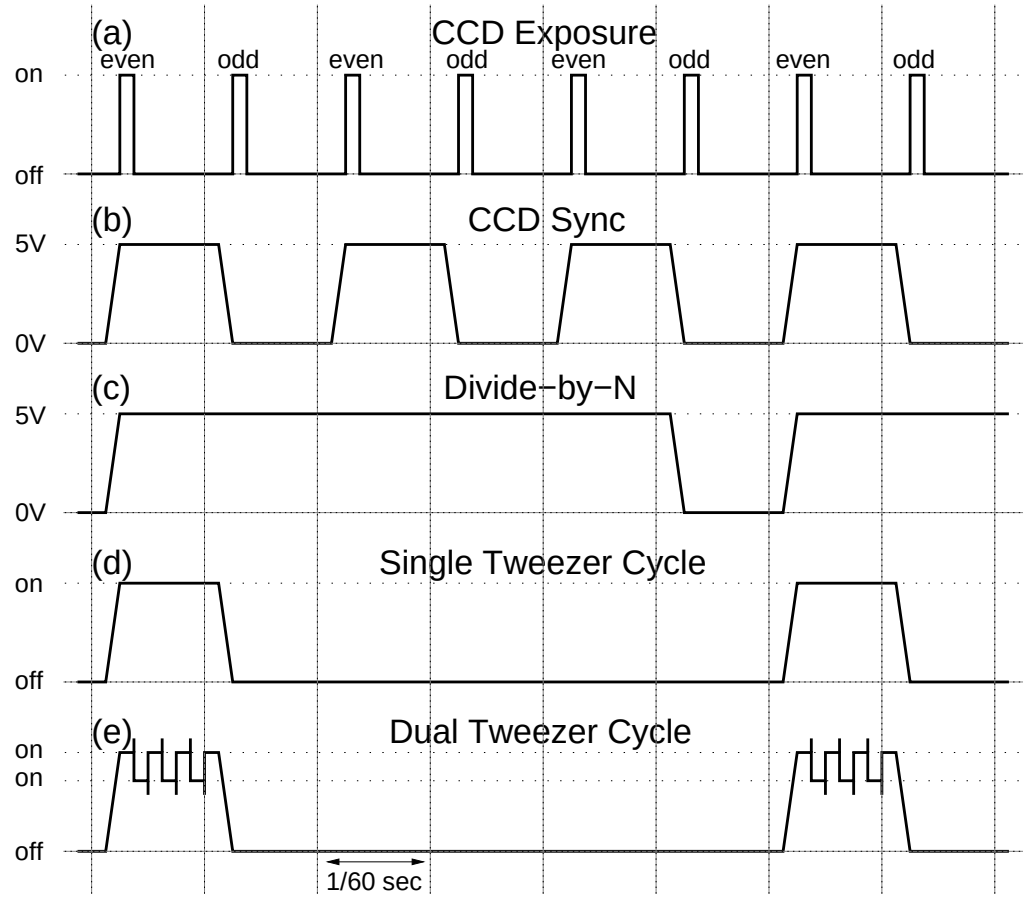

Figure 2.6: *Synchronization of tweezer and camera. (a)* The CCD camera exposes a field every $1/60\,sec$. *(b)* The CCD camera outputs a sync signal, where leading edges encode the exposure of an even field. *(c)* A divide-by-N counter outputs a leading edge every N frames, here N=3. *(d)* The leading edge of the divide-by-N signal triggers a function generator to output a burst that is amplified by the galvanometer driver, and steers the tweezer from its beam block. *(e)* Two tweezers can be made by alternating the tweezer between two "on" positions.

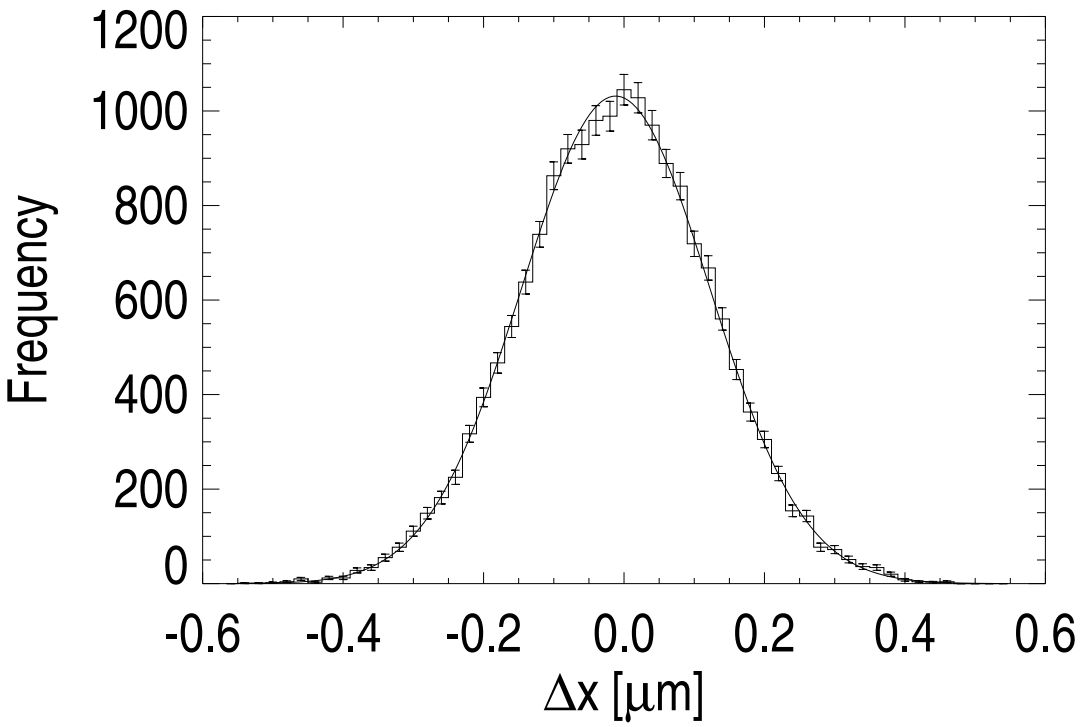

Figure 2.7: *Distribution of one dimensional displacements,* Δx. $\tau = 1/60\,sec$. Fit to Eq. 1.4.

placements for $\tau = 1/60$, $2/60$, $3/60$, and $4/60\,sec$, respectively. Fig. 2.7 shows $P(\Delta x, 1/60\,sec)$, the probability distribution of one dimensional displacements for $\tau = 1/60\,sec$. As predicted by Eq. 1.4, the distribution is well fit by a Gaussian of width $\sigma^2 = \langle \Delta x(\tau)^2 \rangle = (0.0179 \pm 0.0002)\,\mu m^2$. This calculation is repeated for each time-step to generate the mean-squared displacement as a function of time, plotted in Fig. 2.8. As predicted by Eq. 1.17, the displacements are well fit by a straight line through the origin, $\langle \Delta x(\tau)^2 \rangle = 2D\tau$. The slope of this line gives a diffusion coefficient $D = (0.54 \pm 0.01)\,\mu m^2/sec$, which agrees with the Stokes-Einstein prediction, Eq. 1.11, $D = k_B T/(6\pi\eta a) = (0.55 \pm 0.03)\,\mu m^2/sec$. In the next chapter, this sort of blinking optical tweezer measurement is applied to study the hydrodynamic coupling of Brownian spheres.

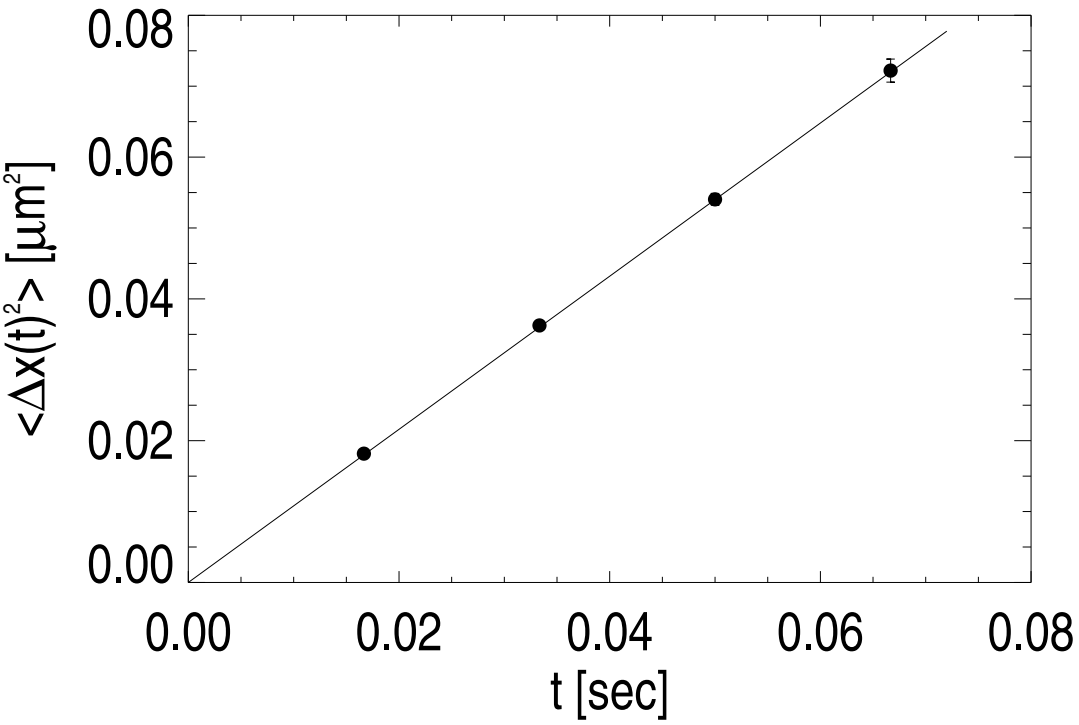

Figure 2.8: *One-dimensional mean-squared displacement versus time.*

CHAPTER 3

WEAK HYDRODYNAMIC COUPLING OF MANY-PARTICLE COLLOIDAL SYSTEMS

Brownian motion dominates the dynamics of individual colloidal particles. These random motions are driven by microscopic collisions with individual solvent molecules and are moderated by hydrodynamic coupling to the solvent's macroscopic flow-field. Einstein quantified this relationship, showing that the diffusion coefficient of an isolated colloidal sphere is proportional to both the available thermal energy and the particle's hydrodynamic mobility, $D = k_B T\, b$. For a single sphere in an unbounded fluid, the mobility has the simple Stokes form and the corresponding diffusion coefficient is $D = k_B T/(6\pi\eta a)$. Interactions with other particles and bounding surfaces modify the sphere's flow-field, affecting its mobility and diffusivity. Because these flows are prohibitively difficult to calculate, even for quite simple systems of particles and bounding surfaces, many phenomena in hydrodynamically coupled colloidal suspensions still defy even qualitative explanation. For example, shear flows can drive both the melting or freezing of colloidal crystals [66, 67]. Hydrodynamic interactions in suspensions of sedimenting colloidal particles can create highly correlated and seemingly divergent fluctuations in sedimentation velocity [68–70]. Hydrodynamic coupling strongly modifies colloidal particles' electrophoretic mobility leading to a panoply of pattern-forming instabilities in dense suspensions [24, 71–74]. Recently, Squires [75] has suggested that some observed

like-charged attractions between colloidal particles[25] may be hydrodynamic rather than electrostatic in origin. As a step toward understanding some of these more complex phenomena, we turn our attention to a few simple systems whose behavior sheds new light on the more general problem of hydrodynamic coupling in colloidal suspensions.

After describing the basic laws that govern colloidal hydrodynamics, we introduce a general formalism for describing the weakly coupled Brownian motion of many spheres. We then apply this formalism to explain trends observed in precise measurements of colloidal hydrodynamic coupling near one wall and between two walls.

3.1 Low Reynolds Number Hydrodynamics

Hydrodynamic interactions can couple the motions of otherwise non-interacting colloidal particles. As particles move through a fluid, they create long-ranged hydrodynamic flows which can couple to the motions of other particles. In this section, we present the mathematical formalism describing hydrodynamic flows, how moving particles create these flows, and how these flows drive the motions of particles.

Hydrodynamic flows are described by their velocity and pressure fields, $\vec{u}$ and p. The Navier-Stokes equation relates the velocity and pressure fields of incompressible Newtonian fluids:

$$\rho\Big(\frac{\partial \vec{u}}{\partial t} + (\vec{u}\cdot\vec{\nabla})\vec{u}\Big) = -\vec{\nabla}p + \eta\nabla^2\vec{u}, \tag{3.1}$$

where ρ and η are the fluid's density and viscosity, respectively. An analog to Newton's second law, Eq. 3.1 describes how pressure and velocity gradients exert

forces on fluid elements, changing their momenta. The relative strengths of these forces are clarified by rewriting Eq. 3.1 in dimensionless form. Rescaling velocity, length and time by characteristic values, U, L and L/U, Eq. 3.1 can be rewritten as [21],

$$Re\Big(\frac{\partial \vec{u}'}{\partial t'} + (\vec{u}' \cdot \vec{\nabla}')\vec{u}'\Big) = -\vec{\nabla}' p' + \eta \nabla'^2 \vec{u}', \tag{3.2}$$

where the primes indicate rescaled variables, and the Reynolds number,

$$Re = \frac{\rho U L}{\eta}. \tag{3.3}$$

compares the relative influence of inertial and viscous effects. When the Reynolds number is much less than one, the inertial terms of the left-hand side of the Navier-Stokes equation can be ignored and

$$\vec{\nabla} p = \eta \nabla^2 \vec{u}. \tag{3.4}$$

Combined with the mathematical statement of incompressibility,

$$\vec{\nabla} \cdot \vec{u} = 0, \tag{3.5}$$

and the no-slip boundary condition, Eq. 3.4 completely describes the flow fluids at low Reynolds number. Eqs. 3.4 and 3.5 are referred to as the *Stokes equations* [76].

Hydrodynamic flows in colloidal systems have very small Reynolds numbers and are well described by the Stokes equations. This can be seen by applying Eq. 3.3 to calculate the range of Reynolds numbers encountered in typical experiments. Taking

the characteristic length scale of fluid flow to be the size of a colloidal particle, L can vary from about $1\,nm$ to $1\,\mu m$. Colloidal particles are typically suspended in water at room temperature, with a density of about $10^3\,kg/m^3$ and a viscosity of about $10^{-3}\,Nsec/m^2$. Fluid velocities vary from about $1 - 100\,\mu m/s$. Therefore, the Reynolds numbers of colloidal systems vary from about 10^{-9} to 10^{-4}.

Many techniques have been developed to solve the Stokes equations, but Green's function techniques are a convenient choice for colloidal systems [21, 77]. One obtains the Green's function for a particular arrangement of fixed surfaces by conceptually applying a unit force in the β direction at the origin, and solving the Stokes equations,

$$\vec{\nabla} p = \eta \nabla^2 \vec{u} + \delta(\vec{r})\hat{\beta}, \tag{3.6}$$

for the resulting fluid velocity in a direction α at an arbitrary point of observation $\vec{r}$. The result for an unbounded fluid,

$$G^S_{\alpha\beta}(\vec{r}) = \frac{1}{8\pi\eta}\left[\frac{\delta_{\alpha\beta}}{r} + \frac{r_\alpha r_\beta}{r^3}\right], \tag{3.7}$$

is called a *Stokeslet*. Since the Stokes equations are linear, flow-fields created by forces exerted by finite objects can be calculated by integrating the Green's function, Eq. 3.7, over the surface of the object [78]. Care must be taken to match the fluid's velocity with the object's velocity at the object's surface. However, boundary effects can be ignored when the observer is far away from the object applying the force, $r \gg a$. In this case, the flow-field is well described by the Stokeslet itself, Eq. 3.7.

Conversely, the Green's function technique can be applied to find the force on an object in an existing flow. If a sphere of radius a is immersed in a viscous fluid whose velocity field is $\vec{u}_o(\vec{r})$ in the absence of the sphere, then the sphere will experience a force,

$$\vec{F} = 6\pi\eta a[(\vec{u}_o(\vec{x}) - \vec{v}) + \frac{a^2}{6}\nabla^2\vec{u}_o(\vec{x})], \tag{3.8}$$

where $\vec{v}$ is the sphere's velocity and $\vec{x}$ is the position of its center. This expression is referred to as Faxen's first law. In a uniform external velocity field, Faxen's first law reduces to the familiar Stokes result,

$$\vec{F} = 6\pi\eta a\ (\vec{u}_o - \vec{v}). \tag{3.9}$$

Eqs. 3.7 and 3.8 together describe how hydrodynamic interactions can couple the motions of otherwise non-interacting colloidal particles, with Eq. 3.7 describing how a particle's motions excite long-ranged flows and Eq. 3.8 describing how these flows can influence the motions of other particles. In the next section, we apply this theoretical framework to formulate a theory describing the coupled Brownian motion of otherwise noninteracting spheres.

3.2 Theory of Coupled Brownian Motion

3.2.1 Generalizing Fick's Laws

Consider a system of N colloidal spheres whose motions are coupled through hydrodynamic interactions. The probability of finding the spheres in a particular

configuration, $\{\vec{r}_1, \ldots, \vec{r}_N\}$, is given by a distribution function $P(\vec{r}_1, \ldots, \vec{r}_N)$. Gradients of $P(\vec{r}_1, \ldots, \vec{r}_N)$ drive fluxes of particles, as described by a generalization of Fick's first law,

$$J^D_{i\alpha}(\vec{r}) = -D_{i\alpha,j\beta}\, \partial_{j\beta} P, \tag{3.10}$$

where $D_{i\alpha,j\beta}$ is the component of the diffusivity tensor, $\mathbf{D}$, which describes the ensemble-averaged flux of the ith particle in the α direction due to gradients of the jth particle's probability density in the β direction. Off-diagonal terms in $\mathbf{D}$ reflect correlated motions among the particles and vanish for noninteracting particles. In writing Eq. 3.10, we have adopted the the summation convention for repeated indices. The conservation of probability requires that fluxes of particles must be matched by flows in the probability distribution,

$$\frac{\partial P}{\partial t} = -\partial_{i\alpha} J_{i\alpha}. \tag{3.11}$$

If the particles only interact hydrodynamically, then $J_{i\alpha} = J^D_{i\alpha}$, and we can combine Eqs. 3.10 and 3.11 to obtain a generalized version of Fick's second law, Eq. 1.3,

$$\frac{\partial P}{\partial t} = \partial_{i\alpha}\, D_{i\alpha,j\beta}\, \partial_{j\beta}\, P. \tag{3.12}$$

If the particles are weakly interacting, the form of the diffusivity tensor does not change much for small particle displacements, and on short timescales

$$\frac{\partial P}{\partial t} = D_{i\alpha,j\beta}\, \partial_{i\alpha}\, \partial_{j\beta}\, P. \tag{3.13}$$

Since $D_{i\alpha,j\beta}$ is symmetric under the interchange of $i\alpha$ and $j\beta$, it can be diagonalized by a set of $3N$ normal coordinates, ψ_ν, which are linear combinations of the single particle coordinates, $\{\vec{r}_1, \ldots, \vec{r}_N\}$,

$$\psi_\nu = a_{\nu,i\alpha}\, r_{i\alpha}. \tag{3.14}$$

In this coordinate system, the diffusion of each coordinate is independent and the diffusion equation, Eq. 3.13, reduces to a $3N$-dimensional analog of Fick's second law for free diffusion, Eq. 1.3,

$$\frac{\partial P}{\partial t} = D_\nu \frac{\partial^2 P}{\partial \psi_\nu^2}. \tag{3.15}$$

Therefore, the system's distribution function takes on the familiar Gaussian form, Eq. 1.4,

$$P(\Delta\psi_1, \ldots, \Delta\psi_{3N}, \tau) = \prod_{\nu=1}^{3N} \frac{1}{\sqrt{4\pi D_\nu \tau}} \exp\Big[\frac{-(\Delta\psi_\nu)^2}{4D_\nu\tau}\Big], \tag{3.16}$$

Just like the single particle coordinates in an uncoupled system, the mean-squared displacements of the normal coordinates increase linearly with time,

$$\langle(\Delta\psi_\nu(\tau))^2\rangle = 2D_\nu\,\tau. \tag{3.17}$$

Applying the coordinate transformation, Eq. 3.14, to the solution, Eq. 3.16, gives the evolution of the probability distribution in single particle coordinates.

$$P(\Delta\vec{r}_1, \ldots, \Delta\vec{r}_N, \tau) \propto \exp\Big[-D^{-1}_{i\alpha,j\beta}\frac{\Delta r_{i\alpha}\,\Delta r_{j\beta}}{4\,\tau}\Big], \tag{3.18}$$

where

$$D^{-1}_{i\alpha,j\beta} \equiv \frac{a_{\nu,i\alpha}\, a_{\nu,j\beta}}{D_\nu} \tag{3.19}$$

and $D^{-1}_{i\alpha,k\gamma} D_{k\gamma,j\beta} = \delta_{i\alpha,j\beta}$. By contributing to the off-diagonal elements of $\mathbf{D}$, coupling causes the displacements of diffusing particles to be correlated [79],

$$\langle \Delta r_{i\alpha}(\tau) \Delta r_{j\beta}(\tau) \rangle = 2 D_{i\alpha,j\beta}\, \tau. \tag{3.20}$$

Eq 3.20 shows that individual particles diffuse regularly, but with modified diffusion coefficients. Comparing Eqs. 3.17 and 3.20, we can relate the diffusivities of the normal modes to the single particle diffusivities,

$$D_\nu = a_{\nu,i\alpha}\, a_{\nu,j\beta}\, D_{i\alpha,j\beta}. \tag{3.21}$$

3.2.2 Generalizing the Stokes-Einstein Relation

We have developed the kinematics of coupled Brownian motion, but we have not yet related the diffusion tensor to the hydrodynamic properties of the system. For simple diffusion, Einstein showed that the diffusion constant is the product of the spheres' mobilities, b, and the thermal energy, $k_B T$. Batchelor [80] generalized Einstein's argument to relate the diffusion tensor, $\mathbf{D}$, to the hydrodynamic mobility tensor, $\mathbf{b}$. In thermal equilibrium, the probability to find the spheres in a particular configuration, $\{\vec{r}_1, \ldots, \vec{r}_N\}$, is given by Boltzmann's distribution,

$$P(\vec{r}_1, \ldots, \vec{r}_N) = \exp\left[\frac{-\Phi(\vec{r}_1, \ldots, \vec{r}_N)}{k_B T}\right], \tag{3.22}$$

where $\Phi(\vec{r}_1, \ldots, \vec{r}_N)$ is the potential energy of the configuration due to interactions among the spheres. For the system to remain in equilibrium, the ensemble-average probability flux of each particle, $\vec{J}_i(\vec{r})$, must be zero at all locations, $\vec{r}$. Each particle's probability flux is the sum of its diffusive flux, $\vec{J}_i^D(\vec{r})$, and its flux due to interactions with the other particles, $\vec{J}_i^I(\vec{r})$. The diffusive flux, $\vec{J}_i^D(\vec{r})$, is given by Eq. 3.10. We now calculate the flux of the ith particle due to interactions with other particles. At low Reynolds number, particles only move when forced. If the particles in a suspension are not coupled, then the average velocity of the ith particle is proportional to the force applied to it, $v_{i\alpha} = bf_{i\alpha}$. In the presence of hydrodynamic coupling, the ith sphere can also move in response to a force applied to the jth particle,

$$v_{i\alpha} = b_{i\alpha,j\beta}\ f_{j\beta}, \tag{3.23}$$

where $b_{i\alpha,j\beta}$ is the component of the mobility tensor, $\mathbf{b}$, which describes the α component of the ith particle's velocity when a unit force is applied to the jth particle in the β direction. Since the system is in thermal equilibrium, the force on the jth particle, $f_{j\beta} = -\partial_{j\beta}\Phi(\vec{r}_1, \ldots, \vec{r}_N)$, can be expressed in terms of the probability distribution, P,

$$f_{j\beta} = k_B T \frac{\partial_{j\beta} P}{P}. \tag{3.24}$$

Since $\vec{J}(\vec{r}) = P(\vec{r})\ v(\vec{r})$, we can combine the above results to obtain the interaction-mediated flux,

$$J^I_{i\alpha}(\vec{r}) = k_B T\, b_{i\alpha,j\beta}\, \partial_{j\beta} P \tag{3.25}$$

Combining Eqs. 3.10 and 3.25 with the statement of equilibrium, $\vec{J}^D_i(\vec{r}) + \vec{J}^I_i(\vec{r}) = 0$, we find the generalized Stokes-Einstein relation

$$\mathbf{D} = k_B T\, \mathbf{b}. \tag{3.26}$$

In order to calculate the diffusivity tensor, we must first formulate the particles' hydrodynamic interactions.

3.2.3 Stokeslet Analysis

In principle, the mobility tensor, $\mathbf{b}$, can be calculated by solving the Stokes equations, Eqs. 3.4 and 3.5. However, the Stokes equations can only be solved in closed form for the simple case of a free sphere, Eq. 3.8. Asymptotic expressions are available for two spheres, for one sphere near a wall, and for a few highly symmetric configurations of other few-body systems [76].

However, in the limit of weak coupling, *Stokeslet analysis* [70, 77]can describe the hydrodynamic interactions between arbitrary numbers of free and confined particles. Stokeslet analysis approximates the flow-field due to each sphere in a suspension as that due to a point force. Faxen's first law then enables us to calculate the response of each sphere to the flow-field generated by all others.

Consider two spherical colloidal particles, i and j, separated by a distance much greater than their radii. The mobility tensor, $b_{i\alpha,j\beta}$, has two terms,

$$b_{i\alpha,j\beta} = \frac{\delta_{i\alpha,j\beta}}{6\pi\eta a} + b^e_{i\alpha,j\beta}. \tag{3.27}$$

The first term is self mobility of the ith sphere, and the second term describes the external contribution due to interactions with the jth particle. Since the spheres are well-separated, a force applied by the jth sphere can be modeled as a point-like force, as shown in Fig. 3.1. Therefore, the jth sphere's flow at the location of the ith particle is given by a Stokeslet, $G^S_{\alpha,\beta}(\vec{r}_i - \vec{r}_j)$. Faxen's law, Eq. 3.8, describes how the ith particle responds to this flow. Retaining only first-order terms in a/r, one finds that the ith sphere moves with the local fluid velocity, $v_{i\alpha} = G^S_{\alpha,\beta}(\vec{r}_i - \vec{r}_j)$. Therefore, the external contribution to the ith sphere's mobility due to interactions with the jth particle is approximately

$$b^e_{i\alpha,j\beta} = G^S_{\alpha,\beta}(\vec{r}_i - \vec{r}_j). \tag{3.28}$$

The downside of this approximation is that the calculated flows do not satisfy no-slip boundary conditions at the sphere's surfaces. The upside is that contributions to the mobility from different spheres add linearly. Thus we are able to calculate the dynamical properties of arbitrary arrangements of well-separated particles. We apply this formalism in the following sections to interpret measurements of hydrodynamic coupling in colloidal suspensions.

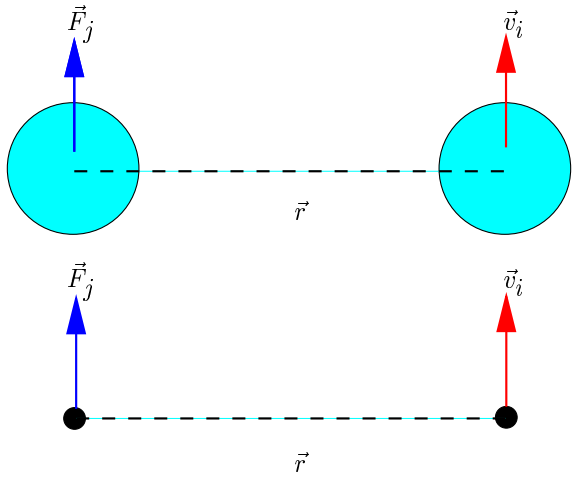

Figure 3.1: *Stokeslet approximation of hydrodynamic interactions.* To calculate the hydrodynamic interaction of two colloidal spheres, we model each sphere as a point particle.

3.3 Coupled Brownian Motion of Two Spheres

Let us apply Stokeslet analysis to calculate the diffusivity tensor of two identical weakly-coupled spheres, located at $\vec{r}_1$ and $\vec{r}_2$. The spheres are separated by a displacement $\vec{r} = \vec{r}_2 - \vec{r}_1$ which is much larger than their radii, $a/r \ll 1$. Thus Eqs. 3.7 and 3.28 imply that the components of the mobility tensor are,

$$b_{i\alpha,j\beta} = \frac{\delta_{i\alpha,j\beta}}{6\pi\eta a} + \frac{(1-\delta_{ij})}{8\pi\eta}\left[\frac{\delta_{\alpha\beta}}{r} + \frac{r_\alpha r_\beta}{r^3}\right] \tag{3.29}$$

where i and j are either 1 or 2.

Diagonalizing the mobility tensor yields four normal modes [80]: two collective modes, $\Delta\rho_{\parallel,\perp}$, and two relative modes, $\Delta R_{\parallel,\perp}$,

$$\Delta\rho_{\parallel} = \hat{R}\cdot\Delta\vec{\rho} = \Delta(x_2+x_1)/2, \tag{3.30}$$

$$\Delta R_{\parallel} = \hat{R}\cdot\Delta\vec{R} = \Delta(x_2-x_1)/2, \tag{3.31}$$

$$\Delta\rho_{\perp} = (\mathbf{1}-\hat{R}\hat{R})\Delta\vec{\rho} = \Delta(y_2+y_1)/2, \tag{3.32}$$

$$\Delta R_{\perp} = (\mathbf{1}-\hat{R}\hat{R})\Delta\vec{R} = \Delta(y_2-y_1)/2, \tag{3.33}$$

where $\vec{\rho} = (\vec{r}_2+\vec{r}_1)/2$, $\vec{R} = (\vec{r}_2-\vec{r}_1)/2$, and the second equality in each equation gives the form of each coordinate in the special case where the spheres are confined to move in two dimensions, and the spheres are initially separated by $\vec{r} = r\hat{x}$. We can now apply the generalized Stokes-Einstein relation and Eq. 3.21 to calculate the modes' diffusivities:

$$D_{\parallel}^{\rho,R} = k_BT(b_{1x,1x}+b_{2x,2x}\pm b_{1x,2x}\pm b_{2x,1x})/4, \tag{3.34}$$

$$D_{\perp}^{\rho,R} = k_BT(b_{1y,1y}+b_{2y,2y}\pm b_{1y,2y}\pm b_{2y,1y})/4, \tag{3.35}$$

where sums apply to the collective modes and the differences apply to the relative modes. Applying Eq. 3.29 to these expressions for the diffusivities yields:

$$D_{\parallel}^{\rho,R}(r) = \frac{D_o}{2}\left[1\pm\frac{3}{2}\frac{a}{r}+\mathcal{O}\left(\frac{a^3}{r^3}\right)\right], \tag{3.36}$$

$$D_{\perp}^{\rho,R}(r) = \frac{D_o}{2}\left[1\pm\frac{3}{4}\frac{a}{r}+\mathcal{O}\left(\frac{a^3}{r^3}\right)\right], \tag{3.37}$$

where the positive corrections apply to collective modes and the negative to relative modes, and $D_o = k_BT/(6\pi\eta a)$. The collective diffusion coefficients, $D_{\parallel}^{\rho}$ and $D_{\perp}^{\rho}$,

are enhanced by hydrodynamic coupling because the flow-field due to the motion of one sphere moves in the same direction as the other sphere. Conversely, relative diffusion coefficients, $D_{\parallel}^{R}$ and $D_{\perp}^{R}$, are suppressed because the flow-field due to the motion of one sphere opposes the motion of the other sphere.

Batchelor [80] calculated expressions for $D_{\parallel,\perp}^{\rho,R}$ to fifth order in a/r, including the finite size of the spheres and their distortions of each other's fields:

$$D_{\parallel}^{\rho,R}(r) = \frac{D_o}{2}\left[1 \pm \frac{3}{2}\frac{a}{r} \mp \left(\frac{a}{r}\right)^3 - \frac{15}{4}\left(\frac{a}{r}\right)^4 + \mathcal{O}\left(\frac{a^6}{r^6}\right)\right], \tag{3.38}$$

$$D_{\perp}^{\rho,R}(r) = \frac{D_o}{2}\left[1 \pm \frac{3}{4}\frac{a}{r} \pm \frac{1}{2}\left(\frac{a}{r}\right)^3 + \mathcal{O}\left(\frac{a^6}{r^6}\right)\right], \tag{3.39}$$

Crocker measured the dependence of these four diffusive modes on the separation of the spheres using blinking optical tweezers [36], and found good agreement with Batchelor's result. If agreement between measured and calculated diffusivities rely on retaining the highest order terms in Batchelor's expansion, then we might be concerned that Stokeslet analysis' first-order result might fare poorly when compared with measurements.

We measured the relative diffusion coefficients of two one micron diameter silica spheres ($a = (0.495 \pm 0.025)\,\mu m$, Duke Scientific, Cat. No. 8100), using the second generation blinking optical tweezers setup described in Chapter 2. The spheres were suspended in a 2mM aqueous solution of NaCl at $T = (29.00 \pm 0.01)^{\circ}C$. The salt was added to the solution to reduce the Debye screening length to $7\,nm$, minimizing the electrostatic interactions between the spheres. The solution was sandwiched between a microscope slide and a #1 coverslip which were stringently cleaned with an acid-peroxide wash, and sealed with a UV-cured epoxy (Norland type 88). The microscope slide and cover slip were separated by $(140 \pm 2)\,\mu m$. A pair of blinking

optical tweezers repeatedly trapped the spheres in a plane $25\,\mu m$ from the nearest glass surface, and continuously varied the separation of the spheres from 2 to $10\,\mu m$. The tweezers were periodically extinguished for $83\,ms$, and the trajectories of the spheres were analyzed to extract the diffusivities of the four modes, as described as Chapter 2. The measured diffusivities appear in Fig. 3.2 with the Stokeslet predictions of Eqs. 3.36 and 3.37 and Batchelor's higher-order predictions, Eqs. 3.38 and 3.39, all with no adjustable parameters. Not only do both the Stokeslet and higher-order solutions capture all trends in the measurements, but they also agree remarkably well with each other. Apparently Batchelor's higher-order corrections are not needed, even when the spheres approach one another within four radii. As long as Batchelor's higher-order corrections are irrelevant, the particles' mobilities may be added according to Eq. 3.27. This in turn suggests that Stokeslet analysis can be scaled to dilute suspensions with arbitrary numbers of particles.

3.4 Brownian Motion of One Sphere near a Wall

In many cases of practical and fundamental interest, Brownian particles interact not only with each other, but also with the walls of their container. The next two sections develop the method of hydrodynamic images through which Stokeslet analysis can be used to calculate the influence of bounding walls on colloidal spheres' dynamics. A wall resists the flow-field accompanying the motion of nearby particles, reducing their mobilities. Faxen calculated an asymptotic expansion for the mobility of a sphere near a planar boundary in 1927 [76]. This expansion has been verified experimentally for Brownian spheres by Pralle [81] and Lin [82].

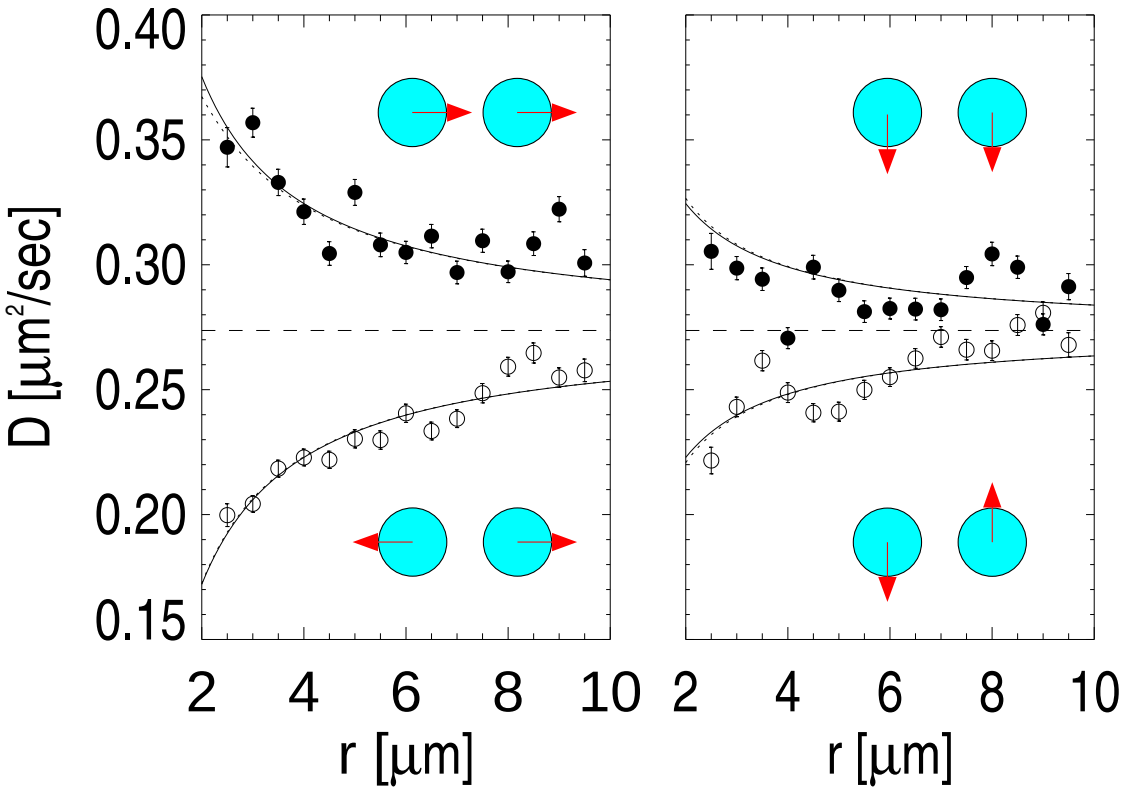

Figure 3.2: *The coupled diffusion of two spheres. Clockwise from top left* $D^{\rho}_{\parallel}$, $D^{\rho}_{\perp}$, $D^{R}_{\parallel}$, $D^{R}_{\perp}$. The solid lines show the Stokeslet prediction, and dotted lines show Batchelor's' higher-order result. Dashed lines show the asymptotic value of the diffusion coefficient. Batchelor's higher-order terms are irrelevant at these length scales.

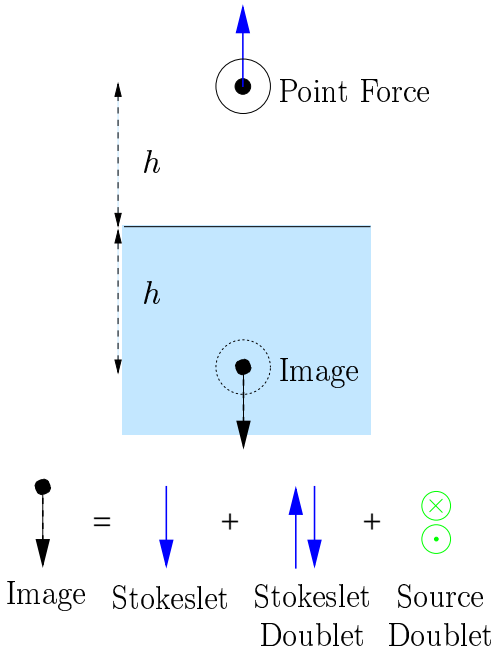

Figure 3.3: *Image system for one sphere near a planar wall.*

The Green's function for a point force a distance h above a solid surface must be modified so that the fluid's velocity vanishes on the surface. Lorentz calculated this Green's function in 1896 [83], but Blake later realized that this solution is more easily obtained by the method of images [84]. Blake noted that the wall's no-slip boundary condition is satisfied by canceling the original Stokeslet's flow at the wall with that due to an image system comprised of a Stokeslet (S), a source doublet (D), and a Stokeslet doublet (SD), all placed a distance h below the surface of the wall [77, 84], as shown in Fig. 3.3. The flow due to this image system is described by the Green's function

$$G^W_{\alpha\beta}(\vec{x} - \vec{R}) = -G^S_{\alpha\beta}(\vec{x} - \vec{R}) + 2h^2 G^D_{\alpha\beta}(\vec{x} - \vec{R}) - 2hG^{SD}_{\alpha\beta}(\vec{x} - \vec{R}) \quad (3.40)$$

where $\vec{R} = \vec{r} - 2h\hat{z}$ is the position of Stokeslet's image, and

$$G^D_{\alpha\beta}(\vec{r}) = \frac{1}{8\pi\eta}(1 - 2\delta_{\alpha z})\,\frac{\partial}{\partial r_\beta}\left(\frac{r_\alpha}{r^3}\right) \tag{3.41}$$

$$G^{SD}_{\alpha\beta}(\vec{r}) = (1 - 2\delta_{\alpha z})\,\frac{\partial}{\partial r_\beta} G^S_{\alpha z}(\vec{r}) \tag{3.42}$$

are Green's functions for a source dipole and a Stokeslet doublet, respectively. The external contribution to the mobility of a sphere located at $\vec{r} = h\hat{z}$ is the wall's contribution to the Green's function at $\vec{r}$, $b^e_{\alpha,\beta} = G^W_{\alpha\beta}(\vec{r} - \vec{R})$:

$$b^e_{xx} = b^e_{yy} = \frac{-3}{32\pi\eta\, h} \tag{3.43}$$

$$b^e_{zz} = \frac{-3}{16\pi\eta\, h}, \tag{3.44}$$

All other terms of the mobility tensor are zero.

Therefore, two diffusion coefficients describe this system: $D_\parallel$ for displacements within a plane parallel to the wall, and $D_\perp$ for displacements perpendicular to the wall,

$$D_\parallel(h) = D_o\left[1 - \frac{9}{16}\,\frac{a}{h} + \mathcal{O}\left(\frac{a^3}{h^3}\right)\right] \tag{3.45}$$

$$D_\perp(h) = D_o\left[1 - \frac{9}{8}\,\frac{a}{h} + \mathcal{O}\left(\frac{a^3}{h^3}\right)\right]. \tag{3.46}$$

Faxen gave an asymptotic expression for $D_\parallel(h)$, satisfying the no-slip boundary condition on the sphere and the wall to fifth order in (a/h) [76],

$$D_\parallel(h) = D_o\left[1 - \frac{9}{16}\,\frac{a}{h} + \frac{1}{8}\left(\frac{a}{h}\right)^3 - \frac{45}{256}\left(\frac{a}{h}\right)^4 - \frac{1}{16}\left(\frac{a}{h}\right)^5 + \ldots\right] \tag{3.47}$$

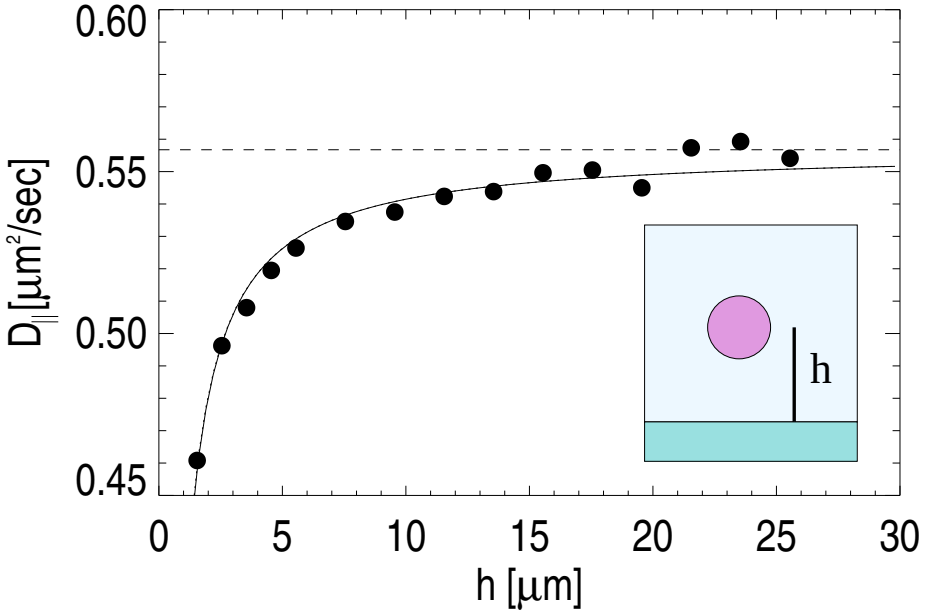

Figure 3.4: *Suppression of mobility near a surface.* The solid circles show the measured in-plane diffusion coefficient of a single sphere, where the radii of the circles indicate the statistical error bars. The solid line plots the Stokeslet prediction, Eq. 3.45. A dotted line plots Faxen's higher-order result, but is almost perfectly obscured by the Stokeslet prediction.

Using the same experimental apparatus described in Section 3.3, we measured the in-plane diffusion coefficient of a single sphere near a glass wall. In these experiments, the galvanometer-driven mirror generated only one blinking optical trap whose height above the surface of the wall was varied in from 1.5 to 25 μm by translating the microscope objective along its optical axis. The measured values of $D_{\parallel}(h)$ are plotted in Fig. 3.4, along with the Stokeslet predictions and Faxen's series expansion. Once again, we see that higher-order corrections are not needed to describe the hydrodynamic coupling of a sphere to a nearby wall at these length-scales. In the following sections, we describe how this result can be extended to

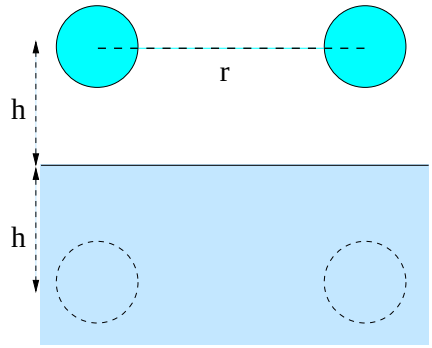

Figure 3.5: *Two spheres near a wall and their images.*

understand the diffusion of many spheres near one wall, and to the considerably more complex problem of a single sphere between two parallel walls.

3.5 Coupled Brownian Motion of Two Spheres near a Wall

Consider the Brownian motion of two spheres near a planar surface, Fig. 3.5. When the spheres are far from the wall, their coupled diffusion should be described adequately by Eqs. 3.36 and 3.37. Similarly, when the spheres are much closer to the wall than to each other, the diffusivity of one sphere near a wall, Eqs. 3.45 and 3.46, should describe the behavior of each sphere. At intermediate separations, however, neither set of formulae is accurate. Stokeslet analysis captures the behavior of the system over the range of accessible configurations, while predictions based on the linear superposition of drag forces fail [85].

Oseen [76] suggested that the total hydrodynamic drag on each of two spheres near a wall may be approximated by the sum of the drags contributed by the other particle and by the wall. In particular, the total drag on each diffusive mode, ν, is the sum of the free particle drags, the drag due to interactions between the spheres,

and drag due to interactions with the wall,

$$\gamma_\nu(r,h) = \gamma_{o\nu} + [\gamma_\nu(r) - \gamma_{o\nu}] + [\gamma_\nu(h) - \gamma_{o\nu}], \tag{3.48}$$

where $\gamma_{o\nu}$ is the drag on the mode when the spheres are not interacting, $\gamma_\nu(r)$ is the drag due to direct interactions between the spheres, and $\gamma_\nu(h)$ is the drag due to coupling with the wall. Applying the Stokes-Einstein relation, the diffusion coefficient of each mode, $D_\nu(r,h)$ is

$$D_\nu^{-1}(r,h) = D_\nu^{-1}(r) + D_\nu^{-1}(h) - D_{o\nu}^{-1}. \tag{3.49}$$

This result approaches the sphere-sphere, and the sphere-wall formulae as $h \to \infty$ and $r \to \infty$, respectively.

Alternatively, we calculate the diffusivity tensor using Stokeslet analysis. The external contribution to the mobility, $b^e_{i\alpha,j\beta}$, is the α component of the fluid velocity at the position of the ith sphere arising when a unit force is applied in the β direction to the jth sphere. Therefore,

$$b^e_{i\alpha,j\beta} = (1-\delta_{ij})G^S_{\alpha\beta}(\vec{r}_i - \vec{r}_j) + G^W_{\alpha\beta}(\vec{r}_i - \vec{R}_j), \tag{3.50}$$

where each sphere interacts with its own image, the other sphere, and the image of the other sphere. Even though this analysis is only valid to first order in a/r it includes many-body terms ignored by the linear superposition of drag forces. Diagonalizing the mobility tensor shows that the four modes identified in the previous section, $\Delta R_{\parallel,\perp}$, $\Delta\rho_{\parallel,\perp}$, are no longer independent. The normal modes of this systems are shown in Fig. 3.6. The independent modes of motion are rotated

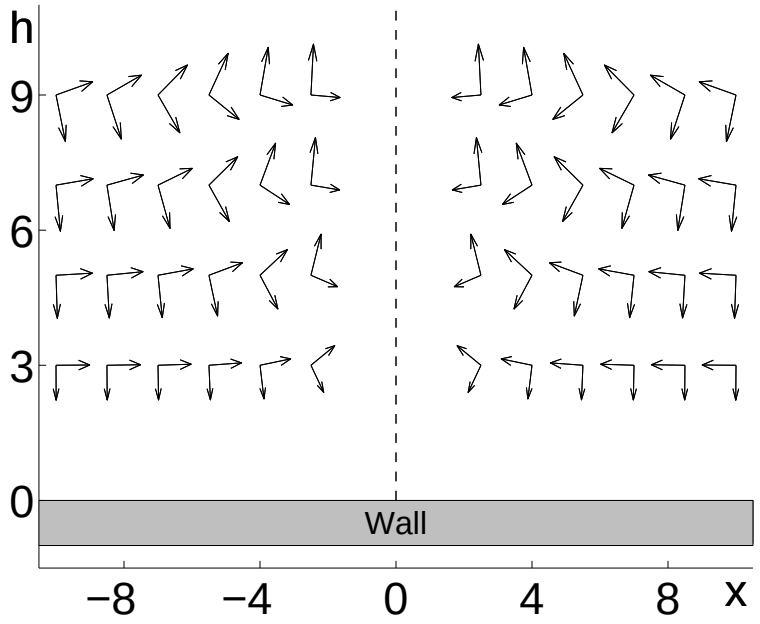

Figure 3.6: *Cross-sectional view of the diffusive modes of two spheres near a wall.* Collective motion normal to the wall becomes increasingly coupled with relative motion parallel to the wall as h approaches r. Collective normal modes at large r cross over continuously to relative parallel modes as r decreases. The dashed line at $x = 0$ indicates the symmetry plane. *Graphic courtesy of Todd Squires.*

with respect to the bounding wall by an amount that depends strongly on both r and h. Even though the experimentally accessible in-plane modes are no longer independent, we can still calculate their diffusivities using Eq. 3.21,

$$D_{\parallel}^{\rho,R} = k_B T(b_{1x,1x} + b_{2x,2x} \pm b_{1x,2x} \pm b_{2x,1x})/4, \tag{3.51}$$

$$D_{\perp}^{\rho,R} = k_B T(b_{1y,1y} + b_{2y,2y} \pm b_{1y,2y} \pm b_{2y,1y})/4, \tag{3.52}$$

where the positive sign corresponds to collective motion, the negative sign to relative motion, and $\hat{x}$ is the direction of the vector connecting the spheres' centers.

Applying Eq. 3.50, we find that to $\mathcal{O}\left(\frac{a^3}{r^3}, \frac{a^3}{h^3}\right)$,

$$D_{\perp}^{\rho,R}(r,h) = \frac{D_o}{2}\left[1 - \frac{9}{16}\frac{a}{h} \pm \frac{3}{4}\frac{a}{r}\left(1 - \frac{1+\frac{3}{2}\xi}{(1+\xi)^{3/2}}\right)\right], \tag{3.53}$$

$$D_{\parallel}^{\rho,R}(r,h) = \frac{D_o}{2}\left[1 - \frac{9}{16}\frac{a}{h} \pm \frac{3}{2}\frac{a}{r}\left(1 - \frac{1+\xi+\frac{3}{2}\xi^2}{(1+\xi)^{5/2}}\right)\right], \tag{3.54}$$

where $\xi = 4h^2/r^2$.

Using the blinking optical tweezer setup described in Section 3.3, we have measured the evolution of these four diffusion coefficients as a function of separation and height above the wall. A pair of blinking optical tweezers repeatedly trapped and released the spheres a height h above a glass wall, while varying their separation, r, from 2 to 10 μm. The height, h, above the wall was varied from 1.6 to 25 μm by translating the microscope objective along its optical axis. Fig. 3.7 shows the four diffusion constants as a function of separation at $h = 1.55\,\mu m$ above a wall. The linear superposition approximation of Eq. 3.58 fares poorly, while the Stokeslet analysis gives quantitatively good predictions. The predictions based on the linear superposition of drag forces become increasingly accurate for increasing ball-ball and ball-wall separations. Stokeslet analysis, on the other hand, does just as well for the entire range of separations considered. To demonstrate this, we plot in Fig. 3.8 the χ^2 deviation of the four diffusivities from their predicted values as a function of height above the wall, where

$$\chi_\nu^2(h) = \frac{1}{N}\sum_{i=1}^{N}\left((D_\nu^{expt}(r_i,h) - D_\nu^{th}(r_i,h))/\sigma_{Di}\right)^2. \tag{3.55}$$

The linear superposition of hydrodynamic drag fails over all distances where cou-

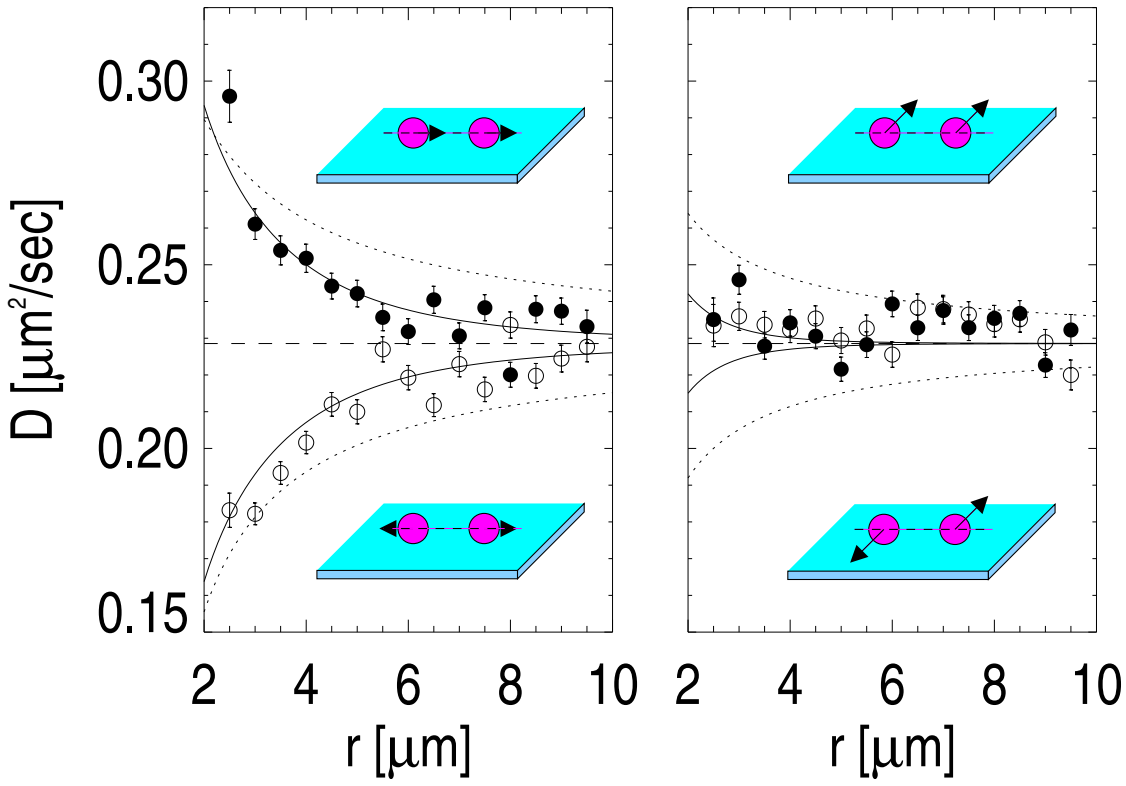

Figure 3.7: *Coupled diffusion two spheres near a wall. Clockwise from top left* $D^{\rho}_{\parallel}$, $D^{\rho}_{\perp}$, $D^{R}_{\parallel}$, $D^{R}_{\perp}$. Solid lines are Stokeslet analysis predictions. Dotted lines are predictions based on the linear superposition of drag forces, using Batchelor and Faxen's high-order expansions and Eq. 3.49.

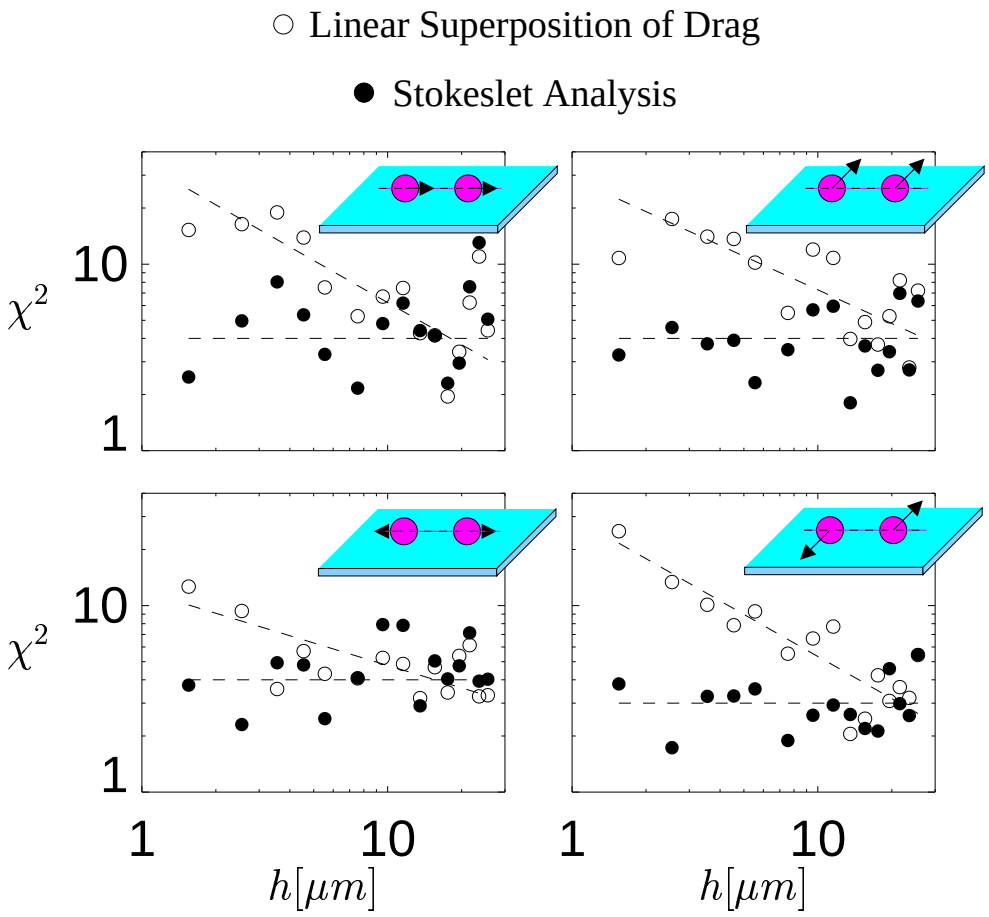

Figure 3.8: *Comparing Stokeslet analysis and the linear superposition of hydrodynamic drag.* χ^2 deviation of the four diffusion coefficients as a function of height above the wall. The open circles are for the linear superposition of drag, and the filled circles are for Stokeslet analysis. The dashed lines are guides to the eye to indicate trends in the data.

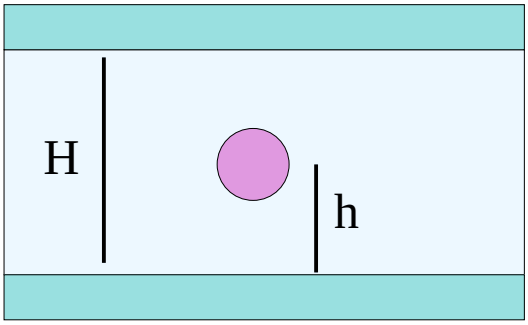

Figure 3.9: *A sphere between two walls.*

pling with the wall is appreciable, while the Stokeslet approach fits the data reasonably well over the full range of data. Therefore many-body contributions to the hydrodynamic interactions of colloidal spheres cannot be ignored when the spheres are near a planar no-slip boundary. These many-body interactions are the source of Squires' hydrodynamically induced like-charged attractions, [75], and may account for some of the complex hydrodynamic behaviors described in the introduction to this chapter. With a view toward describing many-body interactions in suspensions confined between two walls, we now consider the hydrodynamics of a single sphere between two walls.

3.6 Brownian Motion of One Sphere between Two Walls

We now consider the Brownian motion of a single sphere between two parallel planes, separated by a distance H, Fig. 3.9. The description of this deceptively simple system has proven vexing for all but the most symmetric placements of the sphere between the walls. Indeed, recent efforts to extend the available solutions to less symmetric arrangements have led to demonstrably inaccurate results [87]. The simple linear superposition of drag forces performs surprisingly well, particularly

in light of its poor performance in the previous section. The Stokeslet solution to this problem is exceedingly complex, but its results can be readily scaled up to multi-sphere systems.

Faxen obtained asymptotic expressions for the mobility for three highly symmetric locations between parallel walls, $h = H/4,\ H/2,\ 3H/4$ [76]:

$$D_{\|}(h) = \begin{cases} 1 - 0.6526\,\frac{a}{h} + 0.1475\,\frac{a^3}{h^3} \\ \qquad -0.131\,\frac{a^4}{h^4} - 0.0644\,\frac{a^5}{h^5}, & h = \frac{H}{4},\ \frac{3H}{4}. \\ 1 - 1.004\,\frac{a}{h} + 0.418\,\frac{a^3}{h^3} \\ \qquad +0.21\,\frac{a^4}{h^4} - 0.169\,\frac{a^5}{h^5}, & h = \frac{H}{2}. \end{cases} \tag{3.56}$$

These predictions satisfy the no-slip boundary condition on the surfaces of the sphere and both walls, and are plotted as triangles in Fig. 3.10 for various wall separations, H.

Oseen [76, 88] applied the linear superposition of drag forces to this system [89], approximating the total drag on the sphere by the sum of its self drag and the separate contributions of each wall,

$$\gamma(h) = \gamma_o + [\gamma_F(h) - \gamma_o] + [\gamma_F(H-h) - \gamma_o], \tag{3.57}$$

where $\gamma_F(h)$ is the drag on a sphere a height h above a single wall in a semi-infinite system. Applying the Stokes-Einstein relation to this result, we obtain

$$D^{-1}(h) = D_F^{-1}(h) + D_F^{-1}(H-h) - D_o^{-1}, \tag{3.58}$$

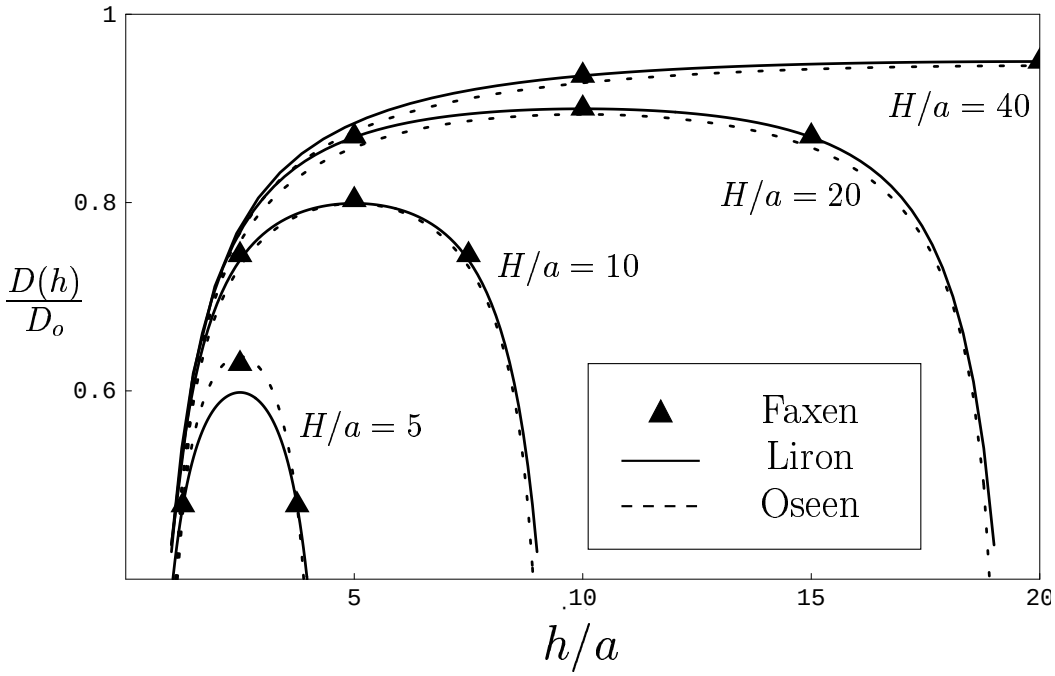

Figure 3.10: *Theoretical predictions for $D_{\|}(h)$ between two parallel walls.*

where $D_F^{-1}(h)$ is Faxen's result for one wall, Eq. 3.47. The resulting predictions for $D_{\|}(h)$ are plotted as dashed lines in Fig. 3.10. Faucheux and Libchaber measured the diffusivities of several particles confined between two glass plates using digital video microscopy [89]. Averaging the diffusivities over h, they found good agreement with Oseen's approximation.

The Stokeslet analysis of this system is considerably more complex. Following Blake's method of hydrodynamic images, Liron and Mochon [90] calculated the Green's function for a point force between parallel planes. They found the total flow-field, u, to be the sum of three parts, $u = G^S + v + w$, where G^S is the free-space Stokeslet, v consists of an infinite series of Stokeslet images, and w is an additional term necessary to match the no slip boundary conditions on the surface each wall. Unfortunately, w has no clear interpretation in terms of hydrodynamic

images. We can use this result to evaluate the walls' influence on the sphere's mobility. Referring once again to Eqs. 3.27 and 3.28, we approximate the external contribution to the mobility, $b^e(h)$, by the fluid velocity at the sphere's position due to all contributions to the flow-field aside from the original Stokeslet, $u - G^S$.

For in-plane diffusion,

$$\frac{D_{\|}(h)}{D_0} = 1 - \frac{3}{4}\frac{a}{H}\int_0^\infty \left[1 + A_0\left(\lambda, \frac{h}{H}\right) + \lambda^2 A_1\left(\lambda, \frac{h}{H}\right)\right] d\lambda, \tag{3.59}$$

where

$$A_0(\lambda, \eta) = \frac{-2\,\sinh[\lambda\eta]\,\sinh[\lambda(1-\eta)]}{\sinh[\lambda]} \tag{3.60}$$

is the contribution due to a stokeslet at the sphere's position together with an infinite series of image stokeslets, and

$$\begin{aligned} A_1(\lambda, \eta) = \frac{1}{\sinh^2[\lambda] - \lambda^2}\Bigg\{ & \lambda\eta^2 \sinh^2[\lambda(1-\eta)] - \sinh[2\lambda\eta] + \\ & \eta^2 \sinh[\lambda]\cosh[\lambda(1-2\eta)] + \coth[\lambda]\sinh^2[\lambda\eta] + \\ & - \frac{\lambda}{4}\left(\frac{(2-\eta)\sinh[\lambda\eta] - \eta\sinh[\lambda(2-\eta)]}{\sinh[\lambda]}\right)^2\Bigg\} \end{aligned} \tag{3.61}$$

enforces the no-flow boundary conditions at the walls. These Stokeslet predictions for $D_{\|}(h)$ are plotted as solid lines in Fig. 3.10.

Even though they only predict the diffusion coefficient at three heights, Faxen's predictions are the most reliable, since they satisfy the boundary conditions on both walls to fifth order in a/h. Liron and Mochon's analysis satisfies the boundary conditions on each wall to first order in a/h. Oseen's theory ignores the boundary

conditions on both walls, and considers the effect of each wall separately to fifth order in a/h. When the walls are separated by more than about 8 radii, these three theories yield nearly identical results, as can be seen in Fig. 3.10. In this range, the theories of Liron and Faxen agree, while Oseen's linear superposition of drag forces slightly underestimates the mobility. For wall separations of less than 8 radii, Oseen and Faxen's theories agree well, while the Stokeslet analysis underestimates the mobility. This comparison suggests Oseen's simple theory is capable of describing the Brownian motion of a single sphere over a wide range of H values. While Liron's analysis is much more cumbersome and applicable over a smaller range of H values, it can be readily extended to describe the coupled diffusion of many spheres, as described in the previous section.

We have measured the in plane diffusion of a two-micron diameter polystyrene sphere ($a = (1.006 \pm 0.010)\,\mu m$, Duke Scientific, Cat. No. 4202A) between two glass walls [86]. The experimental technique was nearly identical to that described in Section 3.4. The walls were separated by roughly $8\,\mu m$ and the temperature of the system was controlled at $T = (27.50 \pm 0.07)^{\circ}C$. A small difference in height between colloid reservoirs connected to either side of the sample cell drove a very slow flow through the system. Measuring the profile of this flow, we were able to locate the positions of the walls. To characterize this flow, we assume that the sphere tracks the flow of the fluid and measure the drift velocity of the sphere along the x and y directions as a function of height above the wall, Fig. 3.11. This flow profile is well described by a Poiseuille flow [91],

$$v(z) = -\frac{4v_o}{H^2}\,(z - z_o)(z - z_o - H), \tag{3.62}$$

where $z = h + z_o$, and z_o is the absolute position of the lower wall. A fit to Eq. 3.62 gives $z_o = (-1.04 \pm 0.11)\,\mu m$, and the separation of the walls, $H = (8.16 \pm 0.22)\,\mu m$. The measured values of $D_{||}(h)$ are shown in Fig. 3.12. The data are consistent with all three theoretical formulations near the center of the cell, but the predictions underestimate the diffusion coefficient when the sphere is near contact. This may be the result of the coupling between the rotational motion of the sphere and its in plane diffusion. Coupling between translational and rotational diffusion is not accounted for in any of the three theories discussed above. Additionally, the Poiseuille flow rotates the sphere. This rotation of the sphere is described by Faxen's second law, [21], and is strongest near the walls where the fluid is most strongly sheared.

3.7 Extending Stokeslet Analysis to Many-Body Systems

Stokeslet analysis simply and successfully describes the hydrodynamic coupling of spheres in a unbounded fluid and near one bounding wall. Measurements of the coupling of two spheres near a single wall suggest that Stokeslet analysis correctly accounts for wall-induced many-body interactions. Stokeslet analysis is cumbersome between two walls, and is only applicable when the walls are separated by more than about 8 sphere radii. Even so, Stokeslet analysis can be systematically extended to describe many-body coupling in larger confined systems.

In a recent paper [70], Brenner performs a Stokeslet analysis of large numbers of sedimenting spheres near a wall. He shows that wall-induced many-body interactions suppress the theoretically predicted [68] but experimentally illusive [69] divergence of sedimentation velocity fluctuations. While the results of sedimentation experiments are consistent with Brenner's Stokeslet analysis, they do not directly test its general validity.

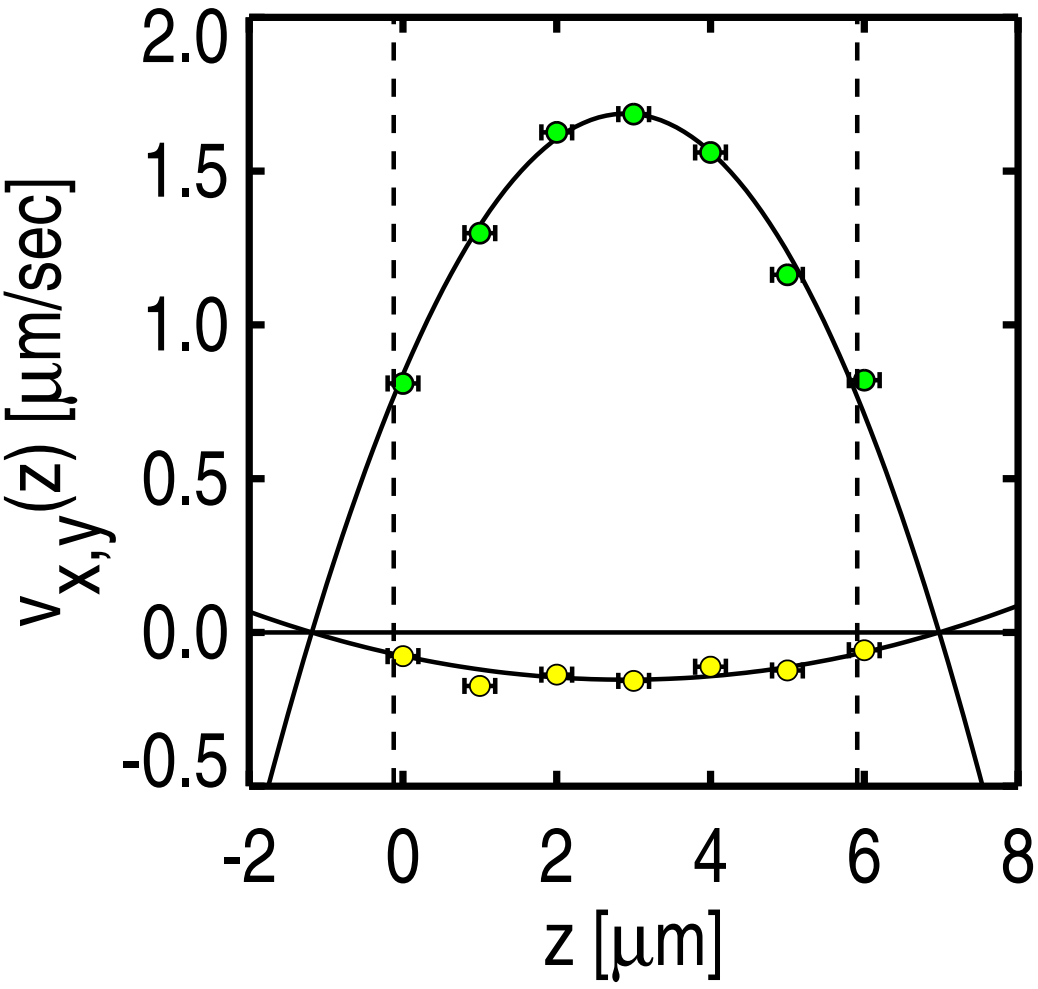

Figure 3.11: *Poiseuille Flow.* The positive flow profile is along the x direction and the negative flow is along the y direction. Vertical lines indicate contact between the sphere and each wall.

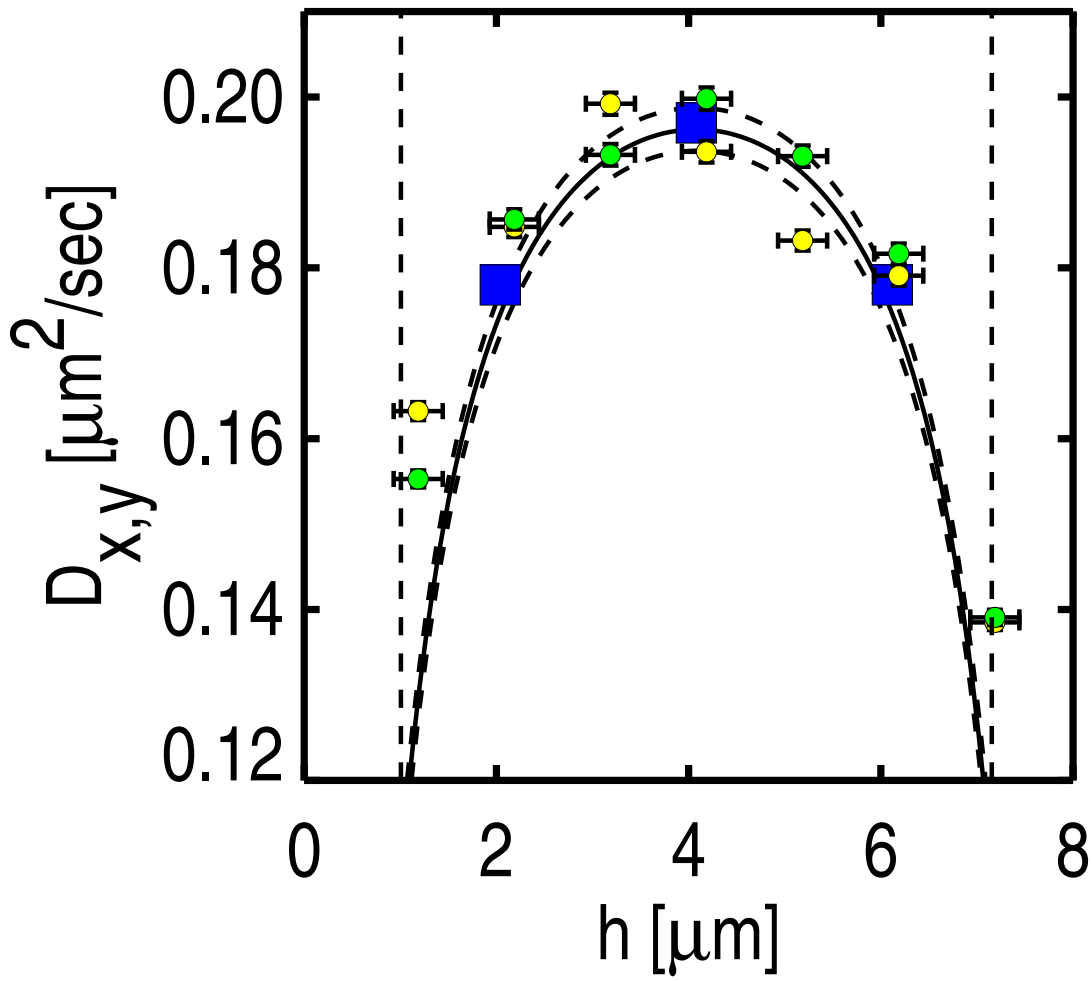

Figure 3.12: *Measured values of* $D_{||}(h)$ *between two parallel walls.* The squares represent Faxen's predictions. The solid and dashed lines plot Oseen's prediction for $a = 1.006\,\mu m$ and $a = (1.006 \pm 0.010)\,\mu m$, respectively. The measured diffusion coefficients along x and y are separately plotted as circles at each height.

Blinking optical tweezer experiments with many optical tweezers could precisely test Stokeslet predictions of many-body effects for larger systems. However, conventional techniques cannot create more than a few tweezers. Therefore, we have developed a novel technique to trap large numbers of colloidal particles in arbitrary configurations. This technique, combining optical tweezers and holography, is discussed in the next chapter.

CHAPTER 4

MASS MICROMANIPULATION OF COLLOIDAL PARTICLES WITH HOLOGRAPHIC OPTICAL TWEEZER ARRAYS

The optical tweezer has become a valuable tool for research in biological [40–45] and physical [23, 31, 35–39] sciences. Past applications of optical tweezers to colloid science have concentrated on the dynamics of one or two particles, since no simple, robust and inexpensive technology had been available to create more than two optical tweezers. Large arrays of optical tweezers could be used to study collective behavior in systems with many particles, to organize microscopic particles into complex structures, to gently and securely grab delicate objects that cannot be trapped with a single tweezer, and to intelligently sort microscopic particles. We apply holographic techniques to create large arrays of optical tweezers from a single laser beam. These *holographic optical tweezer arrays* are capable of trapping hundreds of particles simultaneously, [32, 92, 93]. Other schemes to create multiple optical tweezers were described in Section 2.2.

In principle, N optical tweezers can be made by separately focusing N laser beams with a microscope objective lens, as shown in Fig. 4.1(a). In practice, this technique becomes prohibitively cumbersome and expensive when N is much larger than two. Alternatively, a *hologram* can modulate the wavefront of a single laser beam to mimic the interference pattern of N beams converging at the entrance to

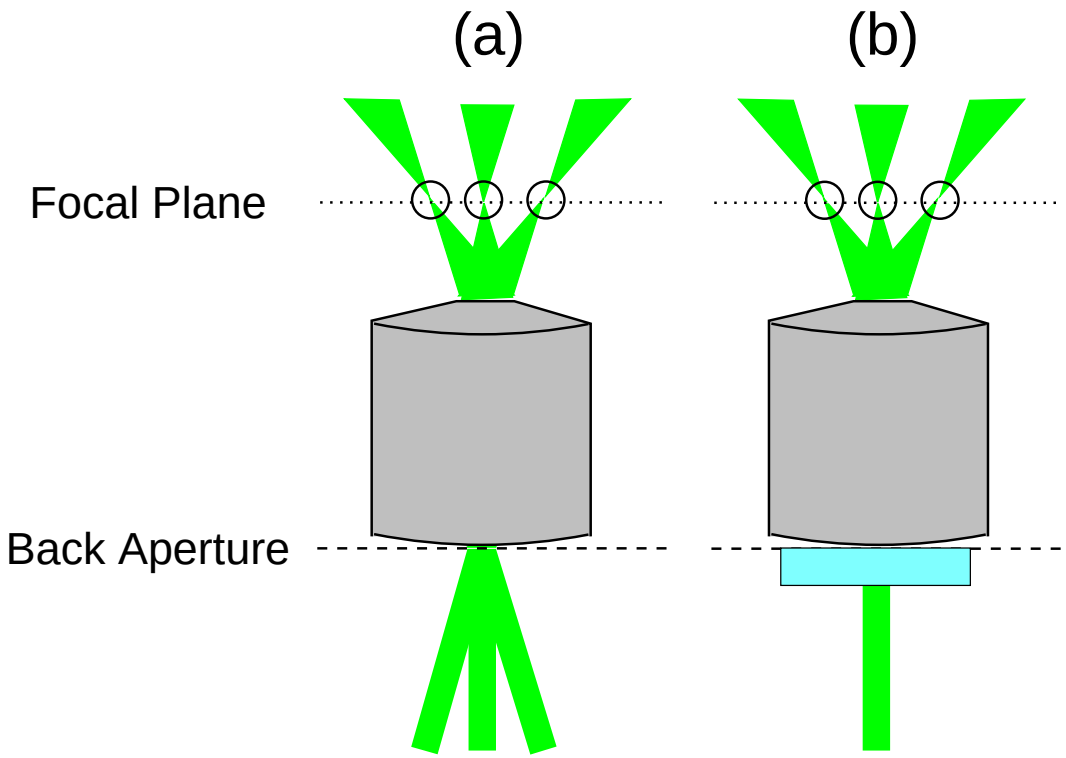

Figure 4.1: *Holographic optical tweezer arrays. (a)* N laser beams are focused by an objective lens to create N optical tweezers. *(b)* A holograms sculpts the wavefront of a single laser beam to mimic the wavefront of N beams converging on the back aperture of the microscope objective, creating N optical tweezers in the focal plane.

the objective lens, Fig. 4.1(b). After passing through the hologram, this sculpted wavefront propagates as N separate beams, forming N optical tweezers in the objective lens' focal plane. In order to mimic the wavefront of N converging beams, a hologram must spatially modulate both the amplitude and phase of the incident beam. However, a hologram cannot modulate a laser beam's amplitude without absorbing some of its energy. Not only is this is inefficient, but it will also damage the hologram at the high laser intensities needed to make large numbers of optical tweezers. Fortunately, optical trapping relies on the optical field's intensity rather than its amplitude and phase separately. Consequently, it is possible to achieve any desired trapping pattern by modulating only the phase of the incident beam.

In this chapter, we describe the design, fabrication, and implementation of efficient phase-only holograms. Before describing the process in detail, however, we first develop the necessary theory of Fourier Optics.

4.1 Fourier Optics of Tweezer Arrays

An array of optical tweezers can be described by the intensity distribution of laser light in the focal plane of a microscope objective lens, $I^f(\vec{\rho})$. The intensity distribution in the focal plane of a lens is determined by the profile of the electric field of light incident at its input plane. While there is a one-to-one correspondence between the electric fields in the input and focal planes of a lens, an infinite number of incident electric fields can yield the same intensity profile in the focal plane, $I^f(\vec{\rho})$, since intensity is independent of the phase of the electric field. Before describing how to exploit this redundancy to create phase-only holograms, We develop the optical principles relating the electric fields in the input and focal planes of a lens.

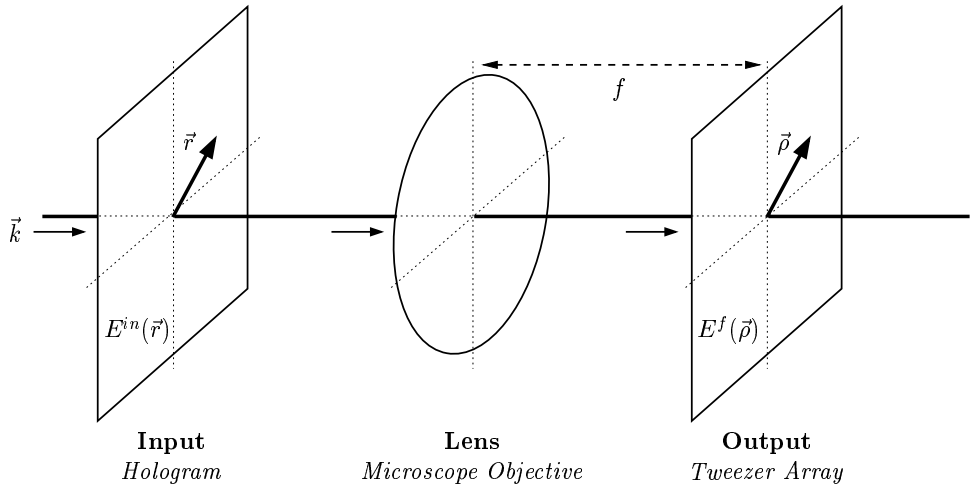

Figure 4.2: *Fourier optics.* Monochromatic light, with wavevector $\vec{k}$, is incident on the input plane. A lens, of focal length f, projects the Fourier transform of the electric field profile, $E^{in}(\vec{r})$, of the incident light onto the focal plane.

Suppose that the input plane of an objective lens is illuminated by linearly polarized monochromatic light, Fig. 4.2. Then the electric field at the input plane is described by

$$\vec{E}^{in}(\vec{r}, t) = E^{in}(\vec{r})e^{i\omega t}\hat{e}, \tag{4.1}$$

where ω is the frequency of the incident light and $\hat{e}$ is its polarization vector. The electric field profile, $E^{in}(\vec{r})$, contains both phase and amplitude information,

$$E^{in}(\vec{r}) = A^{in}(\vec{r}) \exp[i\Phi^{in}(\vec{r})], \tag{4.2}$$

where the amplitude, $A^{in}(\vec{r})$, and phase, $\Phi^{in}(\vec{r})$, are real-valued functions. Similarly,

the electric field in the focal plane of the microscope objective is given by,

$$\vec{E}^f(\vec{\rho},t) = E^f(\vec{\rho})e^{i\omega t}\hat{e}, \tag{4.3}$$

and

$$E^f(\vec{\rho}) = A^f(\vec{\rho})\exp[i\Phi^f(\vec{\rho})]. \tag{4.4}$$

Therefore, the intensity profile of a tweezer array,

$$I^f(\vec{\rho},t) \propto \vec{E}^f(\vec{\rho},t)\cdot\vec{E}^f(\vec{\rho},t)^* = A^f(\vec{\rho})^2, \tag{4.5}$$

is independent of time and the phase of the electric field profile in the focal plane.

The electric field profiles in the input and focal planes of a lens are related by a Fourier transformation, $\mathcal{F}$,

$$E^f(\vec{\rho}) = \mathcal{F}\{E^{in}(\vec{r})\} \equiv \frac{k}{2\pi f}\, e^{i\theta(\vec{\rho})}\int d^2\vec{r}\, E^{in}(\vec{r})\, e^{-ik\vec{r}\cdot\vec{\rho}/f}, \tag{4.6}$$

$$E^{in}(\vec{r}) = \mathcal{F}^{-1}\{E^f(\vec{\rho})\} \equiv \frac{k}{2\pi f}\int d^2\vec{\rho}\, e^{-i\theta(\vec{\rho})}E^f(\vec{\rho})\, e^{ik\vec{r}\cdot\vec{\rho}/f}, \tag{4.7}$$

where f is the focal length of the lens and k is the wavenumber of incident light. The lens' geometry introduces the additional phase profile, $\theta(\vec{\rho})$, which does not influence the intensity in the focal plane, and may be ignored without loss of generality [94].

As an example, let us apply Eq. 4.6 to the formation of a single optical tweezer. Typically, an optical tweezer is created by focusing a Gaussian laser beam with a microscope objective lens. Laser beams with other profiles may be used to increase the tweezer's efficiency, or to trap particles that cannot be trapped in a conventional

tweezer [49, 55, 95]. For a Gaussian beam, the intensity profile of the tweezing laser in the input plane of the objective lens is

$$I_G^{in}(\vec{r}) = \frac{P}{2\pi\,\sigma_{in}^2} \exp\left[\frac{-r^2}{2\,\sigma_{in}^2}\right], \tag{4.8}$$

where P is the beam's power, and σ_{in} is its radius. The phase of a collimated Gaussian beam is uniform in the plane normal to its wavevector, $\vec{k}$. Therefore, the incident electric field profile may be written as

$$E_G^{in}(\vec{r}) = A_G^{in}(\vec{r}) = \sqrt{I_G^{in}(\vec{r})}. \tag{4.9}$$

Applying Eq. 4.6 to $E_G^{in}(\vec{r})$ gives the electric field and intensity of an optical tweezer in the focal plane of the objective lens,

$$I_G^{f}(\vec{\rho}) = \frac{P}{2\pi\,\sigma_{f}^2} \exp\left[\frac{-\rho^2}{2\,\sigma_{f}^2}\right], \tag{4.10}$$

where

$$\sigma_f = \frac{f}{2k\,\sigma_{in}}. \tag{4.11}$$

The optical gradient forces responsible for trapping are strongest when the width of the tweezer is minimized. Therefore, a tweezer is strongest when the width of the incident beam is maximized. The width of the incident beam is limited by the input aperture of the objective lens, which is equal to the product of its focal length

and numerical aperture, NA. Since the minimum width of a tweezer is

$$\sigma_f = \frac{1}{2k\,NA}, \tag{4.12}$$

a tweezer is strongest when the objective lens has a high numerical aperture and the trapping laser has a short wavelength.

This analysis can be generalized to understand how phase modulation can create arrays of optical tweezers from a single laser beam. After passing through a phase modulating hologram, the electric field profile in the input plane of an objective lens is

$$E^{in}(\vec{r}) = E_0^{in}(\vec{r})\exp[i\Phi^{in}(\vec{r})], \tag{4.13}$$

where $E_0^{in}(\vec{r})$ is the electric field profile of the incident beam, and $\Phi^{in}(\vec{r})$ is the modulated phase profile.

The electric field describing an array of identical optical tweezers at the positions $\vec{\rho}_\alpha$ in the focal plane of the objective lens is

$$E^f(\vec{\rho}) = \left[\sum_\alpha E_0^f(\vec{\rho} - \vec{\rho}_\alpha)\right]\exp[i\Phi^f(\vec{\rho})], \tag{4.14}$$

where $E_0^f(\vec{\rho})$ is the electric field profile of a single tweezer. The phase profile, $\Phi^f(\vec{\rho})$, may take any real value without affecting the performance of the tweezer array. Alternatively, $E^f(\vec{\rho})$ may be written as the convolution of $E_0^f(\vec{\rho})$ and a lattice function, $T(\vec{\rho})$, describing the geometry of the array,

$$E^f(\vec{\rho}) = [E_0^f \circ T(\vec{\rho})]\exp[i\Phi^f(\vec{\rho})], \tag{4.15}$$

where

$$T(\vec{\rho}) = \sum_{\alpha} \delta^2(\vec{\rho} - \vec{\rho}_\alpha) \tag{4.16}$$

and $f \circ g(x)$ denotes the convolution of f and g,

$$f \circ g(\vec{x}) \equiv \int d^2\vec{x}' f(\vec{x}') g(\vec{x} - \vec{x}'). \tag{4.17}$$

We can relate the electric field in the input and focal planes of the lens using Eq. 4.6 :

$$\mathcal{F}\{E_0^{in}(\vec{r}) \exp[i\Phi^{in}(\vec{r})]\} = [E_0^f(\vec{\rho}) \circ T(\vec{\rho})] \exp[i\Phi^f(\vec{\rho})]. \tag{4.18}$$

This expression can be understood in light of the frequency-convolution theorem [96], which states that the Fourier transform of the product of two functions is equal to the convolution of their individual transforms,

$$\mathcal{F}\{fg\} = \frac{k}{2\pi f} \mathcal{F}\{f\} \circ \mathcal{F}\{g\}. \tag{4.19}$$

Comparing Eqs. 4.18 and 4.19, we see that the electric field profile of each tweezer is given by the Fourier transform of the unmodified incident beam, $E_0^f(\vec{\rho}) = \mathcal{F}\{E_0^{in}(\vec{\rho})\}$, and the configuration of the tweezers is determined by the Fourier transform of the phase modulation,

$$\frac{2\pi f}{k} T(\vec{\rho}) \exp[i\Phi^f(\vec{\rho})] = \mathcal{F}\{\exp[i\Phi^{in}(\vec{r})]\}. \tag{4.20}$$

Therefore, a hologram controls the geometry of the array without affecting the properties of each tweezer. For example, a hologram that produces an array of Gaussian tweezers, can also produce an array of optical vortex tweezers.

As a simple example, let us calculate the phase modulation, $\Phi^{in}(\vec{r})$ that displaces the focal point of a single optical tweezer by a vector, $\Delta\vec{\rho}$. The displaced tweezer is described by the lattice function

$$T(\vec{\rho}) = \delta^2(\vec{\rho} - \Delta\vec{\rho}). \tag{4.21}$$

Arbitrarily setting $\Phi^f(\vec{\rho}) = 0$ and inverting Eq. 4.20, we find

$$\exp[i\Phi^{in}(\vec{r})] = \mathcal{F}^{-1}\Big\{\frac{2\pi f}{k}\, T(\vec{\rho})\Big\} = \exp[ik\vec{r}\cdot\Delta\vec{\rho}/f]. \tag{4.22}$$

Therefore, one can displace an optical tweezer by applying a linear phase modulation,

$$\Phi^{in}(\vec{r}) = \frac{k\,\Delta\vec{\rho}\cdot\vec{r}}{f}, \tag{4.23}$$

to the laser as it enters the objective lens, where the size of the displacement of the tweezer is proportional to the slope of the phase in the input plane. Instead of modulating the phase with a hologram, it is usually easier to apply this phase gradient and steer the tweezer by tilting the beam through an angle, $\Delta\rho/f$, as it enters the objective lens, as in Section 2.2.

4.2 Designing Holograms for Optical Tweezer Arrays Using the Adaptive-Additive Algorithm

In general, designing phase modulating holograms that produce arrays of optical tweezers is not as simple as inverting Eq. 4.20 with $\Phi^f(\vec{\rho}) = 0$, because the inverse Fourier transform of the lattice function, $T(\vec{\rho})$, contains both amplitude and phase information. This section describes the adaptive-additive (AA) algorithm of Soifer *et al.* [97], an iterative numerical technique which explores the space of degenerate phase profiles, $\Phi^f(\vec{\rho})$, to find a phase modulation of the incident laser beam that creates the desired intensity profile in the focal plane of the microscope objective lens.

The AA algorithm, Fig. 4.3, calculates the phase modulation, $\Phi^{in}(\vec{r})$, of a hologram that most nearly reproduces a desired intensity pattern in the focal plane, $I_0^f(\vec{\rho}) = |A_0^f(\vec{\rho})|^2$, from an input beam whose profile is $A_0^{in}(\vec{r})$. Starting from an initial guess for the hologram's phase profile, $\Phi_0^{in}(\vec{r})$, the AA algorithm iteratively calculates the input phase profile, $\Phi^{in}(\vec{r})$, that most accurately reproduces the desired intensity pattern in the focal plane of a lens. Specifically, AA algorithm minimizes the mean-squared deviation of the actual intensity profile, $I^f(\vec{\rho})$, from the ideal intensity pattern,

$$\epsilon \equiv \frac{1}{M^2} \sum_{i=1}^{M^2} (I^f(\vec{\rho}_i) - I_0^f(\vec{\rho}_i))^2, \tag{4.24}$$

where the focal plane of the microscope objective has been discretized on a $M \times M$ square lattice.

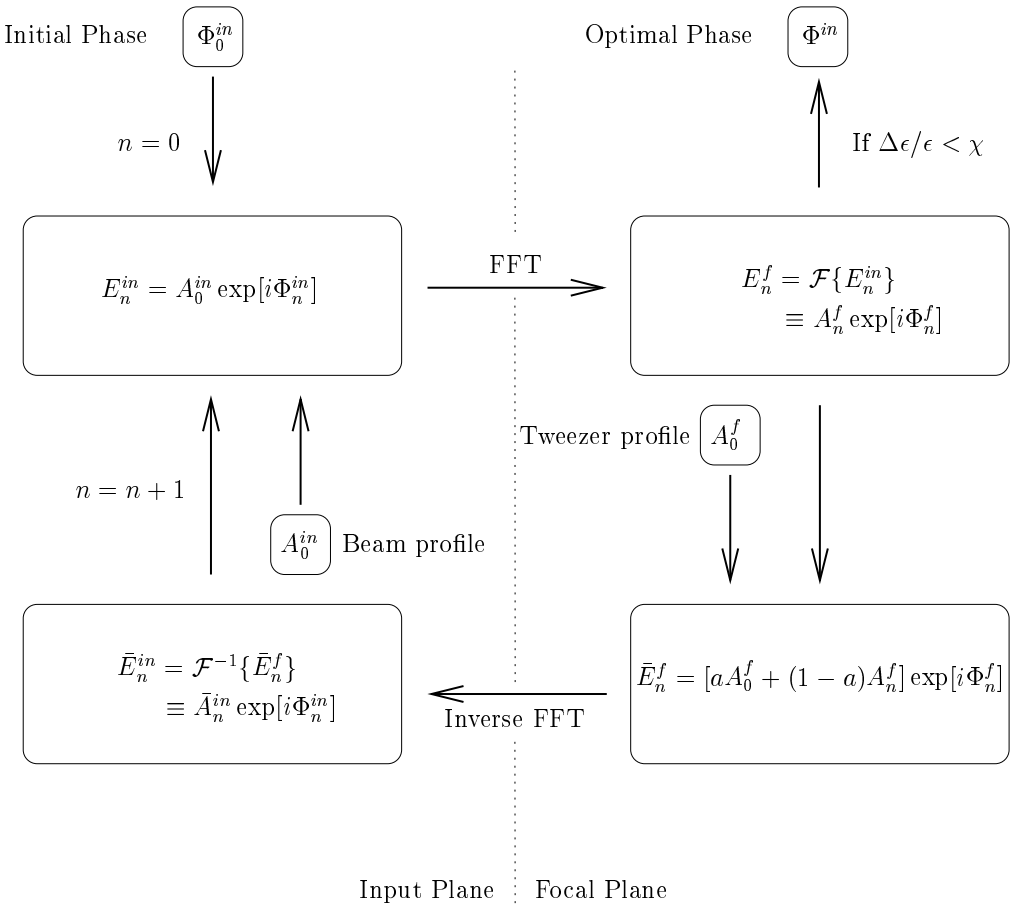

Figure 4.3: *Adaptive-additive algorithm.*

The AA algorithm starts by calculating the electric field profile in the input plane. For the first iteration, $E_0^{in}(\vec{r}) = A_0^{in}(\vec{r})\exp[i\Phi_0^{in}(\vec{r})]$. For later iterations, $E_n^{in}(\vec{r})$ is determined by the output of the previous iteration. The AA algorithm applies a fast Fourier transformation (FFT) to calculate the corresponding electric field profile in the focal plane, $E_n^f(\vec{\rho}) = A_n^f(\vec{\rho})\exp[i\Phi_n^f(\vec{\rho})]$. Next, the algorithm replaces $A_n^f(\vec{\rho})$ with a mixture of $A_n^f(\vec{\rho})$ and the electric field profile of the desired tweezer pattern, $A_0^f(\vec{\rho})$,

$$\bar{E}_n^f(\vec{\rho}) = [aA_o^f(\rho) + (1-a)A_n^f]\exp[i\Phi_n^f(\vec{\rho})], \tag{4.25}$$

where the mixing parameter, a, lies between 0 and 1. The algorithm then transforms the modified electric field profile, $\bar{E}_n^f(\vec{\rho})$, back to the input plane to give $\bar{E}_n^{in}(\vec{r})$. At this point, the amplitude profile, $\bar{A}_n^{in}$, no longer matches the actual laser profile, so the algorithm replaces $\bar{A}_n^{in}$ with $A_0^{in}(\vec{r})$, and increments the counter, n, by one. This completes a full iteration of the AA algorithm. The cycle is repeated until the error, ϵ, converges to a minimal value. The algorithm is said to have converged when the relative change in the error parameter is less than some set value χ: $\Delta\epsilon/\epsilon < \chi$.

For all but the simplest intensity patterns, the algorithm converges to phase profiles that do not exactly reproduce the desired output, $\epsilon = 0$. Instead, it typically converges to one of many local minima of ϵ, all of which produce outputs of similar quality. The absolute quality of the reproduction depends on the complexity of the desired intensity pattern. In particular, the algorithm is more successful at reproducing patterns of isolated bright points, such as those that make tweezer arrays, than it is for smooth patterns.

The AA algorithm is readily adapted to calculate holograms for optical tweezer arrays. For arrays of identical optical tweezers, we ignore the profile of the input beam, using $A_0^{in}(\vec{r}) = 1$, and set $A_0^f(\vec{\rho}) = \frac{2\pi f}{k} T(\vec{\rho})$. We discretize the input and focal planes, describing the optical fields as an $M \times M$ array of double precision real numbers. For maximum resolution, we choose the pixel size in the focal plane to be one half-wavelength, $\delta_f = \lambda/2$. The pixel sizes in the input and focal planes are related by Eq. 4.6, $\delta_{in} = \frac{\lambda f}{M \delta_f}$. For our choice of $\delta_f = \lambda/2$, the pixel size of the hologram is $\delta_{in} = 2f/M$. Finally, the AA algorithm requires an initial guess for the phase, $\Phi_0^{in}(\vec{r})$. We assign an evenly distributed random number between 0 and 2π to each of $\Phi_0^{in}(\vec{r})$'s M^2 pixels.

The algorithm converges quite rapidly for intermediate values of the mixing parameter, a, Fig. 4.4. For $a = 0$, the algorithm never moves beyond the initial guess, and for $a = 1$, the algorithm often fails to converge. In all of our calculations, we have used $a = 0.5$ and $\chi = 10^{-6}$. For most patterns, the algorithm converges in about eight iterations. The error, ϵ typically changes by less than one part in 10^{-2} after the second iteration, and by less than one part in 10^{-6} after about eight iterations. While the algorithm typically does not converge to an exact solution for complex trapping patterns, it does rapidly converge to the exact solution for our simple example of a displaced tweezer, Eq. 4.23, Fig. 4.5.

Holograms that produce highly symmetric arrays of tweezers have a periodic structure whose symmetry reflects the symmetries of the tweezer array. Square arrays, Figs. 4.4, 4.6, and 4.12, are produced by holograms with a square periodic lattice. Holograms that generate triangular cluster of tweezers, Fig. 4.14, similarly have local triangular symmetry, but no well defined unit cell.

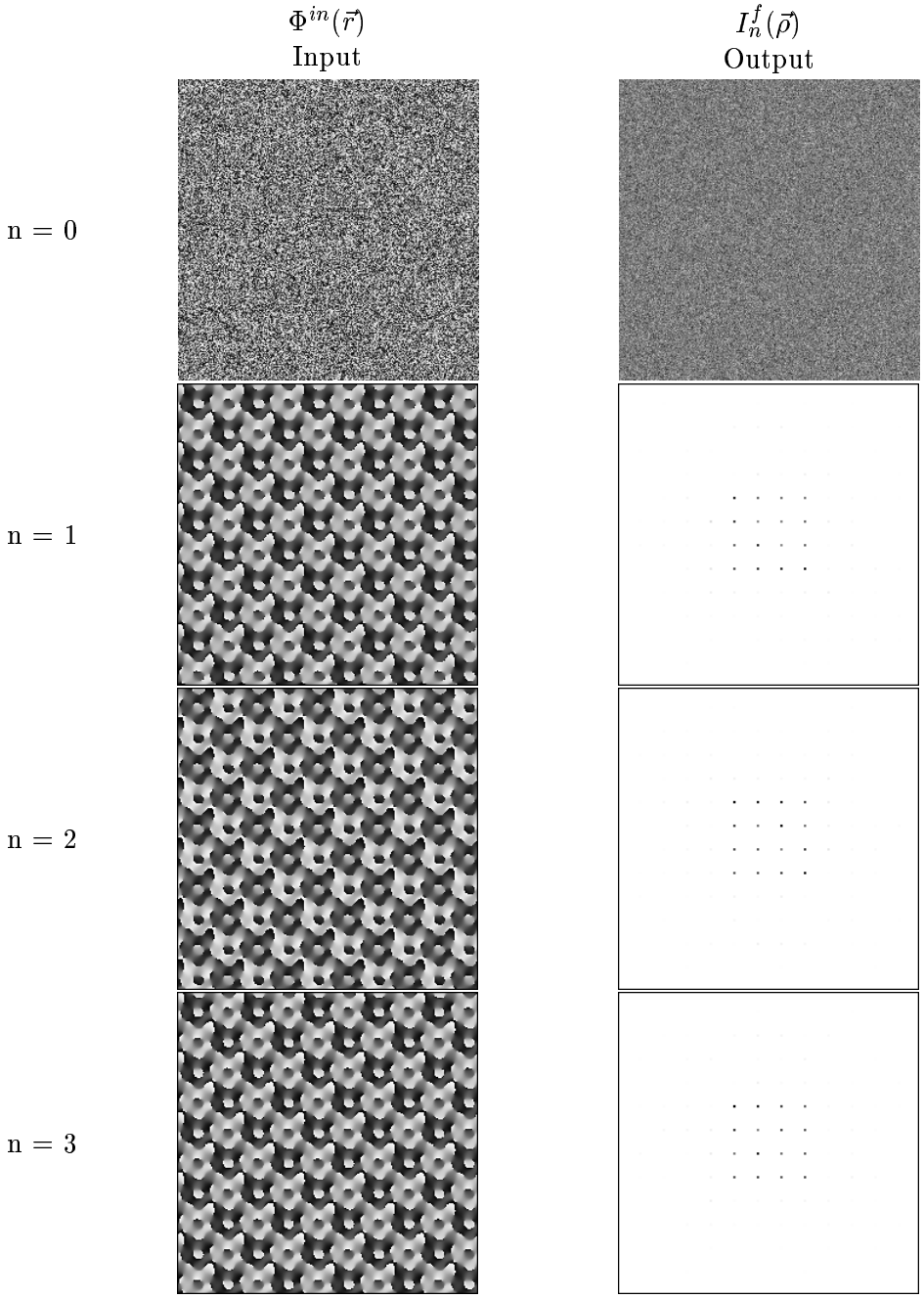

Figure 4.4: *Rapid convergence of the AA algorithm.* The input phase and output intensity profiles after successive iterations of the AA algorithm for a 4×4 square array. The phase profile accurately reconstructs the desired output after a single iteration. The grayscale coloring of the phase profiles encodes phaseshifts from 0 to $2\ \pi$ radians.

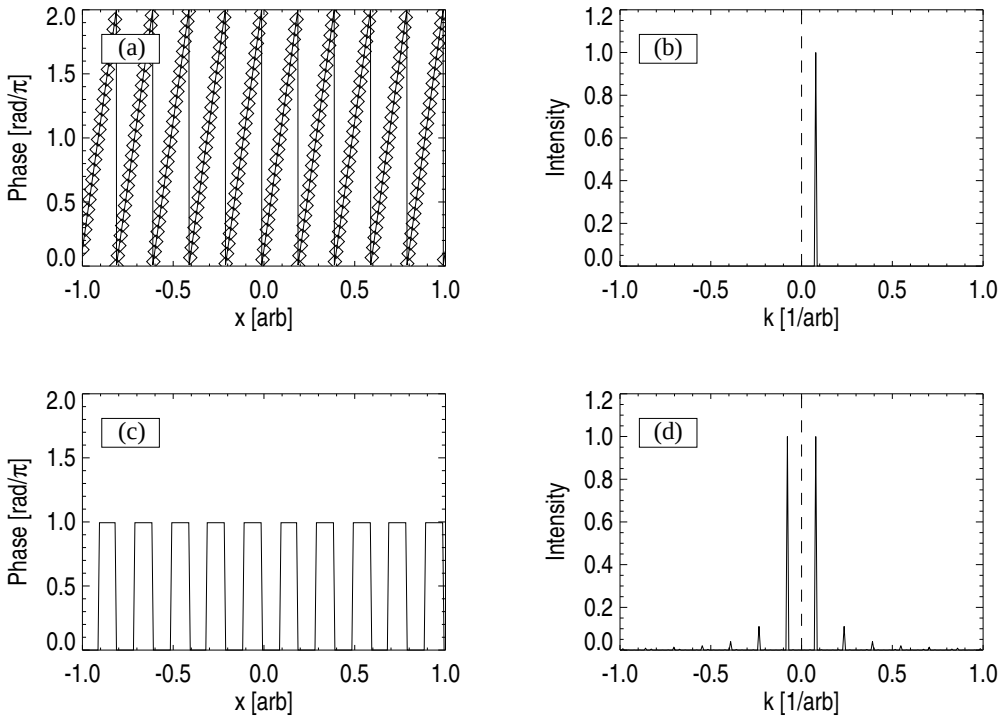

Figure 4.5: *Holographic displacement of* $I^f(\vec{\rho})$. *(a)* A one dimensional phase profile, $\Phi^{in}(\vec{r})$, which displaces the intensity pattern in the focal plane. The solid line plots the exact solution, Eq. 4.23, modulo 2π. The diamonds plot the numerical solution found by the AA algorithm. *(b)* The resulting lattice function, $T(\vec{\rho})$. *(c)* Two-level discretization of $\Phi^{in}(\vec{r})$. *(d)* The resulting lattice function. The original shifted tweezer is reflected across the origin, and small spurious peaks appear.

Computational techniques can exploit the periodicity of holograms in order to increase their efficiency. Because discrete Fourier transformations yield periodic functions, all holograms calculated with the AA algorithm can be tiled smoothly. That is, they can serve as the unit cell for a new hologram with a periodic lattice, and the new hologram will not have phase discontinuities at the unit cell boundaries. Fig. 4.6 shows successive tilings of a hologram that generates the lattice function for a 3×3 square array of tweezers. Successive tilings are labelled by the wavenumber, k, which is equal to both the number of unit cells along one side of the hologram and the lattice constant of the tweezer array in pixels. In other words, tiling changes the length scale of lattice functions but not their geometry.

We have exploited this simple property to design holograms that produce large lattice tweezer arrays. As a tweezer array's lattice constant gets large, the features on the hologram that produce it become smaller. In order to resolve these small features, the hologram's pixel size must be reduced. Since the width of the hologram is fixed, the number of pixels increases with the inverse square of the pixel size. As the holograms contain more pixels, the AA algorithm performs more operations and consumes more memory. Practically, our computer resources do not have enough memory to handle these extra pixels at large lattice constants. Therefore, instead of directly calculating the hologram for a large lattice constant array, we calculate the hologram for a small lattice constant array of the same geometry. Then, this hologram can be tiled to create the hologram that produces large lattice constant tweezer arrays. This tiling can be done either numerically or physically, during the fabrication process. The hologram that produced the 20×20 square array in Fig. 4.15 was tiled during the fabrication process.

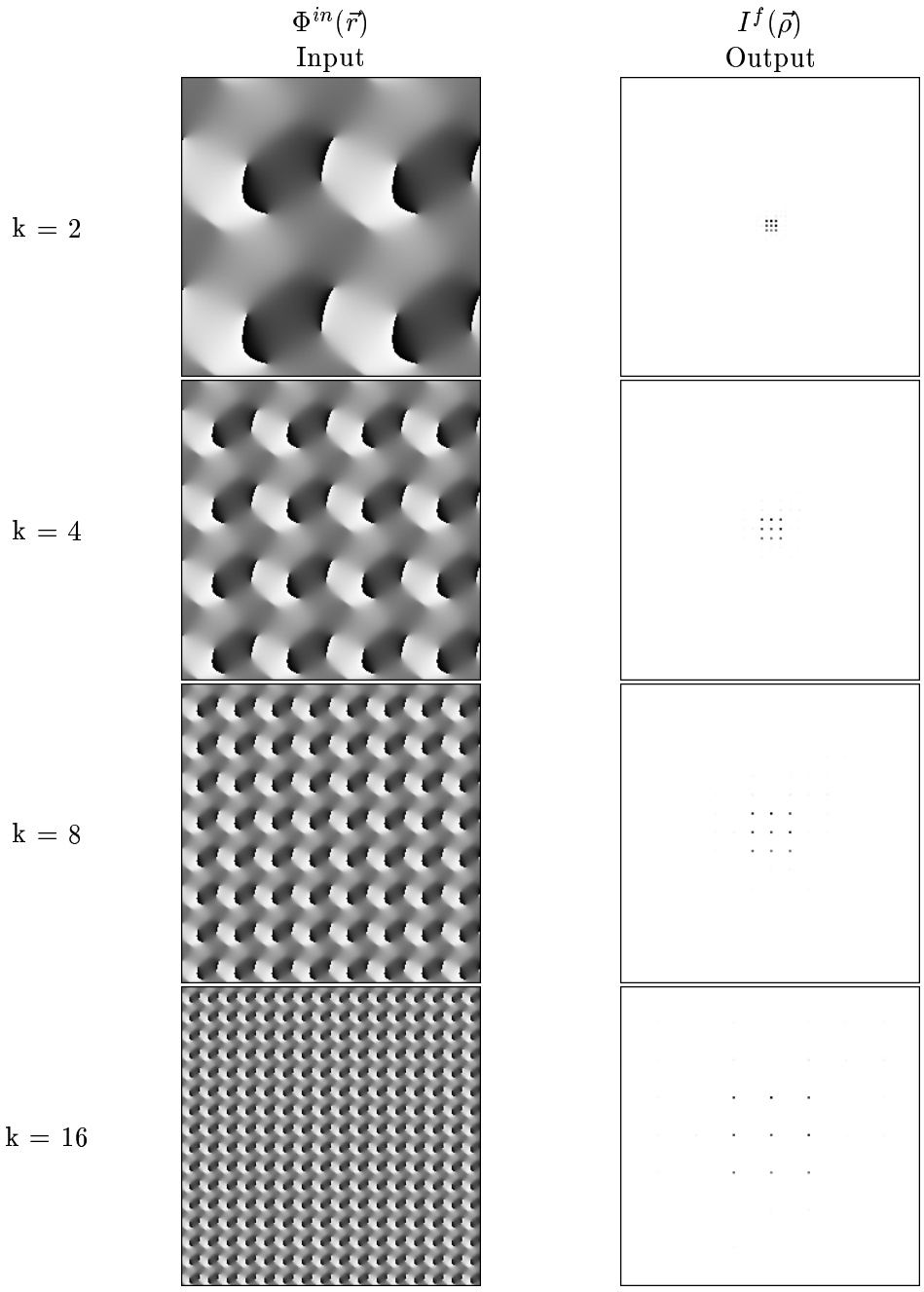

Figure 4.6: *Tiling holograms.* Holograms that generate the lattice function for a 3×3 square array of tweezers. This figure shows the how tiling can be used to increase the lattice constant of a tweezer array.

The AA algorithm generates phase profiles, $\Phi^{in}(\vec{r})$, that vary smoothly between 0 and 2π. However, it is often more convenient to fabricate *binary holograms*, where there are only two phase levels, 0 and π. The holograms in this thesis were made using etching techniques, which are described in the next section. In principle, etching techniques can produce 2^N levels of phase from N precisely aligned etches with different masks [98]. In practice, it is extremely time consuming and difficult to perform more than one etch on a single substrate. Therefore, all of our demonstrations of holographic optical tweezers have used binary holograms. Binary holograms have their limitations, but once these limitations are understood, the AA algorithm can be used to design them.

Binary holograms are less efficient than continuous holograms and are constrained to create tweezer patterns that are inversion symmetric. For example, let us return to our simple example of a hologram that displaces a single tweezer by $\Delta\vec{\rho}$, Eq. 4.23. Discretization replaces the smooth linear increase of phase across the hologram with discontinuous jumps between 0 and π, Fig. 4.5(c). The resulting tweezer array consists of the original shifted tweezer, an equal magnitude reflection across the origin, and some new spurious peaks, Fig. 4.5(d). In general, binary holograms produce tweezer patterns that are unchanged upon reflection through the origin, $\vec{\rho} \longrightarrow -\vec{\rho}$. Our simple example clearly demonstrates the source of this inversion symmetry: after binary discretization, a hologram that shifts a tweezer by $\Delta\vec{\rho}$ is indistinguishable from a hologram shifts the tweezer by $-\Delta\vec{\rho}$, Fig. 4.5(c). Simply stated, the laser light cannot tell if it is supposed to go left or right, so it goes both ways, Fig. 4.5(d).

Let us consider how this inversion symmetry must be accounted for in the calculation of binary holograms. If we simply limit the binary discretization of a smooth

holograms to cases where the pattern of tweezers is inversion symmetric, we still do not get satisfactory tweezer arrays, Figs. 4.7(a) and (b). However, if we anticipate the reflection, and discretize smooth holograms that produce only half of the array, we achieve satisfactory results, as shown in Figs. 4.7(c) and (d). In practice, we repeat this calculation about twenty times and choose the binary hologram with the best value of the error parameter, ϵ, or some other selection criterion, such as efficiency or standard deviation of tweezer intensities.

4.3 Fabricating Holograms for Optical Tweezer Arrays

We have described techniques for calculating the phase profiles, $\Phi^{in}(\vec{r})$, of holograms that modify the profile of a laser beam to create multiple optical tweezers in the focal plane of a microscope objective lens. We now discuss techniques for recording these phase profiles in actual holograms.

Phase profiles can be recorded in the surface topography of a transparent dielectric [98] or in the orientation of liquid crystal domains in a display panel [99]. We have chosen the former approach, shown in Fig. 4.8. The dielectric material slows the propagation of an electromagnetic wave. When a wavefront first enters the material, it is uniformly slowed down to a velocity c/n, where n is the material's index of refraction. However, different parts of the wavefront emerge from the material before others. The sections of the wavefront that remain in the material fall behind the free sections of the wavefront, which travel at the speed of light, c. The end result is that there is a relative phase shift between different parts of the wavefront. The phase at a position, $\vec{r}$, is retarded in proportion to the thickness of the dielectric, t, at that point, $\Phi^{in}(\vec{r}) = -2\pi(n-1)t(\vec{r})/\lambda$. In practice, the

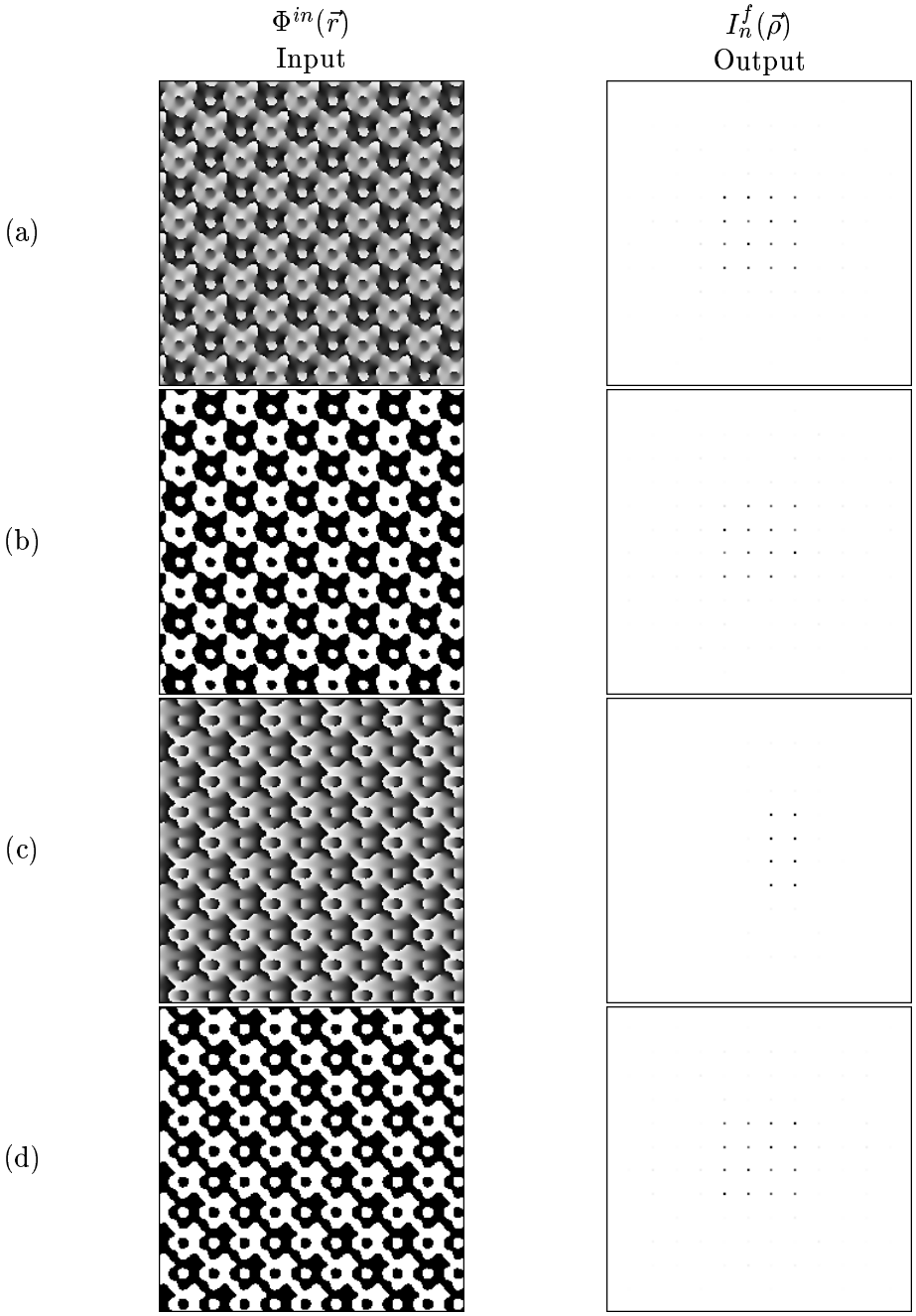

Figure 4.7: *Dealing with the inversion symmetry of binary holograms. (a)* A smooth hologram that makes 4×4 array of tweezers. *(b)* The binary version of hologram (a) generates an array with missing tweezers. *(c)* A smooth hologram that makes a 4×2 array of tweezers. *(d)* The binary version of hologram (c) makes a satisfactory 4×4 array of tweezers.

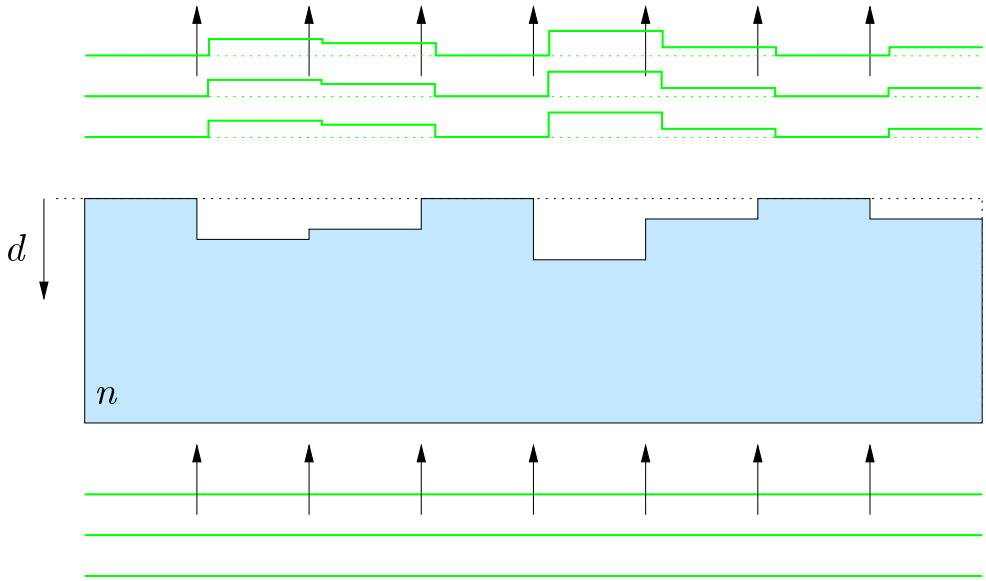

Figure 4.8: *Encoding hase in depth.* A plane wave is incident upon a transparent dielectric material from below.

surface of the dielectric is textured by etching. In this case, the relative phase at $\vec{r}$ is proportional to the etch depth, $d(\vec{r})$,

$$\Phi^{in}(\vec{r}) = 2\pi(n-1)\frac{d(\vec{r})}{\lambda}. \tag{4.26}$$

In practice, it is quite difficult to create more than two depth levels with etching techniques. Therefore, all of the holograms that we have made and tested have been binary. Our binary holograms are made from fused-silica, which has an index of refraction of 1.456 at the wavelength of our trapping laser, $\lambda = 532\,nm$. Therefore, phase shifts of π radians were obtained by etching to depths of $\lambda/2(n-1) = 583\,nm$. We have collaborated with the Spalding Group at Illinois Wesleyan University to fabricate holograms. All the fabrication techniques described here were designed and executed by Prof. Spalding and his students. The fabrication process has three

main steps: the creation of a photo mask, the creation of an etching mask, and etching, Fig. 4.9.

We first create a mask for the exposure of photoresist. The numerical techniques described in previous sections are applied to calculate a binary phase profile. Then, the phase profile is printed as a binary image, with black pixels representing a relative phase shift of π radians, and white pixels representing a phase shift of 0 radians. Finally, this image is photo-reduced onto a transparent film to the actual dimensions of the hologram. Each hologram is a square of width $2f = 3.24\,mm$, where f is the focal length of our microscope objective lens.

We then create a reactive-ion etch mask on the surface of the fused-silica substrate. First, the $1\,mm$ thick substrate is coated with a $250\,\mathring{A}$ layer of chrome, and a $1.76\,\mu m$ layer of positive photoresist, Fig. 4.9(a). The photomask created earlier is placed over the layer of photoresist, and the entire sample is exposed to UV radiation, Fig. 4.9(b). The photomask is removed and sections of exposed photoresist are chemically etched away, revealing parts of the chrome layer, Fig. 4.9(c). The exposed chrome is etched away, exposing the sections of silica to be etched, Fig. 4.9(d).

The exposed sections of silica are etched to a depth of $583\,nm$, Fig. 4.9(e). RF power ionizes and accelerates a mixture of carbon tetrafluoride and oxygen. These reactive ions rapidly etch through the photoresist, and are halted by the layer of chrome. The exposed silica surfaces are slowly etched, at a rate of about $5\,\mathring{A}/sec$. Finally, any remaining chrome or photoresist is removed, leaving behind a precisely textured fused-silica surface, Fig. 4.9(f).

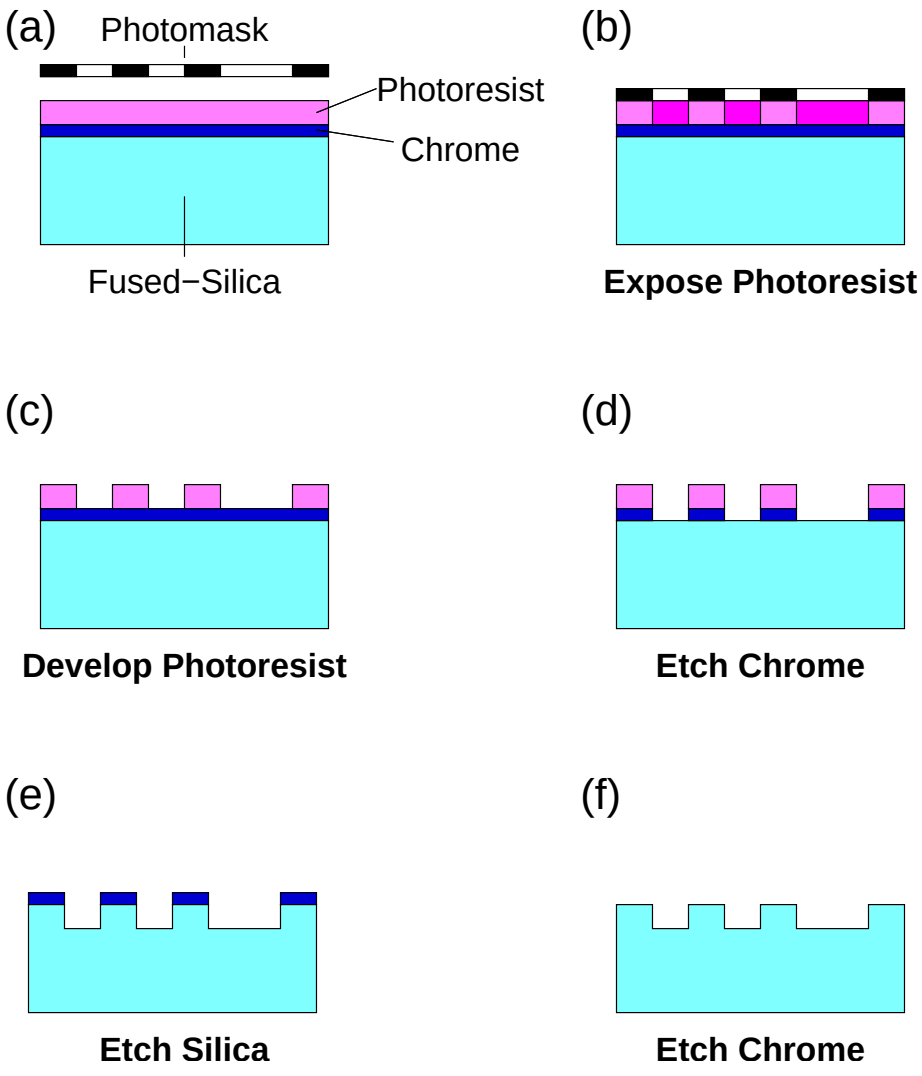

Figure 4.9: *Fabricating holograms with reactive ion etching.*

4.4 Design Tolerances

In this section, we describe how fabrication flaws affect the efficiency of a holographic optical tweezer array. First, we present numerical calculations of efficiency as a function of etch depth. Second, we present numerical and analytical calculations of efficiency as a function of surface roughness. These results can be applied to specify useful tolerances for fabricating holograms.

We define the efficiency of a hologram, $\mathcal{E}$, to be the fraction of incident laser energy that ends up in the planned tweezer pattern. For simplicity, we compare the intensity pattern in the focal plane when the actual hologram is illuminated by a uniform plane wave, $\tilde{I}^f(\vec{\rho})$, to the ideal intensity pattern in the focal plane, $I_0^f(\vec{\rho}) = (2\pi f/k)^2 T^2(\vec{\rho})$. Therefore, the efficiency of a hologram that produces an array of equal intensity tweezers is given by:

$$\mathcal{E} \equiv \frac{\sum_{i=1}^{M^2} T^2(\vec{\rho}_i)\tilde{I}^f(\vec{\rho}_i)}{\sum_{i=1}^{M^2} T^2(\vec{\rho}_i)}. \tag{4.27}$$

The efficiency, $\mathcal{E}$, is a less stringent measure of the agreement between the ideal and actual holograms than the error, ϵ, since it is possible to have $\mathcal{E} = 1$ when $\epsilon > 0$, but $\epsilon = 0$ requires that $\mathcal{E} = 1$. Still, the AA algorithm rarely finds perfectly efficient holograms.

We calculate the efficiency of four standard holograms as a function of the magnitude of the fabrication defects. The four standard holograms are smooth and binary versions of two holograms that produce square arrays of tweezers. One array is 4×4 and the other is 20×20. Both arrays have the same lattice constant. We calculated all four holograms twenty times, and selected the most efficient hologram from each group to use in the both efficiency studies.

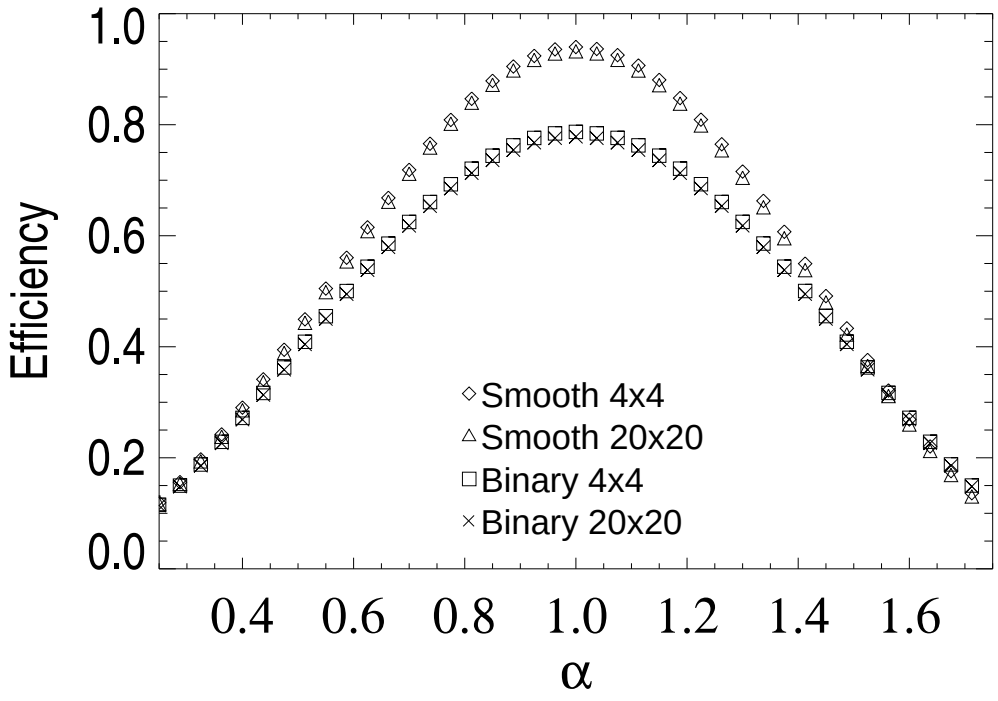

Figure 4.10: *Efficiency of hologram versus phase scale factor.*

The depth of phase modulations created by an etched hologram is proportional to the etch depth, Eq. 4.26. If the etch rate is not precisely controlled, or the hologram is illuminated with light of the wrong wavelength, the actual phase profile, $\tilde{\Phi}^{in}(\vec{r})$, will differ from the design $\Phi^{in}(\vec{r})$ by a scale factor, $\tilde{\Phi}^{in}(\vec{r}) = \alpha\Phi^{in}(\vec{r})$. As α departs from unity, most of the laser light that does not contribute to the tweezer array is focused to the position of the unmodified laser beam. Fig. 4.10 shows the efficiency of the four standard holograms as a function of phase-scale factor, α. Even the ideal, $\alpha = 1$, holograms are not perfectly efficient. Both smooth holograms have ideal efficiencies near 95%. The binary holograms are less efficient, with ideal efficiencies near 80%. Fig. 4.10 suggests that a hologram's efficiency does not depend strongly on the etch depth.

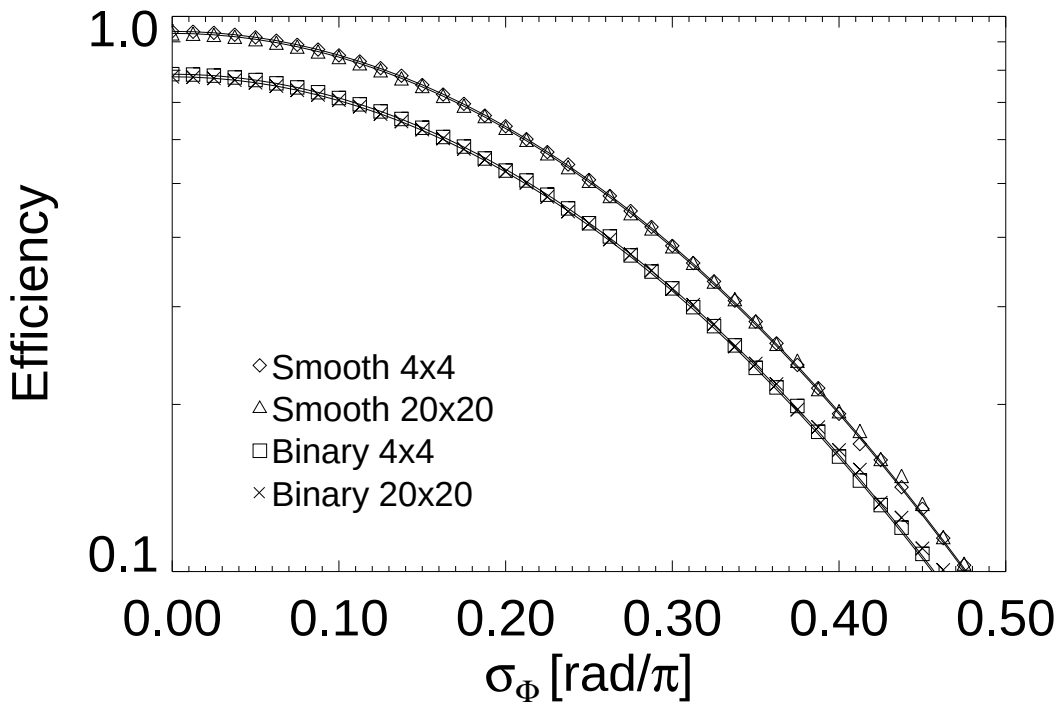

Figure 4.11: *Efficiency of hologram versus roughness.* The symbols are numerically calculated efficiency for specific manifestations of $\eta(\vec{r})$, while the solid curves are the analytically calculated ensemble-averaged efficiencies.

Reactive ion-etching of fused-silica leaves a rough surface, which adds random fluctuations to the phase profile of the trapping laser as it leaves the hologram. Spalding *et al.* have measured the surface topography of fused-silica after etching. They found a Gaussian distribution of etch depths, with a standard deviation of $60\,nm$ or $\pi/10$ radians with $532\,nm$ illumination. The etch depth fluctuations are uncorrelated down to length scales of less than $280nm$. Fig. 4.11 shows the efficiency of the four standard holograms with increasing surface roughness. The roughness was numerically modeled by adding uncorrelated Gaussian noise to the

phase profiles,

$$\tilde{\Phi}^{in}(\vec{r}) = \Phi^{in}(\vec{r}) + \eta(\vec{r}), \tag{4.28}$$

where the probability distribution of the noise is given by

$$\rho(\eta) = \frac{1}{\sqrt{2\pi}\sigma_{\Phi}} \exp\Big[\frac{-\eta^2}{2\sigma_{\Phi}^2}\Big]. \tag{4.29}$$

The decay of a hologram's efficiency with increasing surface roughness can also be calculated analytically. Combining Eqs. 4.6 and 4.28, the electric field profile in the focal plane is found to be

$$\tilde{E}^f(\vec{\rho}) = \frac{k}{2\pi f} \int d^2\vec{r}\, \exp[i(k\vec{r}\cdot\vec{\rho}/f + \Phi^{in}(\vec{r}) + \eta(\vec{r}))], \tag{4.30}$$

for a particular manifestation of the noise profile, $\eta(\vec{r})$. Averaging over all the possible phase profiles,

$$\langle\tilde{E}^f(\vec{\rho})\rangle = \frac{k}{2\pi f} \int d^2\vec{r}\, \exp[i(k\vec{r}\cdot\vec{\rho}/f + \Phi^{in}(\vec{r}))]\, \langle\exp[i\eta(\vec{r})]\rangle, \tag{4.31}$$

Now, applying Eq. 4.29,

$$\langle\exp[i\eta(\vec{r})]\rangle = \int_{-\infty}^{\infty} d\eta\, \rho(\eta) \exp[i\eta] = \exp[-\sigma_{\Phi}^2/2], \tag{4.32}$$

so

$$\langle\tilde{E}^f(\vec{\rho})\rangle = \exp[-\sigma_{\Phi}^2/2] E^f(\vec{\rho}), \tag{4.33}$$

and

$$\langle \tilde{I}^f(\vec{\rho}) \rangle = \exp[-\sigma_\Phi^2] I^f(\vec{\rho}), \tag{4.34}$$

and finally,

$$\langle \mathcal{E}(\sigma_\Phi) \rangle = \mathcal{E}(0) \exp[-\sigma_\Phi^2]. \tag{4.35}$$

This analytical prediction of the ensemble averaged efficiency is compared alongside the numerical calculation of the efficiency for specific manifestations of $\eta(\vec{r})$ in Fig. 4.11. The ensemble-averaged efficiency does a fine job of describing the efficiency for specific manifestations of the noise profile. Note that the absolute scale of efficiency is set by the efficiency of the ideal hologram, $\sigma_\Phi = 0$, while the decay of the efficiency as a function of roughness is the same for all holograms. Substituting the measured value of the surface roughness for fused-silica, $\sigma_\Phi \approx \pi/10$, we find that our holograms' efficiencies are decreased by about 10% due to surface roughness.

4.5 Trapping with Holograms

Having discussed the design and fabrication of holograms that generate optical tweezer arrays, Figs. 4.12(a) and (b), we now discuss the incorporation of these holograms into a conventional optical tweezer apparatus. A holographic optical tweezer array can be created from a conventional optical tweezer setup by adding a hologram at the back aperture of the microscope objective lens, Fig. 4.1. However, this destroys the ability to image through the lens. Therefore, we project an image of the illuminated hologram onto the back aperture of the microscope objective with

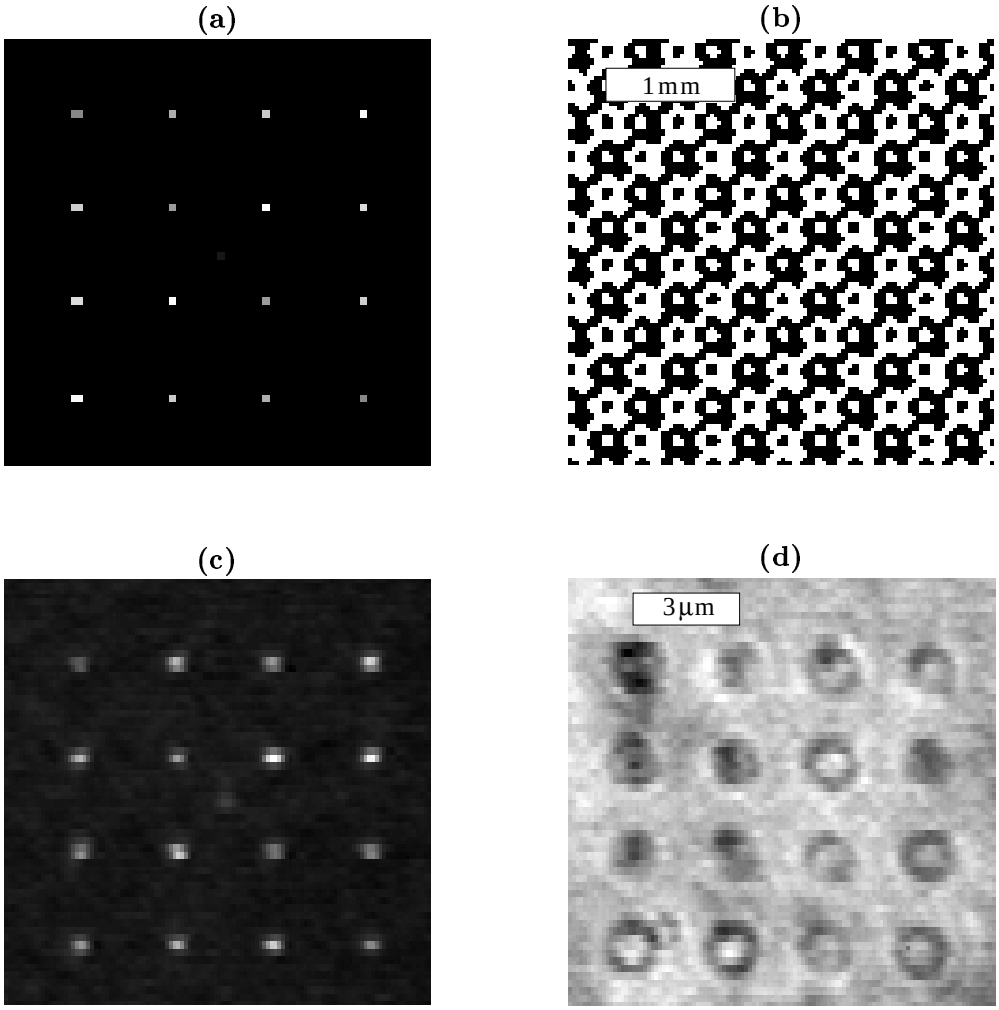

Figure 4.12: *Holographic optical tweezer arrays. (a)* The intensity profile of the ideal tweezer array. *(b)* The phase profile of the ideal hologram. *(c)* The intensity profile of a tweezer array created with the actual hologram. *(d)* One micron silica spheres trapped in the array with $100\,mW$ of laser light.

a simple telescope, as shown in Fig. 4.13. Fig. 4.12(c) shows the intensity profile of an optical tweezer array in the focal plane, created and observed by the optical train shown in Fig. 4.13. A second telescope allows the entire array to be moved across the microscope's field of view by rotating a gimbal-mounted mirror, as described in Section 2.2. Individual tweezers can be selectively extinguished in the intermediate focal planes of the telescopes, where the individual beams that form them come to a focus. Figs. 4.12(d), 4.14, 4.15 and 4.16, show spheres trapped on a small square array, a small triangular array and a large square array of optical tweezers.

4.6 Applications of Holographic Optical Tweezer Arrays

The current realization of holographic optical tweezers, HOTs, will enable many new experiments in the collective behavior of colloidal systems. HOTs are well suited to measure the many-body interactions between colloidal particles [100] and to explore the equilibrium phase behavior and transport of colloidal crystals in external potentials. For example, consider Fig. 4.16 where $1.5\,\mu m$ diameter silica spheres are trapped on a 20×16 square array. Outside of the region illuminated by the array, the dense two-dimensional layer of spheres have six-fold order. However, spheres lying on the tweezer array fill only half of the traps, forming a square lattice whose lattice constant is stretched by a factor of $\sqrt{2}$ and rotated by 45° relative to the tweezer array. This occurs because the lattice constant of the tweezer array is less than the diameter of the spheres. Such experiments may shed light on superconducting vortex structures [101, 102] and surface phase transitions [103, 104].

Yet holographic optical tweezer technology is still in its earliest stage of development, and several new technological advances will soon dramatically increase the

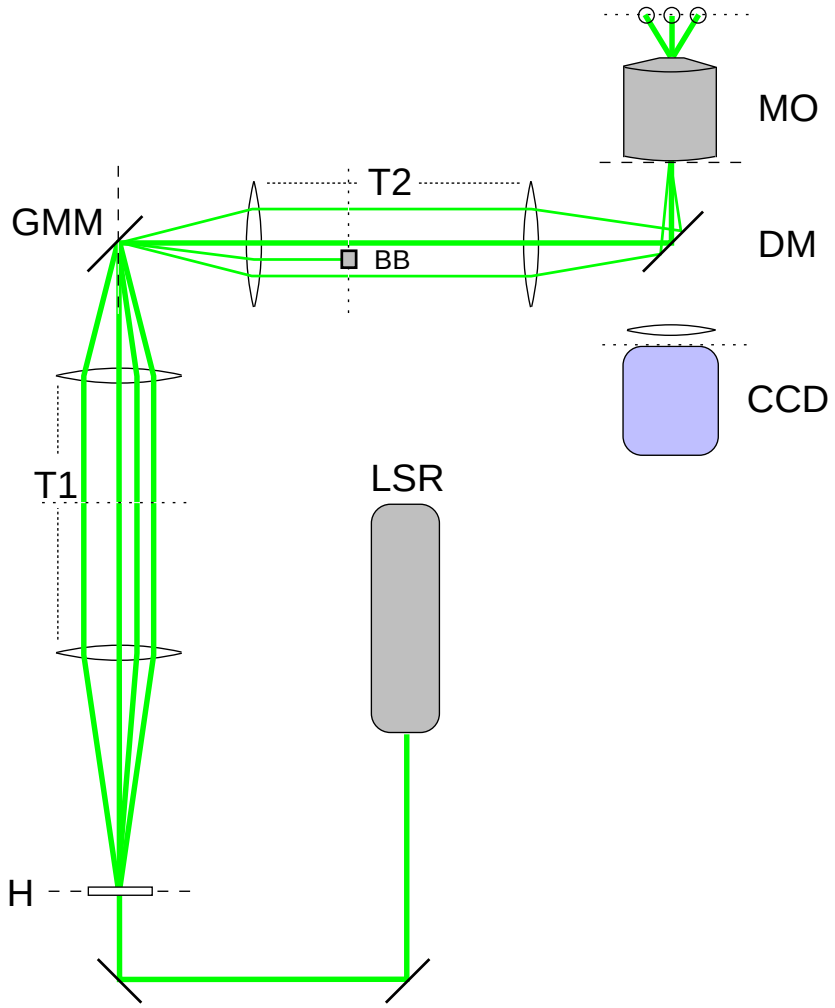

Figure 4.13: *Optical train generating holographic optical tweezer arrays.* A laser, (Coherent Verdi, $\lambda = 532nm$, $P = 10 \rightarrow 5000\,mW$), **LSR**, emits a Gaussian laser beam. A hologram, **H**, modulates the phase of the beam, splitting it into several beams. A simple telescope, **T1**, projects an image of the hologram onto the surface of a gimbal-mounted mirror, **GMM**. A second telescope, **T2**, projects a slightly enlarged image of the hologram onto the back aperture of the microscope objective lens. A beam block, **BB**, can be placed in the intermediate focal plane of either telescope to block unwanted beams. A dichroic mirror, **DM**, placed between the microscope objective lens, (Olympus S-Plan Apochromatic, $NA = 1.4$, $f = 1.62\,mm$, $100\times$), **MO**, and the CCD camera, **CCD**, allows for simultaneous trapping and imaging. The dotted lines show planes that are conjugate to the focal plane of the microscope objective lens, and dashed-lines show planes that are conjugate to its back aperture.

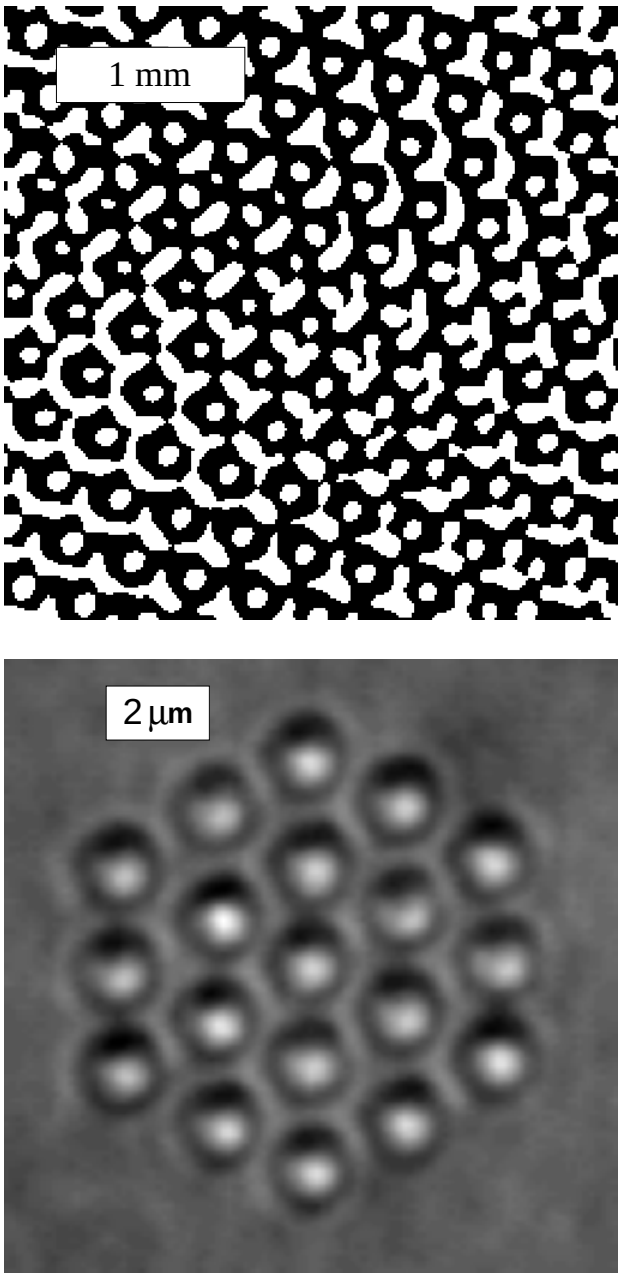

Figure 4.14: *19 point triangular array. (top)* The hologram's phase profile. *(bottom)* Nineteen $1\mu m$ diameter silica spheres suspended in water and trapped in the array, illuminated with $300mW$ of laser light.

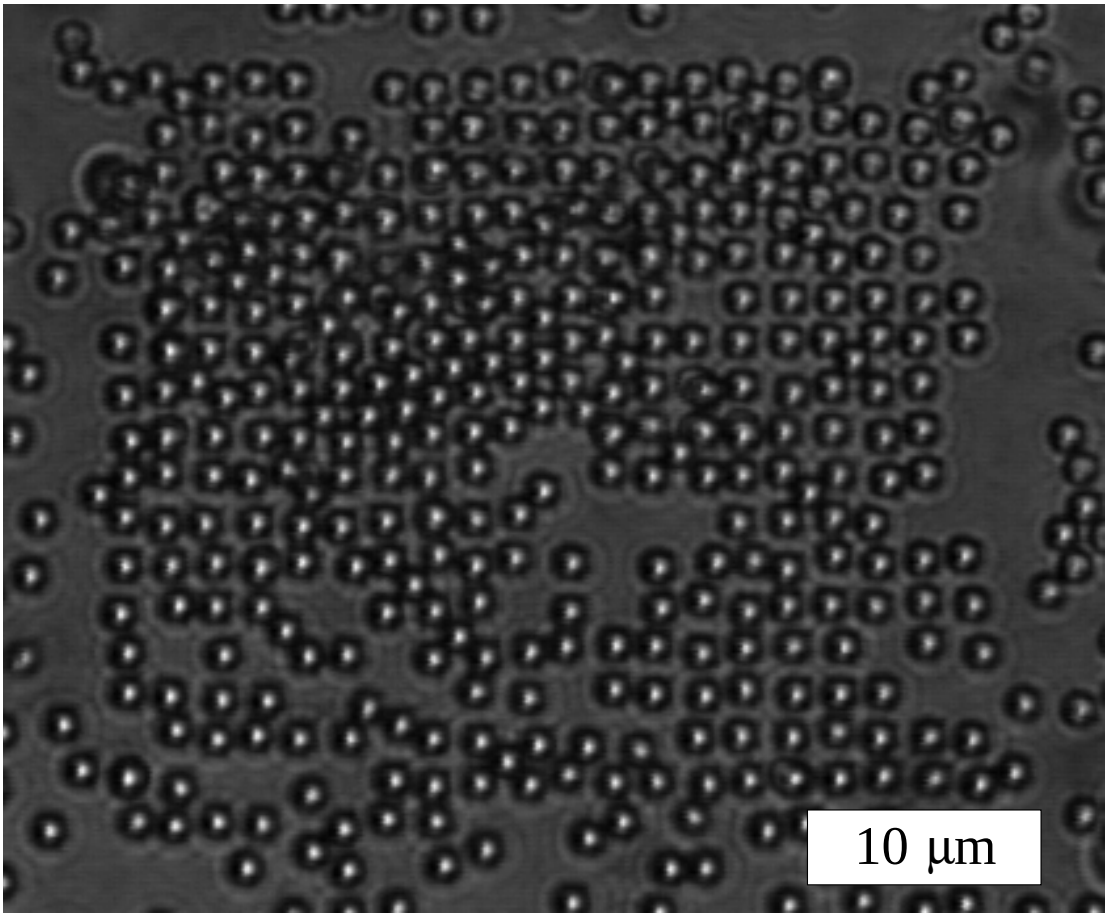

Figure 4.15: 20×20 *square array.* $2\mu m$ diameter polystyrene spheres suspended in water and trapped in the array, illuminated by $1.5W$ of laser light.

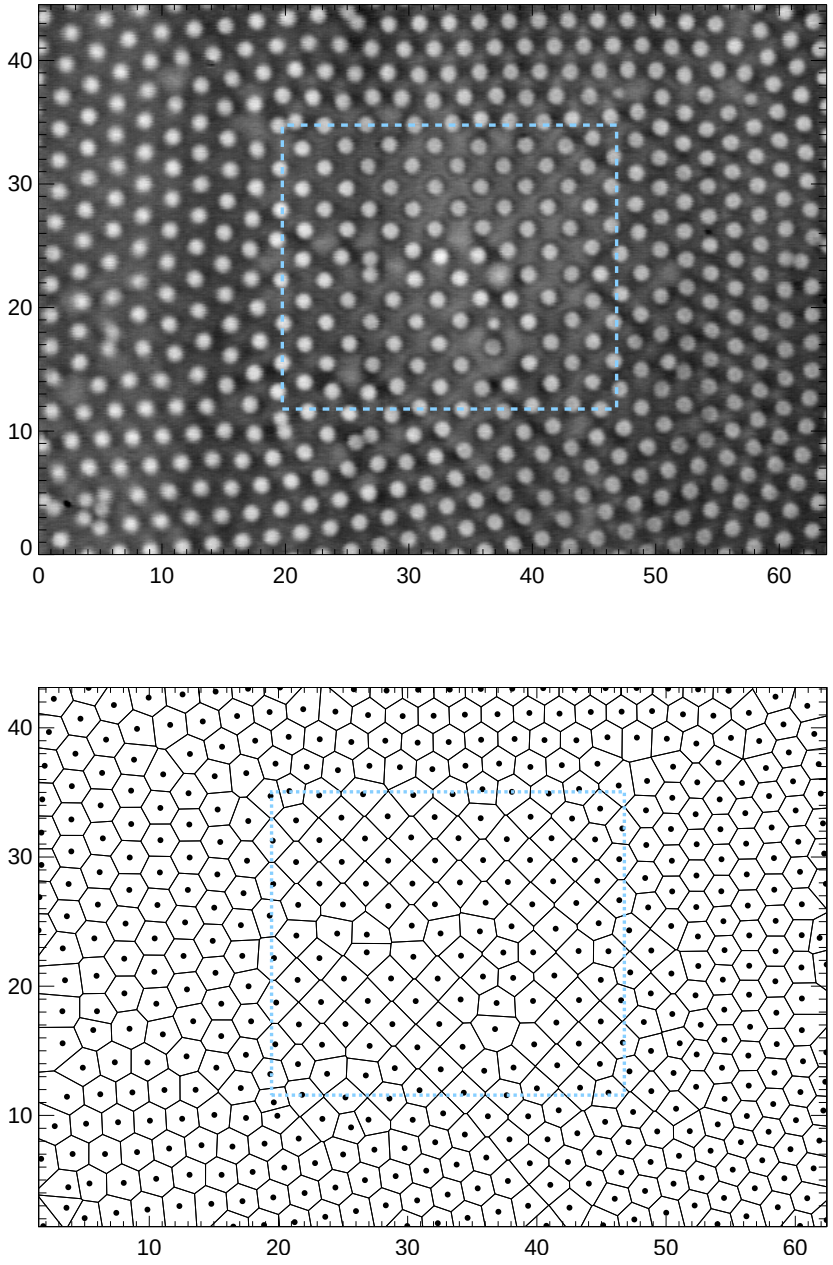

Figure 4.16: $\sqrt{2} \times \sqrt{2}$ *superlattice. (top)* 1.5 μm diameter silica spheres trapped on a 20×16 square array. The region illuminated by the tweezer array lies inside the dashed boundary. *(bottom)* A Voronoi diagram displaying the the two-dimensional Wigner-Seitz cells for each sphere. Note the process of square order extending from bottom of the tweezer array. The above coordinate systems are calibrated in *microns. Data courtesy of P.T. Korda and G.C. Spalding*

utility of HOTs. Most importantly, liquid-crystal spatial light modulators, SLMs, have been introduced that are capable of modulating the phase profile of laser beam continuously from 0 and 2π, and can be updated at speeds of up to $10Hz$ [99]. These devices will allow the creation of time-dependent optical tweezer arrays. Time-addressable SLMs can be combined with the particle tracking techniques of digital video microscopy to create *adaptive optical tweezers*, Fig. 4.17. Adaptive optical tweezers will be able to locate all the particles in the microscope's field of view, calculate a hologram that makes a tweezer array that will grab all the particles, apply the phase modulations to the laser, and trap the particles. Once the particles are trapped, each particle can be moved separately. This technique could be used to efficiently assemble materials textured on the micron scale or to sort microscopic particles. Finally, adaptive optical tweezers could gently and securely trap large objects, in the size range of 10 to $100\mu m$, such as eukaryotic cells, which are not well suited to trapping by conventional tweezers. Currently, one traps large cells by focusing a very bright tweezer onto a single spot with high dielectric contrast, such as an organelle. Often free to move within the cytoplasm, a single organelle is not an effective handle for the entire cell. Additionally, the high laser power of the single tweezer can cause irreparable damage to the organelle. By weakly grabbing onto many organelles simultaneously, adaptive optical tweeezers could gently manipulate large cells, controlling both their position, orientation and shape.

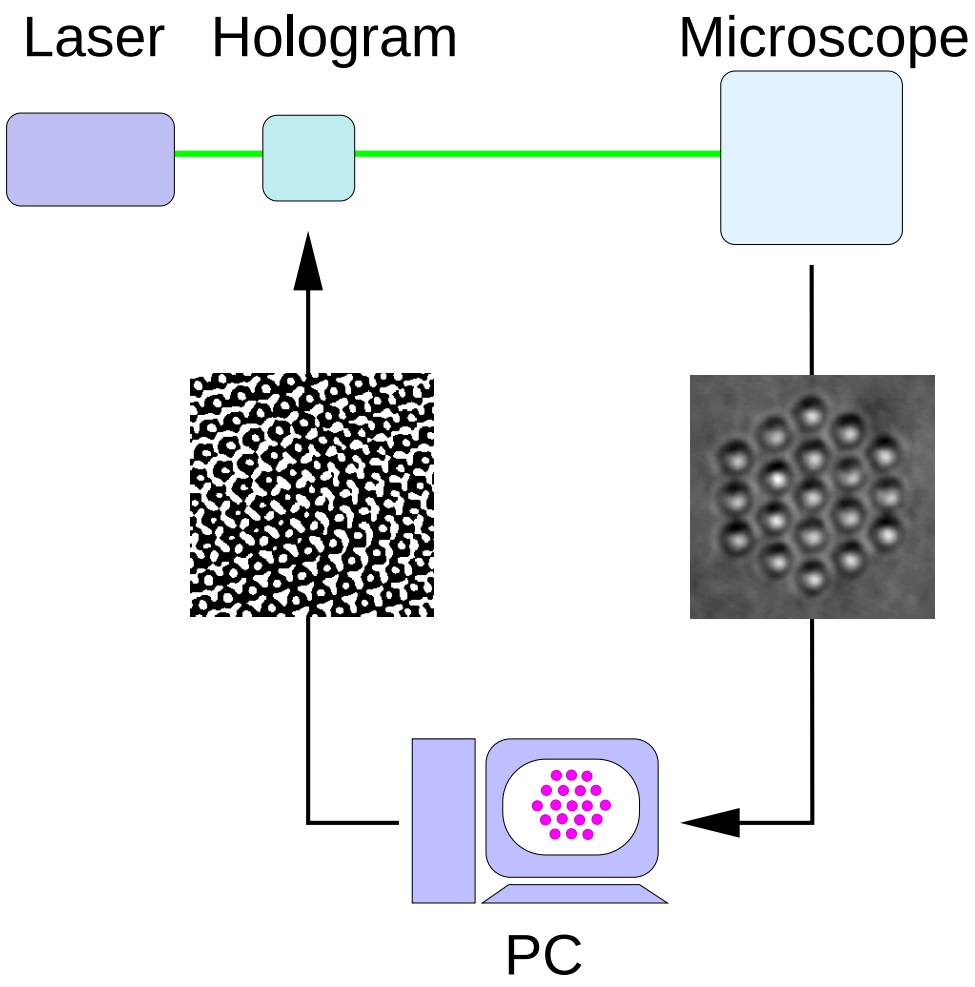

Figure 4.17: *Adaptive optical tweezers.* A microscope images a suspension of colloidal particles. A personal computer identifies the particles, and calculates a phase-only hologram to trap them. A computer controlled spatial light modulator implements the computer's design, applying a pattern of phase modulations to a laser, which is focused by the microscope to create an array of optical tweezers which traps all of the particles on the screen. Each particle can now be individually manipulated to assemble a structure or to sort particles.

CONCLUSION

We have constructed a second-generation blinking optical tweezers system to study the interactions and dynamics of one or two colloidal particles. We have measured hydrodynamic interactions between two spheres, a sphere and a wall, two spheres near a wall, and one sphere and two parallel walls. The dependence of the measured diffusion coefficients on the configuration of the spheres are accurately fit by the predictions of Stokeslet analysis with no free parameters. While the formulation of Stokeslet analysis in confined geometries can be rather complex, it successfully incorporates many-body effects ignored by the linear superposition approximation, and can be systematically extended to describe weak hydrodynamic coupling of larger many-particle systems.

We have shown that multiple optical tweezers can be created from a conventional optical tweezer apparatus by inserting a hologram into its optical train. We have described methods for designing holograms capable of creating arrays of optical tweezers with any planar geometry. We have fabricated holograms using microlithography and have specified useful design tolerances. Recent advances in spatial light modulators will enable the creation of dynamic optical tweezer arrays capable of adapting to the configuration and composition of the particles under study.

APPENDIX A

CALIBRATING OPTICAL TWEEZERS WITH REFLECTIVE CONFOCAL MICROSCOPY

The optical tweezer has become the instrument of choice for biologists measuring forces exerted by biomolecules. In the simplest experiments, [44], one end of a bio-polymer is attached to a micron-sized dielectric sphere and the other end is attached to a fixed surface. An optical tweezer traps the sphere and slowly retracts it from the surface. As the bio-polymer is stretched, it applies a force to the trapped particle, displacing it in the optical tweezer. Assuming that the trapping potential is harmonic, the particle's displacement from the bottom of the well, Δx, is proportional to the force exerted by the bio-polymer, $F = k\Delta x$, where k is the trap's effective spring constant.

In principle, a tweezer's stiffness, k, can be calculated from the optical properties of the trap and the particle. However, existing theories [49, 50] cannot reliably describe the forces on a trapped particle in practical situations. In this regime, where the particle size is comparable to the wavelength of light, trapping forces are extremely sensitive to the geometry and composition of the trapped particle [52] and the optical properties of the trap, all off which are difficult to control precisely. Since experimental conditions are too variable to reliably predict the trapping potential, several techniques have been developed to calibrate a trapped particle's response to an outside force.

First, the trap's stiffness, k, can be extracted by measuring a trapped particle's response to a known force. Typically, one applies a hydrodynamic drag force to the particle by translating the trap at a constant speed, v, [41, 44, 105] and measures the displacement, Δx. Assuming the Stokes form for the hydrodynamic drag constant, $\gamma = 6\pi\eta a$, one equates the trapping and hydrodynamic forces, to calculate the tweezer's spring constant:

$$k = \frac{6\pi\eta a}{\Delta x}\, v. \tag{A.1}$$

The accuracy of this calibration is limited by the uncertainty in the sphere's radius, velocity, and displacement in the trap, as well as and the possibly inaccuracy of the Stokes form of the hydrodynamic drag.

Second, one can measure the tweezer potential from the equilibrium statistical mechanics of a trapped particle [61, 106]. One measures the equilibrium probability distribution of sphere locations in the trap, $P(x) \propto e^{-\beta U(x)}$. Assuming a Boltzmann distribution, one obtains the tweezer potential:

$$U(x) = -k_B T \, \ln[P(x)]. \tag{A.2}$$

This technique requires no knowledge of the sphere's size or hydrodynamics and makes no assumptions about the shape of the tweezer's potential, $U(x)$. However, this equilibrium calibration is difficult because the characteristic thermally-driven displacements of the particle are too small to be reliably resolved with digital video microscopy (DVM), which has a typical spatial resolution of about $20\,nm$.

Third, one can extract useful information about both the particle and the tweezer by observing the non-equilibrium statistical mechanics of a trapped particle [61, 81, 107]. As discussed in Chapter 1, the dynamics of a Brownian particle in a harmonic well are easily described by a Langevin equation, Eq. 1.19. We found that the particle loses memory of its previous locations with a characteristic time scale, $\tau = \gamma/k$. More specifically, the auto-correlation function of particle positions is, according to Eq. 1.21

$$\langle x(t_1)x(t_2)\rangle = \frac{k_B T}{k} e^{-\frac{k}{\gamma}|t_2 - t_1|} \tag{A.3}$$

Therefore, one can determine both the trap stiffness k and the viscous drag parameter γ by measuring the autocorrelation function [81] or its Fourier transform [61, 107] with temporal resolution finer than τ. However, τ is typically much shorter than the interval between video frames.

In principle, the calibration of an optical tweezer by the observation of the statistical mechanics of a trapped particle provides more information than simple force-response measurements, and requires fewer assumptions. In practice, faster and more accurate particle tracking methods are needed to implement these techniques. While many high-resolution tracking techniques have been developed, these techniques all share one common feature: they do not record images of the particles that they track. The simplest technique focuses a white-light image of the trapped particle onto the center of a quadrant photodiode detector [105]. The position of the particle can be determined to within $1\,nm$ from the relative strength of signals from the four photodiodes. While a CCD camera integrates light over its exposure time, a photodiode generates a current signal that is essentially proportional to

the instantaneous light intensity. Fast data acquisition systems can record particle positions at rates up to $125\,kHz$. Other non-imaging techniques have similar resolutions [61, 81, 107–109].

In this appendix, we introduce an alternative fast tracking technique that images the trapped particle. This technique, *reflective confocal microscopy*, RCM, records one dimensional images of particles at $400\,Hz$ with a spatial resolution of about $5\,nm$. While this technique is neither as fast nor as sensitive as non-imaging techniques, it can track multiple particles along a line and could be extended to create high resolution three-dimensional images.

A.1 Reflective Confocal Microscopy

A.1.1 Setup

In DVM, the image of a typical dielectric colloidal sphere has low contrast, and the pixellation of video signals further degrades the image quality, Fig. 2.2. The image is formed by bright field microscopy, where the sample rests in the focal plane of a microscope objective and a bright light source projects light into the microscope objective through the sample, Fig. 2.1. Light bends as it travels through index of refraction gradients, and is focused to form an image of the sample superimposed over a bright background.

The contrast of these images can be dramatically improved if the image is formed with reflected light. In RCM, a probe laser beam, focused to a diffraction limited spot by a microscope objective lens, illuminates a small volume in the objective lens' focal plane. If no particle is found within the laser's focal spot, the laser light is transmitted through the sample. If a particle lies within the focus of the laser

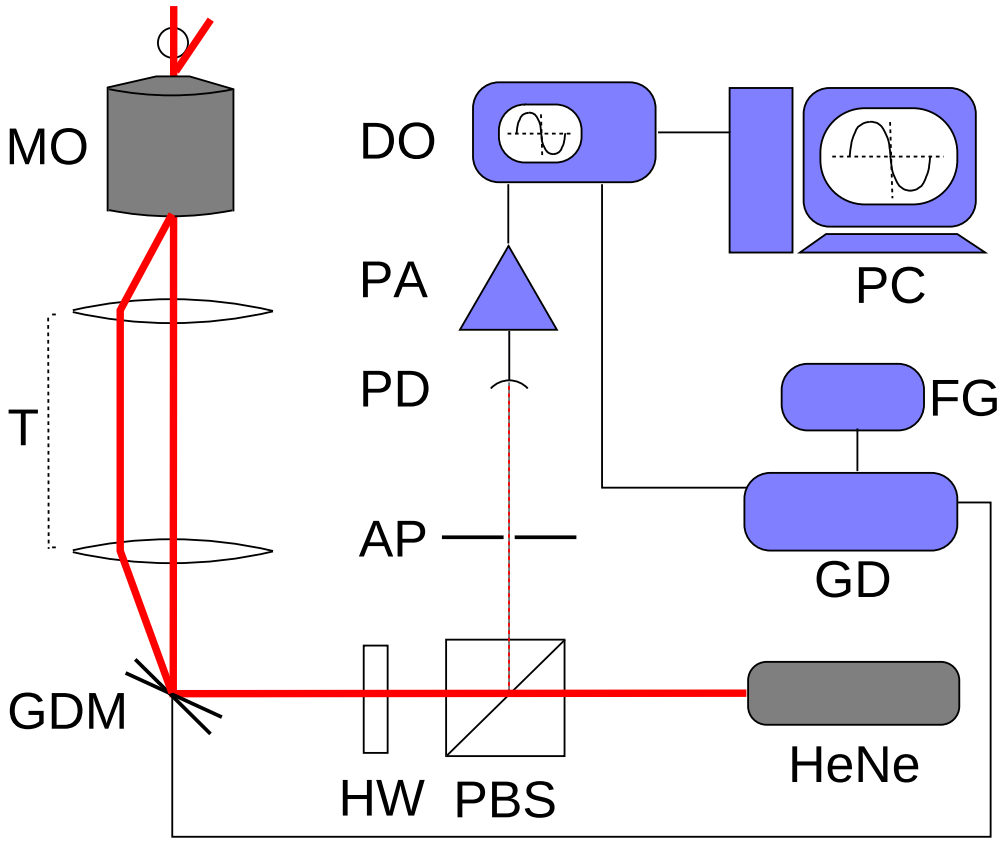

Figure A.1: *Reflective Confocal Microscopy.*

beam, a fraction of the laser light will be reflected [52] back through the objective lens and collected by a photodiode. An image is formed by recording the intensity of reflected light as the focused spot of laser light is scanned across the field of view. A colloidal particle appears as a peak in the intensity of reflected light, Fig. A.2.

A schematic diagram of our RCM setup is shown in Fig. A.1. A helium-neon laser (Uniphase HeNe 1107P, $\lambda = 633\,nm$), labelled **HeNe**, emits $4\,mW$ of laser light. After passing through a polarizing beam splitter, **PBS**, a half-wave plate, **HW** rotates the beam's polarization by 45°. A galvanometer-driven mirror, **GDM**, deflects the beam, controlling the location of the laser's focus. A simple Keplerian

telescope, **T**, forms an image of the microscope objective's back aperture on the surface of the galvanometer-driven mirror. A microscope objective lens (Olympus S-Plan Apochromatic, $NA = 1.4$, $f = 1.62\,mm$, $100\times$), **MO**, focuses the laser beam to a diffraction-limited spot in its focal plane. If a particle lies in focal point of the beam, it will reflect a small fraction of the incident laser light. The reflected light follows its original path back towards the laser, but the second pass through the halfwave plate rotates the polarization of the beam by an additional 45°. The polarization of the returning laser light has now been rotated a total of 90° and is reflected by the polarizing beam splitter. The reflected light passes through an aperture, **AP**, and is collected by a photodiode, **PD**. The signal from the photodiode is amplified by a current pre-amplifier (Stanford Research SR570), **PA**, stored in a digital oscilloscope (Hewlett Packard 35670A), **DO**, and transferred to a personal computer, **PC**, over a GPIB interface, Fig. A.2. The galvanometer driven mirror is controlled by the galvanometer driver (Cambridge Technology, 603X Dual-Axis Mirror Positioning System), **GD** that positions the mirror according to a signal provided by a function generator, **FG**. A dielectric capacitive sensor in the galvanometer-driven mirror returns the position of the mirror to the galvanometer driver for feedback. This signal is recorded by the digital oscilloscope and transferred to the personal computer, to track the position of the laser's focus, Fig. A.2. For calibration, this signal can be compared to a trajectory of the laser focus measured with DVM.

Particle trajectories extracted from RCM images have enough spatial and temporal resolution to study the dynamics of a particle trapped in an optical tweezer. RCM images of colloidal spheres have better contrast and less pixellation than images formed with DVM, Fig. A.3. The pixellation of the image is limited by the

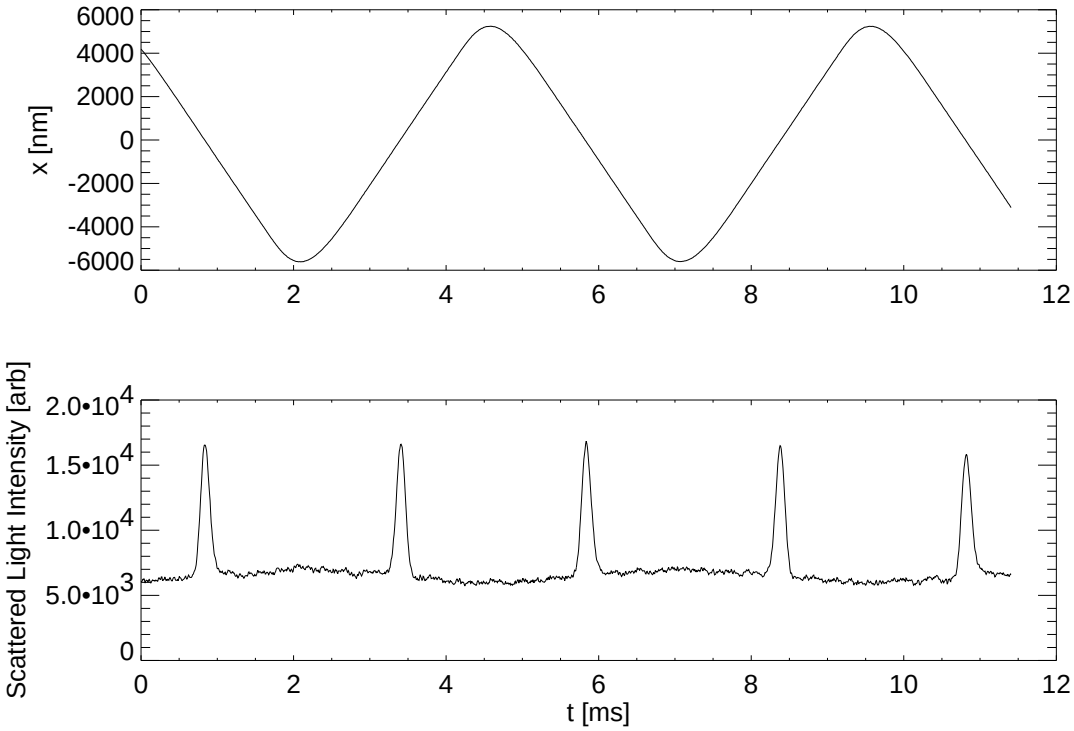

Figure A.2: *Raw RCM Data. (top)* The trajectory of the laser focus, as detected by a dielectric capacitive sensor in the galvanometer-driven mirror. *(bottom)* The intensity of reflected light, as recorded by the photodiode. The multiple peaks are consecutive images of one sphere, separated by $1/400\,sec$.

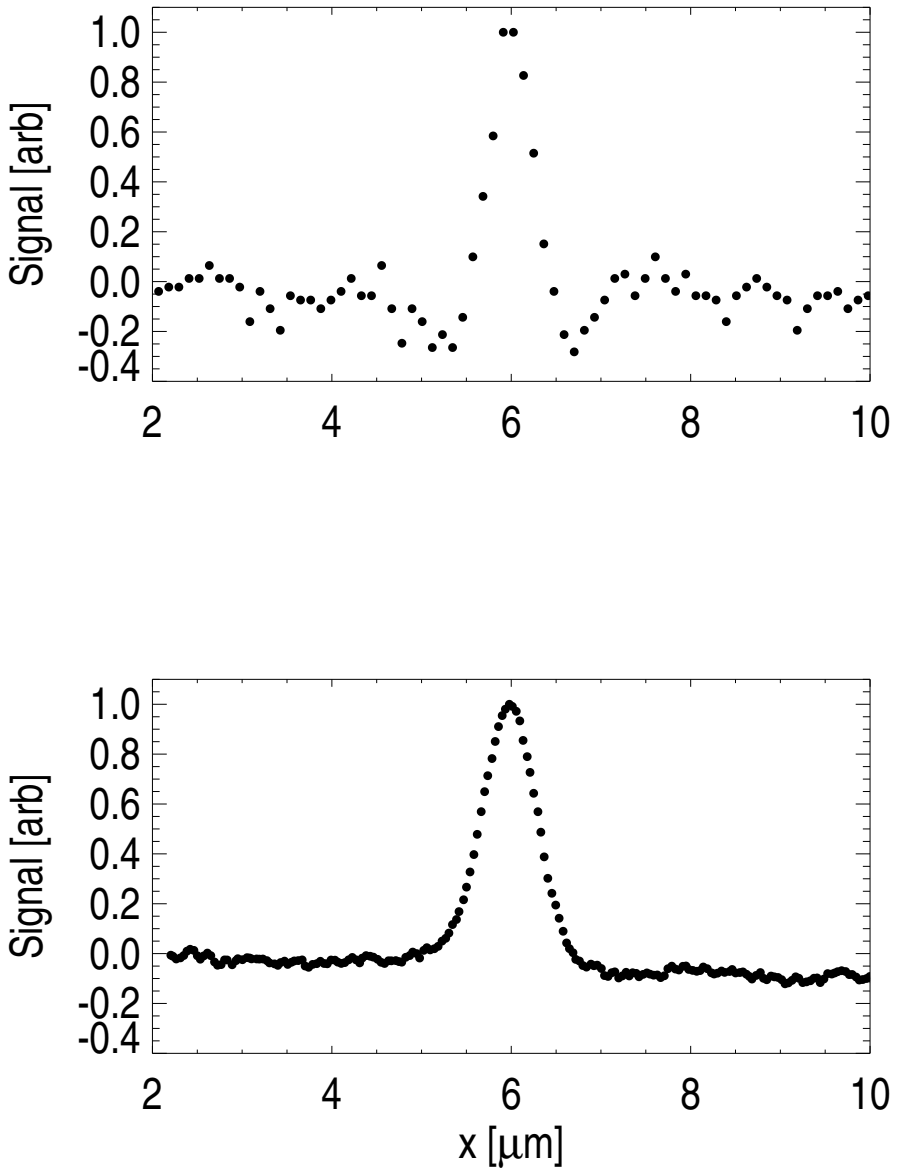

Figure A.3: *DVM versus RCM (top)* The image of one micron silica particle with DVM. *(bottom)* The same sphere imaged with RCM.

sample rate of our digital oscilloscope. At a $22\,kHz$ sample rate, the RCM image of a $1\,\mu m$ sphere contains about 50 pixels, while a one-dimensional slice of a DVM image of the same sphere has only about 13 pixels. The particle location is identified as the maximum of each peak. We determine the maximum of each peak to sub-pixel accuracy by fitting the pixels near the peak of the image to a parabola. While DVM has a typical spatial resolution of about $20\,nm$, [33], this technique reliably locates particles to within $\delta x = 5\,nm$. RCM's temporal resolution is determined by the scan rate of the probe laser, which was limited by the galvanometer to $200\,Hz$. While DVM updates particle locations at $60\,Hz$, our RCM setup updates the particle location at $400\,Hz$. Indeed, RCM can resolve the motions of a particle in an optical tweezer, Fig. A.4.

A.2 Equilibrium Measurement of Tweezer Potential

We now apply RCM to measure the potential felt by a particle trapped in an optical tweezer. A frequency-doubled Nd:YVO laser (Coherent Verdi, $\lambda = 532\,nm$, $P = 25\,mW$) forms an optical tweezer in the focal plane of a microscope objective. The tweezer confines a one micron diameter silica sphere ($a = (0.495 \pm 0.025)\,\mu m$, Duke Scientific, Cat. No. 8100) to a small volume just beyond the microscope objective's focal plane, Fig. A.5. The divergence of the scanned probe laser is adjusted to displace the focal point of the probe so that it passes through the center of the trapping volume, maximizing the reflected light signal. The trajectory of the sphere in the tweezer is recorded for 27 *sec*, and extracted using the techniques described above, Fig. A.4.

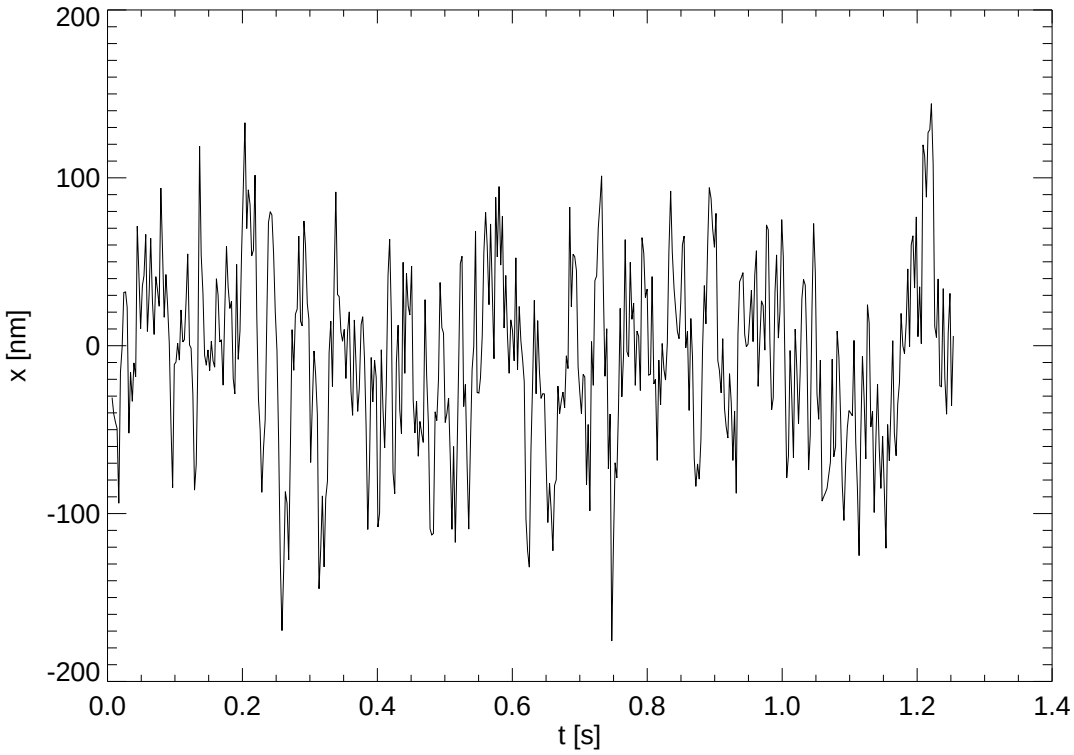

Figure A.4: *Particle trajectory measured with RCM.* Trajectory of $1\,\mu m$ silica sphere in a $25\,mW$ optical tweezer.

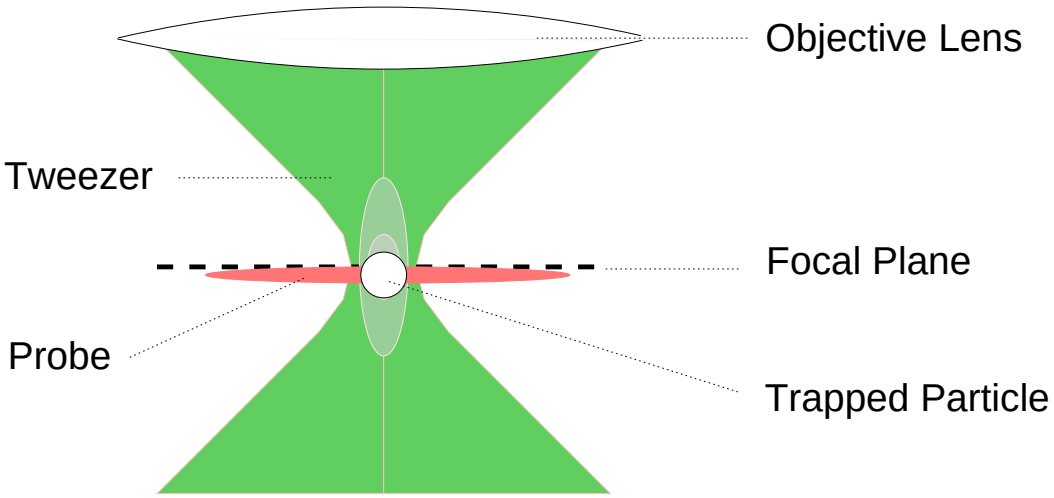

Figure A.5: *Probing tweezer dynamics.* An optical tweezer traps a dielectric particle just beyond the focal plane of the microscope objective. A probe laser scans through the center of the particle, recording the particle location. The probe is shown in time averaged form as a blurred line through the particle.

The observed particle positions are compiled to calculate to the probability distribution of sphere locations, $P(x)$, Fig. A.6. Assuming a Boltzmann distribution, the potential experienced by the particle in the optical tweezer is extracted using Eq. A.2 and is plotted in Fig. A.7. As expected, this potential is well-approximated by a harmonic potential:

$$U(x) = \frac{1}{2}kx^2. \tag{A.4}$$

Optical tweezer potentials are typically much deeper than a few k_BT, and a trapped particle buffeted by thermal fluctuations only wanders within a few k_BT of its potential minimum. Therefore, it is no surprise that a particle trapped in an optical tweezer feels a harmonic potential. A fit to this form yields, $k = (3.00 \pm 0.04) \times 10^{-4} \, \frac{k_BT}{nm^2}$ about $1 \, \frac{fN}{nm}$.

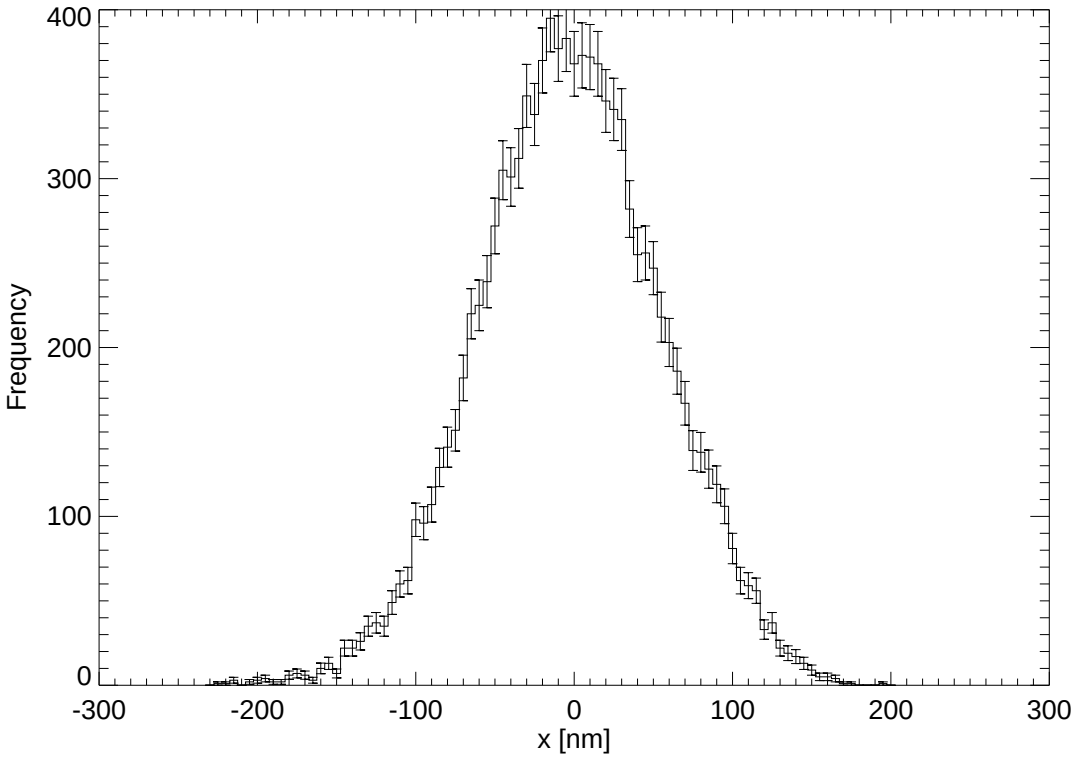

Figure A.6: *Probability distribution of particle locations in a* $25\,mW$ *optical tweezer.*

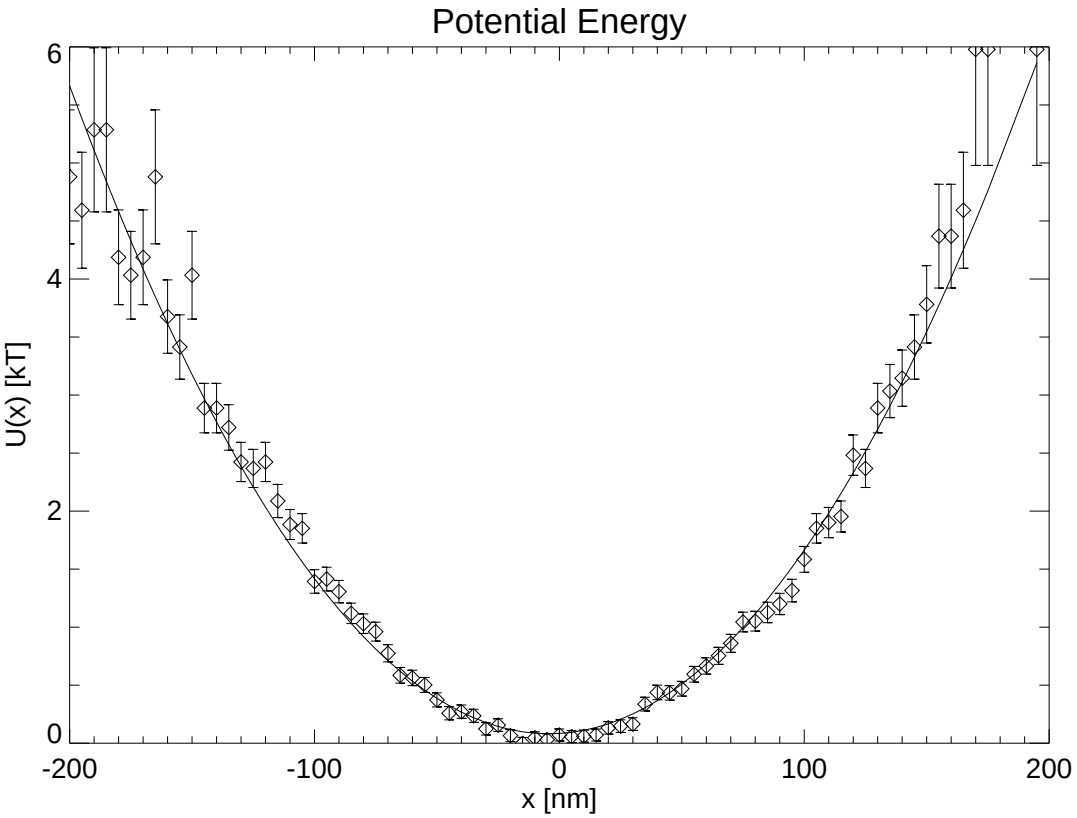

Figure A.7: *The potential of a particle trapped in an optical tweezer made with* $25\,mW$ *of laser light.* The solid curve is a fit to a harmonic potential, Eq. A.4.

We can determine the effective force resolution of this technique. Identifying the force resolution, δF, as the force experienced by the sphere at its minimum resolvable displacement, $\delta F = k\,\delta x$, we find that $\delta F = 0.0014\,k_BT/nm = 6\,fN$. This force resolution is typical of optical tweezer measurements [23, 105].

We can estimate the depth of the optical trap. Since the trapping laser is focused to a diffraction limited spot, the width of the trap is about the wavelength of light, λ. Assuming that the trap is harmonic over this range, the depth of the trap, U_o, is approximately:

$$U_o \approx \frac{1}{2}k\left(\frac{\lambda}{2}\right)^2. \tag{A.5}$$

In this case, $\lambda = 532\,nm$, and the trap is about $10\,k_BT$ deep.

A.3 Non-equilibrium Measurement of Tweezer Stiffness and Hydrodynamic Drag

Let us now reanalyze the same data, considering the trapped sphere's approach toward equilibrium. Fig. A.8 shows the decay of the auto-correlation function. Fits to Eq. A.3 yield a tweezer stiffness, $k = (3.1 \pm 0.1) \times 10^{-4}\,\frac{k_BT}{nm^2}$, and a hydrodynamic drag constant, $\gamma = (2.9 \pm 0.1) \times 10^{-6}\,\frac{k_BTs}{nm^2}$. The tweezer strength agrees well with the equilibrium result, but the viscous drag term is higher than predicted from the Stokes form, $\gamma = 6\pi\eta a = 2.4 \times 10^{-6}\,\frac{k_BTs}{nm^2}$. In this case, the increased drag is the result of hydrodynamic coupling of the sphere to a wall. As we saw in Chapter 3,

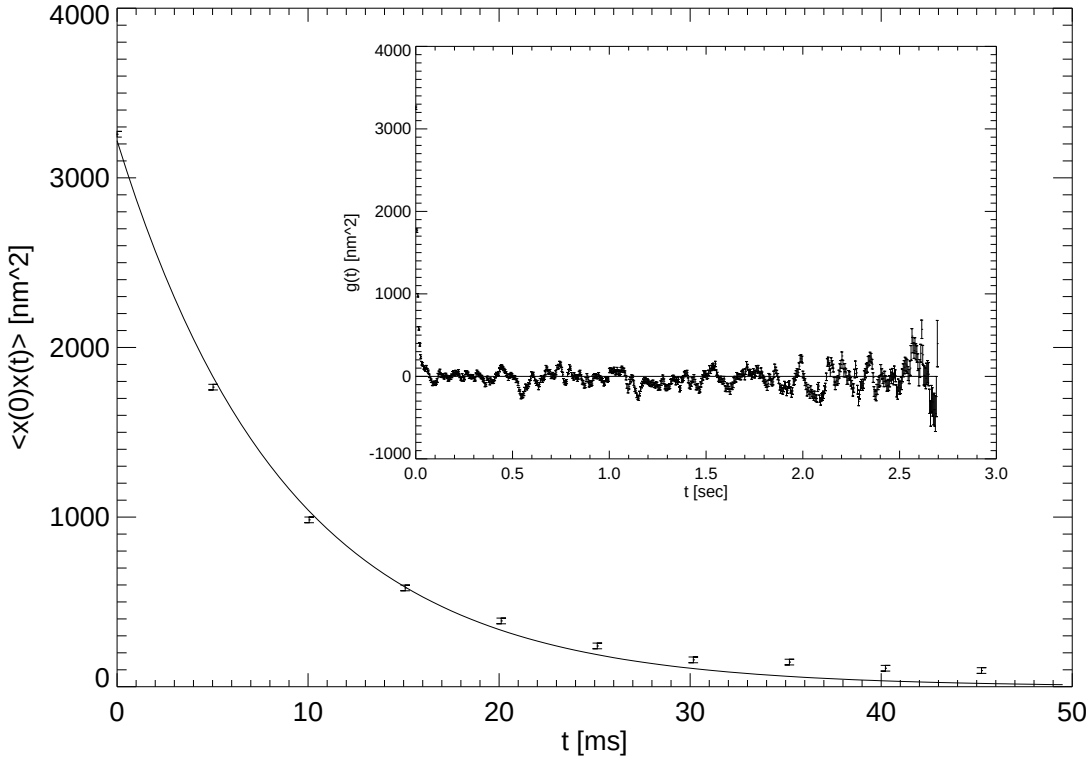

Figure A.8: *Decay of position autocorrelation function.* The main plot shows the short time behavior, and the inset shows the behavior over time scales much longer than the relaxation time, $\tau = \gamma/k$. Solid curves in both plots are fits to Eq. A.3.

the viscous drag on a particle of radius a a distance h above a wall is

$$\frac{\gamma(h)}{6\pi\eta a} = 1 + \frac{9}{16}\frac{a}{h} + \mathcal{O}\left(\frac{a^3}{h^3}\right). \tag{A.6}$$

In this experiment, the ball was trapped $h = (2.5 \pm 1.0)\,\mu m$ above a wall, so that Eq. A.6 gives $\gamma(h) = (2.7 \pm 0.2) \times 10^{-6}\,\frac{k_B T s}{n m^2}$, which agrees well with the measured value. This highlights a previously noted [107, 110] but never before demonstrated potential pitfall of calibrating optical tweezers with hydrodynamic drag forces. If the appropriate hydrodynamics are not employed in drag force measurements, one can substantially underestimate the strength of the optical tweezer. Therefore, measurements based on the statistical mechanics of particles trapped in an tweezer yield more reliable values of trap stiffness than force/response measurements that assume a form for the hydrodynamic drag on a trapped particle.

A.4 Tweezer Stiffness vs. Laser Intensity

In Section A.3, we described an equilibrium measurement of the potential felt by a one micron diameter silica sphere in an optical trap. This measurement was repeated to extract tweezer potentials for several different laser intensities, from 25 to 250 mW, Fig. A.9. The potentials were fit to a harmonic form to find the tweezer stiffness, k, as a function of the intensity of the trapping laser, Fig. A.10. As expected, higher laser intensities produce stiffer optical tweezers.

Since the size of the trapped particle is comparable to the wavelength of light and we do not have a precise description of the intensity profile of our optical tweezer, we cannot rigorously compare the tweezer's absolute stiffness to any theory. The laser intensity was measured with a power meter (Coherent Lasermate 10W) at the

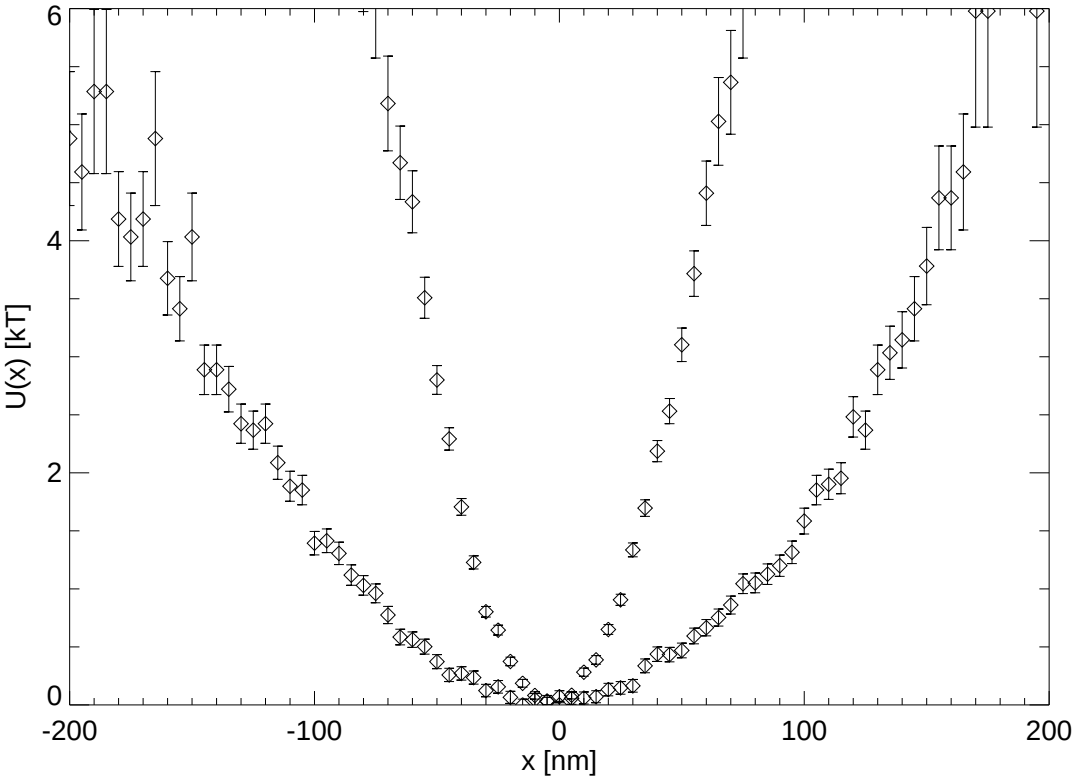

Figure A.9: *Comparison of tweezer potentials at* $25\,mW$ *and* $250\,mW$. Fits to a harmonic potential yield: for 25 mW, $k = (3.00 \pm 0.04) \times 10^{-4}\,\frac{k_B T}{nm^2}$, $x_{rms} = (57.7 \pm 0.3)\,nm$, for $250\,mW$, $k = (2.34 \pm 0.03) 10^{-3}\,\frac{k_B T}{nm^2}$, $x_{rms} = (20.7 \pm 0.2)\,nm$.

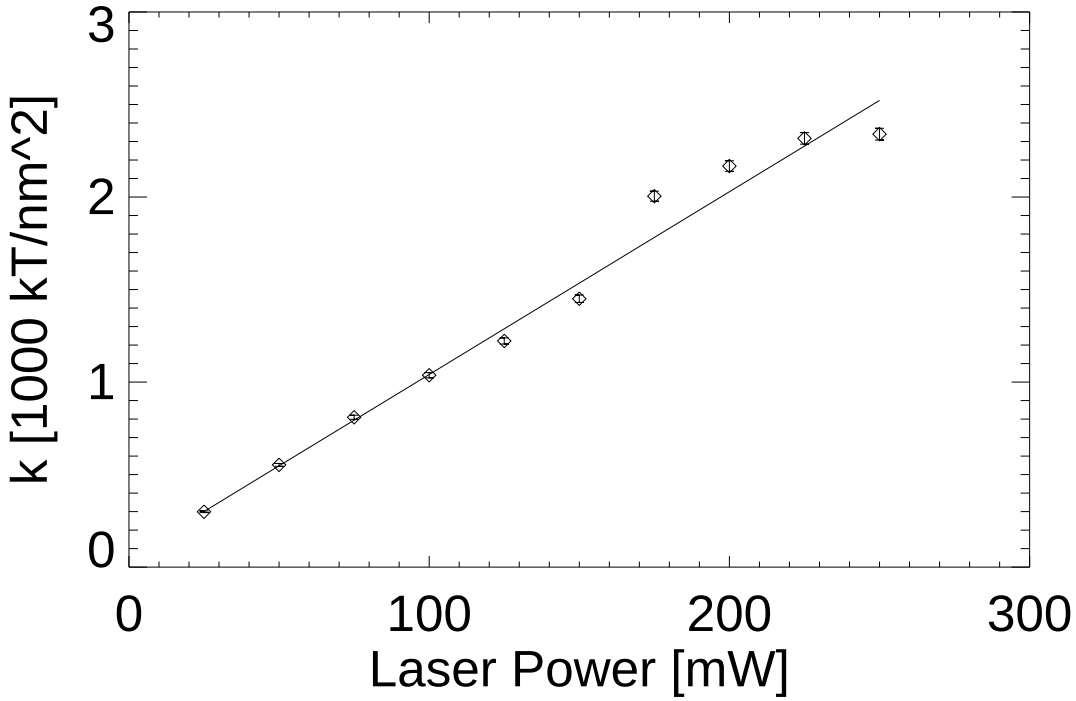

Figure A.10: *Tweezer strength, k, versus laser intensity.* The solid curve is a fit to a straight line.

output of the laser head. Mirrors, lenses and filters absorb, scatter and reflect well over fifty percent of the laser light as it travels from the laser head to the focal plane of the microscope objective. Since we do not know the precise fraction of the light that reaches the final tweezer, we simply report the intensity measured by the power meter.

However, we can compare the intensity dependence of the trapping force to Harada and Asakura's derivation of optical gradient forces in the Rayleigh limit. If the sphere is dominated by the gradient force then Eq. 2.4 implies that

$$\vec{F}(\vec{r}) = \alpha\vec{\nabla}I(\vec{r}) = \alpha I_o\vec{\nabla}f(\vec{r}), \tag{A.7}$$

where α describes the optical and geometrical properties of the trapped particle, I_o is the laser intensity and $f(\vec{r})$ describes the geometrical profile of the beam. The spring constant of the laser in the x-direction is therefore

$$k_x = \partial_x F_x(\vec{r})|_{\vec{r}_o} = \alpha I_o \partial_x^2 f(\vec{r})|_{\vec{r}_o} \equiv \beta I_o, \tag{A.8}$$

where $\vec{r}_o$ is the location of the trap's potential minimum. Fitting the measured tweezer stiffness' dependence on laser intensity to Eq. A.8, we find $\beta = (9.8 \pm 0.1) \times 10^{-6}\,\frac{k_BT}{nm^2mW}$, Fig. A.10.

We can estimate the overall depth of the optical trap as a function of laser intensity. Combining Eqs. A.5 and A.8,

$$U_o \approx \frac{1}{2}k_x\left(\frac{\lambda}{2}\right)^2 = \beta\left(\frac{\lambda}{2}\right)^2 I_o. \tag{A.9}$$

For our particular setup

$$U_o \approx 0.7 \left(\frac{I_o}{[mW]} \right) k_B T. \tag{A.10}$$

Therefore, for each milliwatt of laser light emitted from our laser, the depth of the optical trap increases by about $1\, k_B T$.

REFERENCES

[1] A. Kose *et al.*, J. Colloid Interface Sci. **44**, 330 (1973).

[2] J. M. Weissman, H. B. Sunkara, A. S. Tse, and S. A. Asher, Science **274**, 959 (1996).

[3] J. H. Holtz and S. A. Asher, Nature **389**, 829 (1997).

[4] G. Pan, R. Kesavamoorthy, and S. A. Asher, Phys. Rev. Lett. **78**, 3860 (1997).

[5] A. van Blaaderen, R. Ruel, and P. Wiltzius, Nature **385**, 321 (1997).

[6] M. J. Murray and J. V. Sanders, Phil. Mag. A **42**, 721 (1980).

[7] E. Yablonovitch, J. Opt. Soc. Am. B **10**, 283 (1993).

[8] J. D. Joannopoulos, R. D. Meade, and J. N. Winn, *Photonic Crystals* (Princeton University Press, Princeton, 1995).

[9] W. Zhang *et al.*, Phys. Rev. Lett. **84**, 2853 (2000).

[10] J. Israelachvili, *Intermolecular and Surface Forces*, 2 ed. (Academic Press, London, 1992).

[11] H. Jensenius and G. Zocchi, Phys. Rev. Lett. **79**, 5030 (1997).

[12] A. D. Dinsmore, D. T. Wong, P. Nelson, and A. G. Yodh, Phys. Rev. Lett. **80**, 409 (1998).

[13] J. C. Crocker and D. G. Grier, MRS Bull. **23**, 24 (1998).

[14] R. Brown, Phil. Mag. **4**, 161 (1828).

[15] A. Einstein, Ann. der Phys. **17**, 549 (1905).

[16] P. Langevin, C. R. Acad. Sci. **146**, 530 (1908).

[17] J. Perrin, Ann. Chim. Phys. **18**, 1 (1909).

[18] J. Perrin, *Les Atomes* (Librairie Alcan, Paris, 1914).

[19] A. Fick, Ann. der Phys. **170**, 59 (1855).

[20] E. R. Dufresne and D. G. Grier, J. Chem. Phys. **110**, 8845 (1999).

[21] W. B. Russel, D. A. Saville, and W. R. Schowalter, *Colloidal Dispersions*, *Cambridge Monographs on Mechanics and Applied Mathematics* (Cambridge University Press, Cambridge, 1989).

[22] S. Alexander *et al.*, J. Chem. Phys. **80**, 5776 (1984).

[23] J. C. Crocker and D. G. Grier, Phys. Rev. Lett. **77**, 1897 (1996).

[24] A. E. Larsen and D. G. Grier, Phys. Rev. Lett. **76**, 3862 (1996).

[25] A. E. Larsen and D. G. Grier, Nature **385**, 230 (1997).

[26] P. D. Kaplan, J. L. Rouke, A. G. Yodh, and D. J. Pine, Phys. Rev. Lett. **72**, 582 (1994).

[27] J. Walz and A. Sharma, J. Coll. Int. Sci. **168**, 485 (1994).

[28] A. D. Dinsmore, A. G. Yodh, and D. J. Pine, Nature **383**, 239 (1996).

[29] R. Verma, J. C. Crocker, T. C. Lubensky, and A. G. Yodh, Phys. Rev. Lett. **81**, 4004 (1998).

[30] C. Bechinger *et al.*, Phys. Rev. Lett. **83**, 3960 (1999).

[31] J. C. Crocker, J. A. Matteo, A. D. Dinsmore, and A. G. Yodh, Phys. Rev. Lett. **82**, 4352 (1999).

[32] E. R. Dufresne and D. G. Grier, Rev. Sci. Instr. **69**, 1974 (1998).

[33] J. C. Crocker and D. G. Grier, J. Colloid Interface Sci. **179**, 298 (1996).

[34] A. Ashkin, J. M. Dziedzic, J. E. Bjorkholm, and S. Chu, Opt. Lett. **11**, 288 (1986).

[35] J. C. Crocker and D. G. Grier, Phys. Rev. Lett. **73**, 352 (1994).

[36] J. Crocker, J. Chem. Phys. **106**, 2837 (1997).

[37] T. Sugimoto *et al.*, Langmuir **13**, 5528 (1997).

[38] D. G. Grier, Current Opinion Colloid Interface Sci. **2**, 264 (1997).

[39] J.-C. Meiners and S. R. Quake, Phys. Rev. Lett. **82**, 2211 (1999).

[40] A. Ashkin, J. M. Dziedzic, and T. Yamane, Nature **330**, 769 (1987).

[41] S. C. Kuo and M. P. Sheetz, Science **260**, 232 (1993).

[42] T. T. Perkins, D. E. Smith, R. G. Larson, and S. Chu, Science **268**, 83 (1995).

[43] H. Yin *et al.*, Science **270**, 1653 (1995).

[44] M. D. Wang *et al.*, Biophys. J. **72**, 1335 (1997).

[45] M. Wang *et al.*, Science **282**, 902 (1998).

[46] K. Sasaki *et al.*, Opt. Lett. **16**, 1463 (1991).

[47] K. Sasaki *et al.*, Jap. J. Appl. Phys. **30**, L907 (1991).

[48] L. P. Faucheux, L. S. Bourdieu, P. D. Kaplan, and A. J. Libchaber, Phys. Rev. Lett. **74**, 1504 (1995).

[49] A. Ashkin, Biophys. J. **61**, 569 (1992).

[50] Y. Harada and T. Asakura, Opt. Comm. **124**, 529 (1996).

[51] A. Ashkin, Proc. National Academy Sci., USA **94**, 4853 (1997).

[52] C. Bohren and D. Huffman, *Absorption and Scattering of Light by Small Particles* (Wiley, New York, 1983).

[53] K. Svoboda and S. M. Block, Optics Letters **19**, 930 (1994).

[54] K. Sasaki, M. Koshioka, M. Hiroaki, and N. Kitamura, Appl. Phys. Lett. **60**, 807 (1992).

[55] H. He, N. R. Heckenberg, and H. Rubinsztein-Dunlop, J. Mod. Opt. **42**, 217 (1995).

[56] M. E. J. Friese, T. A. Nieminen, N. R. Heckenberg, and H. Rubinsztein-Dunlop, Nature **394**, 348 (1998).

[57] E. Fällman and O. Axner, Appl. Opt. **36**, 2107 (1997).

[58] A. Chowdhury, B. J. Ackerson, and N. A. Clark, Phys. Rev. Lett. **55**, 833 (1985).

[59] M. M. Burns, J.-M. Fournier, and J. A. Golovchenko, Science **249**, 749 (1990).

[60] A. E. Chiou *et al.*, Opt. Comm. **133**, 7 (1997).

[61] K. Visscher, S. P. Gross, and S. M. Block, IEEE J. Selected Topics Quantum Elect. **2**, 1066 (1996).

[62] G. M. Kepler and S. Fraden, Phys. Rev. Lett. **73**, 356 (1994).

[63] M. D. Carbajal-Tinoco, F. Castro-Román, and J. L. Arauz-Lara, Phys. Rev. E **53**, 3745 (1996).

[64] S. H. Behrens, preprint (2000).

[65] J.-P. Hansen and I. R. McDonald, *Theory of Simple Liquids*, 2nd ed. (Academic Press, London, 1986).

[66] B. J. Ackerson and N. A. Clark, Phys. Rev. Lett. **46**, 123 (1981).

[67] B. J. Ackerson and P. N. Pusey, Phys. Rev. Lett. **61**, 1033 (1988).

[68] R. E. Caflisch and J. H. C. Luke, Phys. Fluids **28**, 759 (1985).

[69] P. N. Segrè, E. Herbolzheimer, and P. M. Chaikin, Phys. Rev. Lett. **79**, 2574 (1997).

[70] M. P. Brenner, Phys. Fluids **11**, 754 (1999).

[71] R. Bruinsma and S. Alexander, J. Chem. Phys. **92**, 3074 (1990).

[72] M. Trau, S. Sankaran, D. A. Saville, and I. A. Aksay, Nature **374**, 437 (1995).

[73] M. Trau, D. A. Saville, and I. A. Aksay, Science **272**, 706 (1996).

[74] Y. Han and D. G. Grier, preprint (2000).

[75] T. M. Squires and M. P. Brenner, preprint (1999).

[76] J. Happel and H. Brenner, *Low Reynolds Number Hydrodynamics* (Kluwer, Dordrecht, 1991).

[77] C. Pozrikidis, *Boundary Integral and Singularity Methods for Linearized Viscous flow* (Cambridge University Press, Cambridge, 1992).

[78] G. K. Batchelor, J. Fluid Mech. **52**, 245 (1972).

[79] L. P. Kadanoff, *Lectures in Statistical Physics: Statics, Dynamics, Renormalization* (unpublished, Chicago, 1997).

[80] G. K. Batchelor, J. Fluid Mech. **74**, 1 (1976).

[81] A. Pralle, E.-L. Florin, E. H. K. Stelzer, and J. K. H. Hörber, Appl. Phys. A **66**, S71 (1998).

[82] B. Lin and S. A. Rice, preprint (1999).

[83] H. Lorentz, Zittingsverlag Akad. v. Wet. **5**, 168 (1896).

[84] J. Blake, Proc. Camb. Phil. Soc. **70**, 303 (1971).

[85] E. R. Dufresne, T. M. Squires, M. P. Brenner, and D. G. Grier, preprint (2000).

[86] E. R. Dufresne, D. M. Altman, and D. G. Grier, preprint (2000).

[87] L. Lobry and N. Ostrowsky, Phys. Rev. B **53**, 12050 (1996).

[88] C. Oseen, *Nuere Methoden und Ergebnisse in der Hydrodynamik* (Akademische Verlagsgesellschaft, Leipzig, 1927).

[89] L. P. Faucheux and A. J. Libchaber, Phys. Rev. E **49**, 5158 (1994).

[90] N. Liron and S. Mochon, J. Eng. Mathematics **10**, 287 (1976).

[91] L. D. Landau and E. M. Lifshitz, *Fluid Mechanics*, *Course of Theoretical Physics* (Pergamon Press, New York, 1959).

[92] D. G. Grier and E. R. Dufresne, *An Apparatus for Applying Optical Gradient Forces*, U.S. Patent No. 6,055,106, (2000).

[93] E. R. Dufresne, M. T. Dearing, G. C. Spalding, and D. G. Grier, preprint (2000).

[94] S. Lipson and H. Lipson, *Optical Physics*, 2nd ed. (Cambridge University Press, Cambridge, 1981).

[95] K. T. Gahagan and J. G. A. Swartzlander, Opt. Lett. **21**, 827 (1996).

[96] E. Hecht, *Optics*, 2nd ed. (Addison-Wesley, Reading, MA, 1987).

[97] V. Soifer, V. Kotlyar, and L. Doskolovich, *Iterative Methods for Diffractive Optical Elements Computation* (Taylor and Francis, London, 1997).

[98] G. J. Swanson and W. B. Veldkamp, Opt. Eng. **28**, 605 (1989).

[99] Y. Igasaki *et al.*, Opt. Rev. **6**, 339 (1999).

[100] T. S. Sullivan, C.-H. Sow, and C. A. Murray, preprint (2000).

[101] K. Harada *et al.*, Science **274**, 1167 (1996).

[102] C. Reichhardt, J. Olson, and F. Nori, Phys. Rev. B. **57**, 7937 (1998).

[103] J. Chakrabarti, H. R. Krishnamurthy, and A. K. Sood, Phys. Rev. Lett. **73**, 2923 (1994).

[104] J. Chakrabarti, H. R. Krishnamurthy, A. K. Sood, and S. Sengupta, Phys. Rev. Lett. **75**, 2232 (1995).

[105] R. M. Simmons, J. T. Finer, S. Chu, and J. A. Spudich, Biophys. J. **70**, 1813 (1996).

[106] E.-L. Florin, A. Pralle, E. H. K. Stelzer, and J. K. H. Hörber, Appl. Phys. A **66**, S75 (1998).

[107] L. P. Ghislain, N. A. Switz, and W. W. Webb, Rev. Sci. Instrum. **65**, 2762 (1994).

[108] W. Denk and W. W. Webb, Appl. Opt. **29**, 2382 (1991).

[109] M. E. J. Friese, J. Enger, H. Rubinsztein-Dunlop, and N. R. Heckenberg, Phys. Rev. A **54**, 1593 (1996).

[110] K. Visscher and S. M. Block, Methods in Enzymology **298**, 460 (1998).